Title

Mad for magnetosomes: Uncovering the mechanism for synthesizing and organizing tooth-shaped magnetosomes in Desulfovibrio magneticus RS-1

Author

Russell, Virginia Vandever

Publication Date

2024

Peer reviewed|Thesis/dissertation

Mad for magnetosomes: Uncovering the mechanism for synthesizing and organizing tooth-shaped magnetosomes in *Desulfovibrio magneticus* RS-1

By

Virginia V Russell

A dissertation submitted in partial satisfaction of the

requirements for the degree of

Doctor of Philosophy

in

Microbiology

in the

Graduate Division

of the

University of California, Berkeley

Committee in charge:

Professor Arash Komeili, Chair
Professor Michi Taga
Professor Kim Seed
Professor James Olzmann

Spring 2024

Abstract

Mad for magnetosomes: Uncovering the mechanism for synthesizing and organizing tooth-shaped magnetosomes in *Desulfovibrio magneticus* RS-1

by

Virginia Vandever Russell

Doctor of Philosophy in Microbiology

University of California, Berkeley

Professor Arash Komeili, Chair

Magnetotactic Bacteria (MTB) are a diverse, ubiquitous group of bacteria that navigate along the Earth's geomagnetic field in search of optimal environments with low or no oxygen. They achieve this by producing magnetosomes, organelles made up of magnetite or greigite typically enclosed in a lipid membrane. The process of magnetosome formation is extensively studied in two alpha-Proteobacterial species, known for their cubooctahedral magnetite crystals encased in lipid membranes. Alternatively, the synthesis mechanisms for tooth-shaped magnetosomes, believed to be the ancestral form of magnetosomes, remain largely unexplored. We used *Desulfovibrio magneticus* RS-1, a delta-Proteobacterium, as a model organism to understand the mechanisms of synthesizing magnetosomes in deeper branching MTB. This study has revealed that when RS-1 is cultivated in hydrogen-rich environments, magnetosomes fail to form, though iron uptake is not impacted. When hydrogen is substituted with nitrogen, the process of magnetite biomineralization begins and can be monitored with different techniques. We observe that early in the biomineralization cycle, cells predominantly contain equidimensional crystals, which later elongate and take on the distinctive tooth shape as the cycle progresses. Additionally, we discovered that chain formation occurs concurrently with biomineralization. Early in the cycle, cells possess one or a few crystals, while in later stages, they develop the typical long chains composed of several smaller sub-chains. Next, we pinpointed various genes and proteins that play roles in different stages of magnetosome synthesis through proteomic and genetic analyses. The findings show that magnetosomes extracted from cells at various stages of biomineralization contain different proportions of magnetosome proteins. MamA, MamB, MamEO, FmpA, FmpB, Mad4, and Mad10 are more abundant in the initial stages of biomineralization, while Mad20, Mad23, Mad28, and MamK are more abundant in the later stages of the process. Subsequently, we employed genetic techniques to investigate if these different cohorts of proteins have specific functions in magnetosome chain formation. Mutants of *fmpA* and *fmpB* exhibit significant disruptions in the early phases of magnetosome production and fail to develop into longer chains. Conversely, deletion mutants of *mad10*, *mad20*, *mad23*, *mad25*, *mad26*, *mad28*, and *mamK* exhibited a range of defects in the organization of the chains. Based on these results, we propose a model that RS-1 produces magnetosomes consecutively using the early biomineralization genes and actively transports these crystals to the positive curvature of the cell to construct a mature magnetosome chain. Notably, this method of chain organization is significantly different from that seen in alpha-Proteobacterial MTB. Our study

highlights the shared as well as distinct evolutionary paths for magnetosome formation in deep-branching MTB. It also emphasizes the critical need for direct molecular genetic studies of magnetosome formation in diverse MTB model systems.

Table of Contents

Abbreviations/Definitions

MTB: Magnetotactic Bacteria
MAI: Magnetosome Gene Island
MGC: Magnetosome Gene Cluster
mam: Magnetosome gene set
mms: Magnetic particle Membrane-Specific gene set
mad: Magnetosome deep-branching gene set
man: Magnetosome Nitrospirae gene set
WT: Wildtype
C_{Mag}: Coefficient of magnetic response

Positive curvature: Located above a positive curve (Chapter 1, Supplemental Figure S1)

Introduction

Microbial biomineralization, the process by which microbes can synthesize minerals, is a phenomenon associated with a wide range of bacterial species. The notion of regulated biomineralization, the process where a set of genes direct mineralization as opposed to it being merely a byproduct of an organism's activity, was first characterized by Mann in 1983 (*1*). This description was based on the principle of 'organic matrix mediation,' a term originally introduced by Lowenstam in 1981 (*2*). Controlled biomineralization can take place within a cell, outside of a cell, or in both locations, where the process begins inside the cell and is then moved to an external location during the final stages (*3*). Microbes may synthesize minerals for a variety of advantageous functions. The range of functions includes: (i) serving as a reservoir for elements like iron, sulfur, or carbon, (ii) facilitating movement by utilizing Earth's geomagnetic fields with magnetic minerals or ascending through the water column via the buoyancy of amorphous calcium carbonate (ACC), (iii) enabling adhesion, as seen in iron oxidizers that produce iron stalks, and (iv) acting as electron acceptors, with extracellular magnetite or (ACC) being examples of minerals with this capacity (*3*). The most studied and best example of controlled biomineralization in prokaryotes is the biomineralization of intracellular iron minerals by magnetotactic bacteria (*3*).

Magnetotatic Bacteria (MTB) are a diverse, ubiquitous group of bacteria capable of navigating along the Earth's geomagnetic field in search of the optimal environment with low to no oxygen. A typical magnetosome consists of a lipid bilayer membrane with a unique set of proteins that synthesizes and encloses a magnetic crystal composed of either magnetite (Fe_3O_4) or greigite (Fe_3S_4) (*4*). In a cell, magnetosomes are usually present as a single chain or multiple chains depending on the species. This chain arrangement maximizes the magnetic dipole moment of the cell allowing it to align along the magnetic field (*5*). Individual magnetosomes usually measure 50-70 nm in diameter, but can have many different morphologies (*5*) including cubooctohedral, pseudo-hexagonal, truncated hexa-octahedral and tooth-shaped. The most well-characterized models of magnetotactic bacteria *Magnetospirillum magneticum* AMB-1 and *Magnetospirillum gryphiswaldense* MSR-1 belong to the sub-phyla of alpha-Proteobacteria and synthesize cubooctohedral magnetite crystals. Extensive and valuable research has emerged from the study of these models, yet they constitute only a fraction of the diversity found within MTB. Here, we used an alternative model organism, *Desulfovibrio magneticus* RS-1, a member of delta-Proteobacteria, to uncover the mechanism for producing and organizing tooth-shaped magnetite magnetosomes in deep-branching MTB.

Chapter 1, a review of the current literature, will discuss the diversity of MTB and the need for models outside of the sub-phyla of alpha-Proteobacteria. Chapter 2 will explore the process of magnetosome assembly in RS-1. It unveils genetic and mechanistic perspectives on the process by which deep-branching MTB synthesize and arrange magnetosomes, presenting a distinct contrast to the established mechanisms observed in alpha-Proteobacteria. Furthermore, it delves into the newly uncovered phenomenon of magnetosome formation being hindered when hydrogen is present. Lastly, Chapter 3 presents a genetic screening strategy to investigate the mechanism of magnetosome inhibition in the presence of hydrogen.

Acknowledgements

I would like to thank my thesis committee chair, Professor Arash Komeili, for the guidance and mentorship during the process of my dissertation. I would also like to thank the rest of my committee, Michi Taga, Kim Seed, and James Olzmann, for their help and assistance during this process. Gratitude is extended to the team at the University of California Berkeley Electron Microscope Laboratory for their guidance and support with electron microscopy, with particular thanks to Danielle Jorgens, Reena Zalpuri, and Misun Kang for their comprehensive advice and assistance. Furthermore, I extend my heartfelt thanks to a previous mentor, Dr. José de la Torre, my master's thesis advisor, who played a pivotal role in my growth as an early-career scientist and motivating me to embark on a PhD journey. I also would like to thank the rest of the Komeili lab for all of their advice and support.

Chapter 1

Exploring the diversity of magnetotactic bacteria using deep-branching model organisms.

Virginia V. Russell[1] and Arash Komeili[1]

[1] *Plant and Microbiology, University of California Berkeley, Berkeley, California, USA.*

Section 1: Broader diversity of MTB

Magnetotactic bacteria (MTB) represent a diverse and ubiquitous collective of bacteria that possess the unique ability to orient and move along the Earth's geomagnetic lines, enabling them to locate environments with reduced or absent levels of oxygen. MTB achieve this by orienting themselves along geomagnetic fields in tandem with aerotaxis and chemotaxis, which guides them to the most suitable oxygen zone within a sediment or water column (*5*). The ability to implement this magnetotaxis behavior is mediated by a specialized organelle, the magnetosome. A typical magnetosome consists of a lipid bilayer membrane with a unique set of proteins that synthesizes and encloses a magnetic crystal composed of either magnetite (Fe_3O_4) or greigite (Fe_3S_4) (*6*). In a cell, magnetosomes are usually present as a chain or multiple chains depending on the species. This chain arrangement maximizes the magnetic dipole moment of the cell allowing it to align along the magnetic field (*5*). The mechanisms by which MTB synthesize and organize their magnetosomes has been most well-studied in two closely related species, *Magnetospirillum magneticum* AMB-1 and *Magnetospirillum gryphiswaldense* MSR-1, even though the number of identified MTB has been growing exponentially since their discover in the 1970s (*7*–*9*).

The phylogenetic diversity of magnetotactic bacteria is vast and encompasses several different phyla of bacteria (Figure 1). MTB comprise a polyphyletic group of microorganisms that belong within four subdivisions of Proteobacteria (Alpha, Gamma, Eta and Delta) and the phyla of Nitrospirae, Omnitrophica and Elusimicrobiota (*6*, *10*, *11*). In addition, metagenomic analysis has suggested Latescribacteria and Planctomyetes phyla may also contain MTB species (*12*). Magnetotactic Eukaryotes have also been described. In some cases they acquire magnetosomes through the ingestion of MTB (*13*), or free magnetosomes after cell lysis. In other cases, they have formed a mutualistic relationship with ectosymbiotic MTB (*14*). There is also evidence for eukaryotic protists that may independently form magnetosome-like chains (*15*). Thus far, magnetotactic Archaea or Gram-positive bacteria have not been discovered. In addition to this phylogenetic diversity, there is great morphological variation amongst MTB. This diversity encompasses differences in crystal geometry, cell structure, oxygen preference, chain arrangement, magnetosome quantity per cell, and crystal composition across various MTB species (*5*).

The most notable type of diversity among MTB is the arrangement and geometry of magnetosomes within the cell. The geometry of magnetosome crystals is significant because it exemplifies the precise connection between biological factors and controlled synthesis of inorganic crystals. Based on extensive surveys, there seems to be a correlation between phylogeny and crystal shape. For example, alpha-Proteobacteria are known to biomineralize cubooctahedral and elongated prismatic magnetite crystals (*5*) In contrast, delta-Proteobacteria and other deeply divergent MTB groups, like Nitrospirae, OP3 and Elusimicrobiota, which synthesize magnetite magnetosomes, produce irregular, tooth-like crystal shapes. This implies that the tooth-shaped magnetosome crystals might represent the ancestral form of magnetosomes. Moreover, everything that is known regarding the molecular mechanism for magnetosome synthesis has come out of research on two model organisms for MTB, *Magnetospirillum magneticum* AMB-1 and *Magnetospirillum gryphiswaldense* MSR-1. However, that is only a small representation of all known MTB. The diversity of known magnetotactic bacteria (MTB) is continuously expanding, yet the selection of model organisms for investigating the biosynthesis of magnetosomes still remains quite limited.

Section 2: Developing RS-1 as a model

2.1 The discovery of RS-1 and other deep-branching MTB

Desulfovibrio magneticus RS-1 was first described in 1993 by T. Sakaguchi et al. (*16*). It was isolated from sediments near the Kameno River in Wakayama Prefecture, in Western Japan (*17*). RS-1 is a dissimilatory sulfate-reducing bacterium, belonging to the delta-Proteobacteria sub-phylum, that is capable of synthesizing a single chain of irregular tooth-shaped magnetite magnetosomes. Discovering that a dissimilatory sulfate-reducing bacterium was among those able to produce magnetite instead of the sulfur-containing greigite magnetosomes was surprising. Initially, upon cultivation, RS-1 demonstrated a subdued magnetic response, likely attributed to its growth in a sulfate-enriched environment. *Desulfovibrios* generate hydrogen sulfide as a byproduct of sulfate metabolism. This hydrogen sulfide can react with iron to form iron sulfide precipitate, thus reducing the amount of free iron available for magnetosome formation. RS-1 can use sulfate for growth (*16*), but fumarate can also serve as an alternative electron acceptor (*17*). Replacement of sulfate with fumarate, resulted in an increased production of magnetosomes (*17*). The detection of magnetite magnetosomes in RS-1 broadened the scientific perspective, leading to the development of new hypotheses regarding the evolutionary origins of magnetosomes (*18*).

Concurrent with the uncovering of RS-1, several other deep-branching MTB were also identified. One of those was *Ca. Magnetoglobus multicellularis*, an obligately multicellular bacterium, was discovered before the isolation of RS-1, and also belongs to the delta-Proteobacteria (*19*). However, *M. multicellularis* produces greigite magnetosomes exclusively (*19*). The finding of greigite magnetosomes in *M. multicellularis* gave rise to the hypothesis that magnetite magnetosomes were unique to alpha-Proteobacteria and had evolved independently from greigite magnetosome containing MTB (*20*). However, the identification of RS-1 possessing magnetite magnetosomes called this theory into question. Then one month after RS-1 was isolated and described another deep-branching MTB from microaerobic freshwaters was discovered to also contain tooth-shaped magnetite magnetosomes (*21*). This MTB, *Magnetobacterium bavaricum*, belongs to another phyla entirely, Nitrospirae, further widening the diversity of MTB (*7*). Since *M. bavaricum* has not been cultured, research into its magnetosome production has been primarily limited to transmission electron microscopy (TEM) (*21*). Finally, the discovery of another deep-branching MTB, *Desulfamplus magnetovallimortis* BW-1, an organism capable of producing both magnetite and greigite magnetosomes, even further challenged the idea of a separate evolution for greigite and magnetite magnetosomes (*22*). The initial isolation of RS-1, followed by the identification of various other deep-branching MTB, ignited a wave of curiosity regarding the true diversity and evolution of magnetotactic bacteria. But the limiting factor was the current model organisms for all MTB, AMB-1 and MSR-1, were not sufficient to study these newly discovered diverse MTB, especially in regards to the unique morphology and chemical composition of their crystals.

2.2 Magnetosomes Formation in RS-1

The process by which magnetosomes are formed in the cell has only been studied in a two species of alpha-Proteobacteria, AMB-1 and MSR-1, which have cubooctohedral shaped magnetosomes surrounded by a lipid membrane. However, this model of magnetosome formation does not hold true for deep-branching magnetotatic bacteria. A core set of 7 or 8 magnetosome genes, *mamA, B, I, K, M, E, O* (*mamO* and *mamP* or *mamP-like* are disputed

among different literatures), and *Q*, found in the *mamAB* operon of AMB-1 and MSR-1 are present in all sequenced MTB ((*8*, *23*), Figure 1B). However, many of the genes necessary for magnetosome formation in the alpha-Proteobacteria are absent from other MTB. Other sets of conserved genes, called *mad* (deep branching magnetosome) and *man* (Nitrospirae magnetosome) genes, exist in all deep-branching MTB and only Nitrospirae MTB respectively instead (Figure 1A and C). The *mad* genes are completely absent from the alpha-, gamma- and eta-Proteobacteria, yet they are present in all deeply divergent MTB. This observation has led to the hypothesis that the *mad* genes govern the process of synthesizing and organizing tooth-shaped magnetosome in the deep-branching MTB. However, little to nothing is known about the function of any of the *mad* genes or the production of irregular, tooth-shaped magnetosomes.

As mentioned previously, *Desulfovibrio magneticus* RS-1, a delta-Proteobacterium, synthesizes a single chain of irregular tooth-shaped magnetite magnetosomes. The magnetosome chain is positioned along the cell's positive curvature (Supplemental Figure S1), extending the full cell length with intermittent spaces between clusters of adjacent crystals. A notable feature of magnetosomes in RS-1 is the absence of a membrane encasing the fully formed crystal (*24*), despite the presence of magnetosome-associated genes that include transmembrane domains. Considering RS-1 possesses magnetosome genes with membrane domains, it is logical to infer that membranes play a role in some stage of magnetosome formation, yet the specifics of this involvement are still not fully understood. Furthermore, *Desulfamplus magnetomortis* BW-1, which harbors both greigite cubooctahedral and tooth-shaped magnetite magnetosomes, has been demonstrated to have membranes encircling the greigite magnetosomes (*22*). However, no imagery has depicted membranes encasing the tooth-shaped magnetite magnetosomes (*22*).

Previous studies have shown that in contrast to AMB-1 and MSR-1, which synchronize the synthesis of their magnetosomes when transitioning out of iron starvation (Figure 2, (*4*)), RS-1 produces its magnetosomes sequentially (Figure 2, (*24*, *25*)). This significant contrast supports the view that the process of magnetosome production in RS-1 diverges markedly from the synthesis mechanism in AMB-1 and MSR-1. Moreover, RS-1 lacks certain crucial genes that are involved in magnetosome formation in AMB-1 and MSR-1, and it possesses additional magnetosome genes that are unique to deep-branching MTB (Figure 1C). Clues to the importance of these genes emerged from a chemical and UV mutagenesis-based forward genetics screen that identified non-magnetic mutants of RS-1 (*25*). This screen identified mutations in *mam* genes such as *mamL* and *mamB*, highlighting the importance and functionality of the core magnetosome genes in RS-1. It also revealed that mutations in genes conserved in deep-branching MTB can impair magnetosome formation. For instance, *fmpA* and *fmpB* mutations resulted in mutants with significantly fewer and smaller magnetosomes (*25*). Moreover, mutations in *mad1* and *mad2* led to magnetosomes that were aberrant in size and shape compared to the wild type (*25*). Findings from these studies identified a group of genes implicated in the initial phases of biomineralizing tooth-shaped magnetosomes, controlling the size and morphology of the crystals (*25*). Based on these studies we have hypothesized that magnetosome formation in RS-1 consists of three stages: 1) Crystal nucleation, where the formation of crystals is initiated. 2) Growth, size, and shape control, during which crystals continue to grow and specific genes dictate the size and shape of each crystal. 3) Chain alignment and organization, where another set of genes aligns the chain to the cell's positive curvature and arranges it linearly along the cell's length (Figure 3).

RS-1 stands as the sole magnetotactic bacterium, cultured from beyond the alpha-Proteobacteria sub-phylum, that not only has its genome sequenced but also has genetic tools at

its disposal (*26*). As such, RS-1 is a good model organism to study the diversity of magnetosome formation and uncover the mechanisms behind the biomineralization of tooth-shaped magnetite particles. Understanding the mechanism for synthesizing tooth-shaped magnetosomes is critical because they constitute the bulk of magnetism found in sediment environments (*5*). Studying tooth-shaped magnetite magnetosomes is pivotal as they are likely the ancestral form of magnetosomes, given that all magnetite magnetosomes in deeply divergent MTB exhibit this shape (*12*). Thus, new research using RS-1 as a model organism could reveal the evolution of the biomineralization processes of magnetosomes in MTB. Finally, while recent experiments have utilized magnetosome genes from distantly related MTB to complement gene deletions in MSR-1, the effectiveness of these complementations were weaker in proportion to the evolutionary distance of the source organism (*27, 28*). This underscores the importance of examining magnetosome genes and protein functions within their native systems and ensuring representation from the deeper-branching MTB. Therefore, *Desulfovibrio magneticus* RS-1 serves as an ideal model organism for elucidating the processes involved in the synthesis and organization of tooth-shaped magnetosomes in a more evolutionarily ancient MTB.

Section 3: Future directions

In conclusion, incorporating models from more distantly related organisms is crucial for addressing questions regarding the mechanisms for formation of morphogically diverse varieties of magnetosome. Beyond the well-characterized alpha-Proteobacterial models of magnetotactic bacteria, *Magnetospirillum magneticum* AMB-1 and *Magnetospirillum gryphiswaldense* MSR-1, *Desulfovibrio magneticus* RS-1 offers a superior model for investigating the mechanisms at play in the deep-branching MTB. At present, it is possible to generate single gene deletions in RS-1 via an allelic exchange, but further advancements in this system are necessary. Enhancing the genetic and molecular tools in RS-1 will enable more comprehensive studies into the intricate mechanisms of synthesizing and organizing tooth-shaped magnetite magnetosomes. Moreover, it would be advantageous to develop additional model systems from various deep-branching MTB in the future. Such models could provide insights into whether the process of synthesizing and organizing tooth-shaped magnetosomes is controlled among many deep-branching MTB or if diverse mechanisms are employed. This, in turn, could yield even greater understanding of how magnetosome synthesis has evolved across multiple bacterial phyla.

Figures:

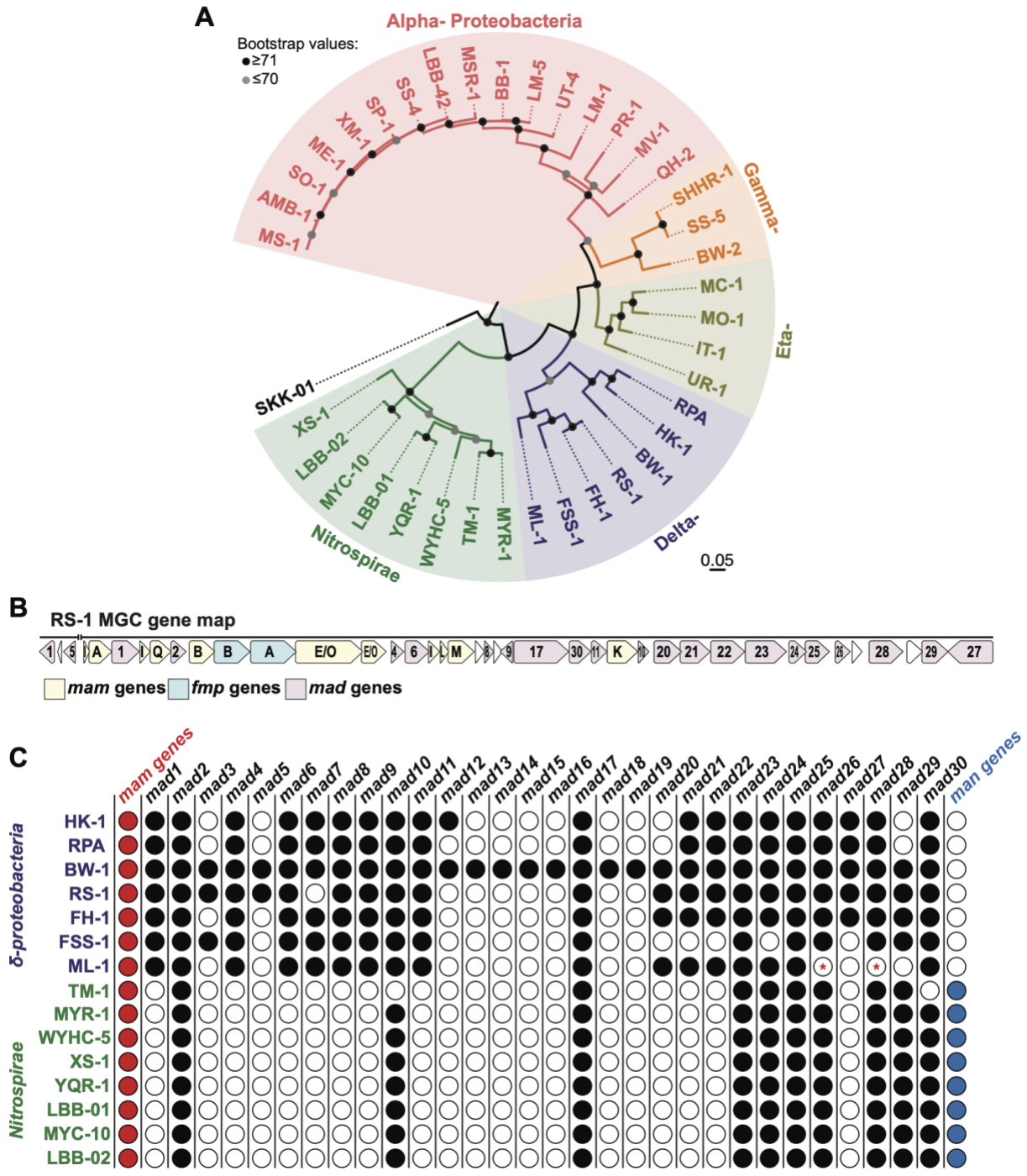

Figure 1. *Phylogeny and gene comparison of deep-branching Magnetotactic Bacteria*

(A). 16S maximum likelihood phylogenetic tree of magnetotactic bacteria representing four different sub groups of Proteobacteria as well as the deeper branching phyla of Nitrospirae. The tree was rooted with *Omnitrophus magneticus* SKK-01. MAFFT was used for alignment of 16S genes and maximum likelihood tree was built using PhyML Tree with GTR substitution model

and 1000 bootstraps. (B) Gene map of magnetosome gene cluster found in *Desulfovibrio magneticus* RS-1. (C). Gene comparison for all deep branching MTB from tree in A, focusing on the *mad* (deep branching magnetosome) genes (*8*, *23*, *29*). Red asterisks represent uncertainty as there was no complete genome available on NCBI.

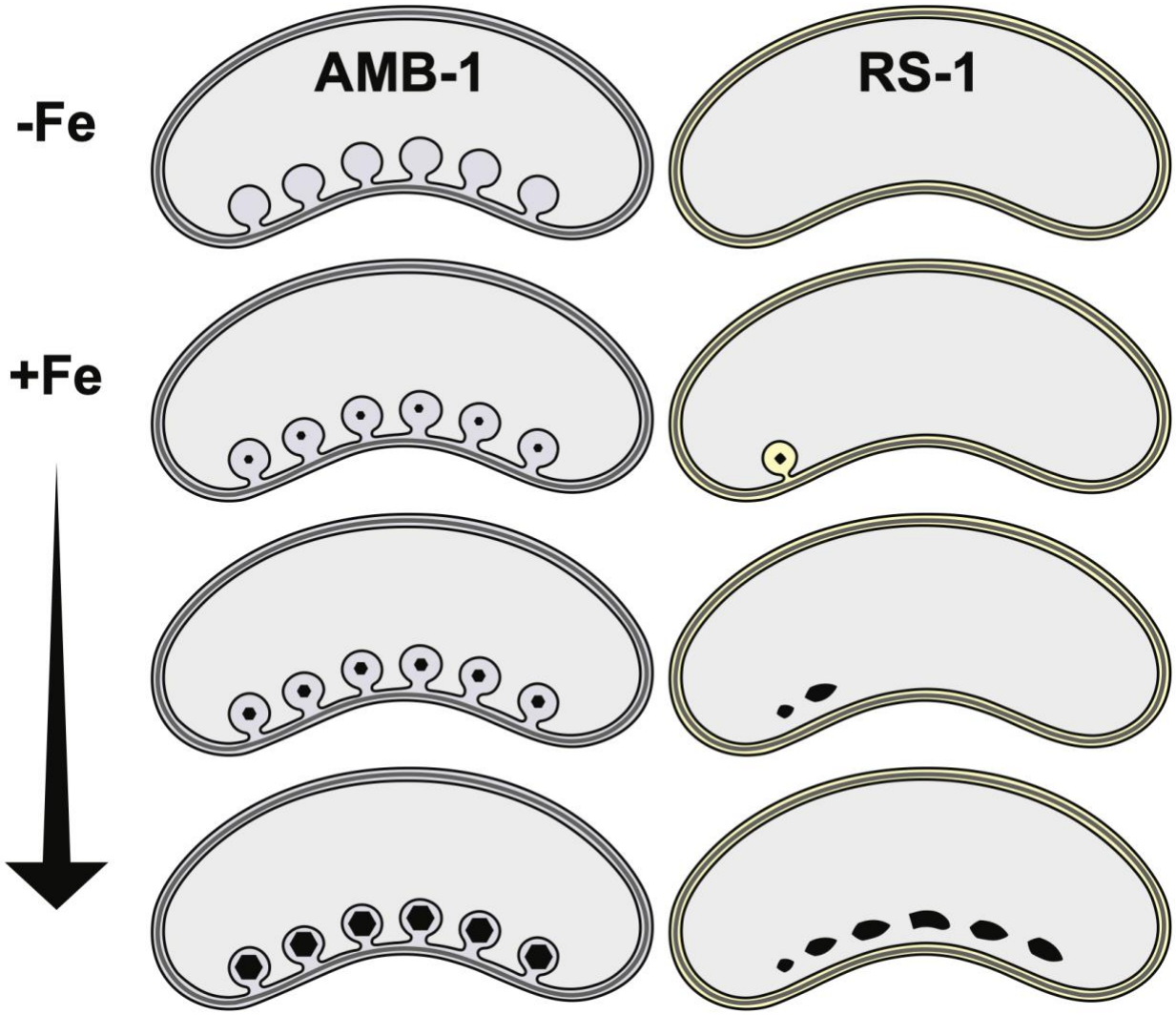

Figure 2. *Differences in biomineralization*

Model of differences in stages of biomineralization post iron starvation. In AMB-1, the synthesis of crystals occurs simultaneously, while in RS-1, they are produced sequentially, indicating that a markedly different process governs the formation of magnetosomes in RS-1.

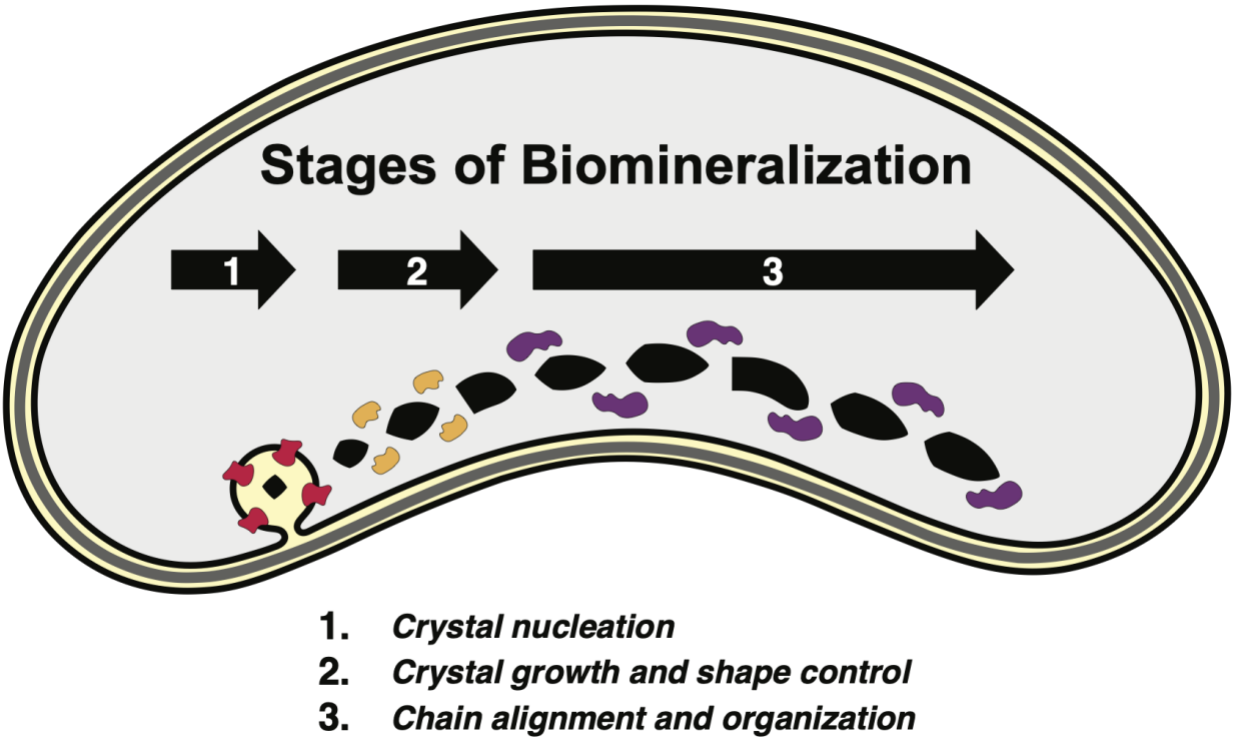

Figure 3. *Steps of biomineralization in Desulfovibrio magneticus RS-1*

Model of the different stages of biomineralization in *Desulfovibrio magneticus* RS-1. The stages are as follows: 1) Crystal nucleation where crystal synthesis is initiated. 2) Crystal growth and shape and control, where the ongoing growth as well as the dimensions and form of the crystals, are governed by a specific suite of magnetosome proteins until crystal maturation. 3) Chain alignment and organization the systematic organization of magnetosomes into a chain along the cell's positive curvature, which is directed by a distinct array of proteins.

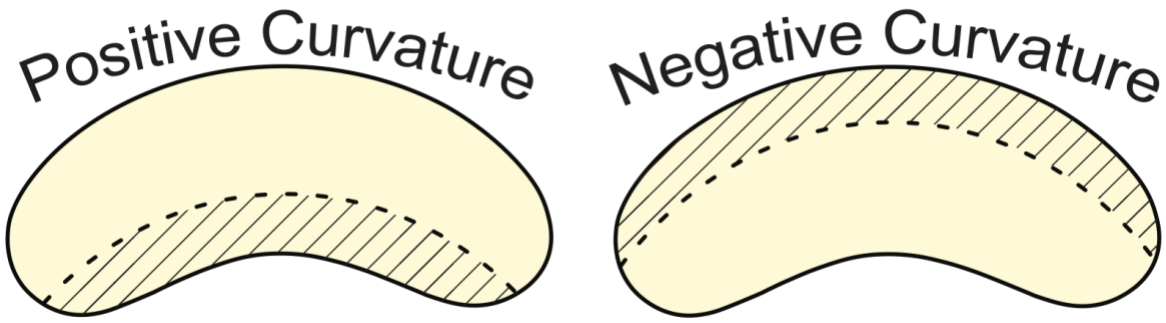

Supplemental Figure S1. *Positive vs. Negative curvature of a cell*

Model showing the location of the positive curvature of a cell in comparison to the negative curvature of a cell. The magnetosome chains are located at the positive curvature of the cell for RS-1, AMB-1 and MSR-1.

Chapter 2

Mad for magnetosomes: Uncovering the mechanism for synthesizing and organizing tooth-shaped magnetosomes in *Desulfovibrio magneticus* RS-1

Virginia V. Russell[1], Anthony T. Iavarone[2], Ertan Ozyamak[3], Carly Grant[4] and Arash Komeili[1]

[1] Plant and Microbiology, University of California Berkeley, Berkeley, California, USA.
[2] QB3/Chemistry Mass Spectrometry Facility, University of California Berkeley, Berkeley, California, USA.
[3] Bio-Rad Laboratories, Hercules, California, USA
[4] Entrepreneurship Program, UCSF Rosenman Institute, San Francisco, California, USA

Section 1: Abstract

Magnetotactic Bacteria (MTB) are a diverse group of bacteria capable of navigating along the geomagnetic field in search of the optimal environment. To do this they synthesize magnetosomes, an organelle composed of magnetite or greigite usually enclosed in a lipid membrane. Studies into the molecular mechanisms for magnetosome formation have been almost exclusively limited to two closely related species of alpha-Proteobacteria, which produce cubooctohedral-shaped magnetite crystals surrounded by a lipid membrane. In contrast, little is known about the mechanisms for synthesis of tooth-shaped magnetosomes, which are thought to be the ancestral form of magnetosomes. Here, we use *Desulfovibrio magneticus* RS-1, a delta-Proteobacterium, as a model organism to uncover distinct mechanisms of magnetosome formation in deep-branching MTB. We first devised a method to visualize different stages of biomineralization in RS-1. When cells are grown in the presence of hydrogen magnetosomes are not formed while iron uptake is not impacted. Once hydrogen is replaced with nitrogen, magnetite biomineralization is initiated and proceeds synchronously within the culture. We find that early in the biomineralization cycle cells contain predominantly equidimensional crystals which then grow in length and adopt the characteristic tooth shape. We also find that chain formation proceeds in step with biomineralization such that early in the cycle cells have one or a few crystals and in later stages adopt the characteristic long chains composed of multiple smaller sub-chains. Immature crystals can be found in any location within the cell while mature crystals are localized to the positive curvature. Using proteomics, we show that different populations of proteins are associated with magnetosomes collected at early versus late biomineralization stages. MamA, MamB, MamEO, FmpA, FmpB, Mad4 and Mad10 are more abundant at the early stages of biomineralization, whereas Mad20, Mad23, Mad28, as well as MamK, are more abundant at the late stage of biomineralization. We then used genetics to see if these different cohorts of proteins play distinct roles in magnetosome chain formation. *fmpA* and *fmpB* mutants display severe defects in the early stages of magnetosome production, do not localize to the positive cell curvature, and cannot form longer chains. On the other hand, deletion mutants of *mad10*, *mad20, mad23, mad25, mad26, mad28* and *mamK* displayed a variety of defects in chain organization. Importantly, MamK and Mad28, both of which encode for actin-like proteins perform distinct functions in chain formation. MamK, limits the number of magnetite particles formed and helps to spread smaller sub-chains across the cell length. Mad28 is responsible for localizing the chain to the positive cell curvature. Based on these results, we propose a model that RS-1 produces magnetosomes consecutively using the early biomineralization genes and actively transports these crystals to the positive curvature of the cell to construct a mature magnetosome chain. Notably, this mode of chain organization is substantially different from that found alpha-Proteobacterial MTB, highlighting the importance of direct molecular genetic study of magnetosome formation in deep-branching MTB model systems.

Section 2: Introduction

Magnetotatic Bacteria (MTB) are a diverse, ubiquitous group of microorganisms capable of navigating along the Earth's geomagnetic field in search of the optimal low to no oxygen environments. This behavior, termed magneto-aerotaxis, is mediated by a specialized organelle, the magnetosome. A typical magnetosome consists of a lipid bilayer membrane with a unique set of proteins that synthesizes and encloses a magnetic crystal, 50-70 nm in diameter, composed of either magnetite (Fe_3O_4) or greigite (Fe_3S_4) (*6*, *30*). Depending on the species, magnetosomes are usually present as single or multiple chains that maximize the magnetic dipole moment of the

cell allowing it to align with external magnetic fields (*5*). The fascinating biological features of magnetosomes have made MTB models for the mechanistic study of organelle formation and biomineralization in bacteria. These studies have in turn fueled an explosion of metagenomic and ecological surveys that hint at a deep history of diverse MTB on Earth and their potentially outsized impact on present-day biogeochemical cycles of iron. However, the narrow selection of current model systems has created a barrier to understanding the mechanistic diversity and evolutionary trajectory of magnetosome formation.

All known MTB are a polyphyletic group of microorganisms that belong to four subdivisions of Proteobacteria (Alpha-, Gamma-, Eta- and Delta-Proteobacteria) and the phyla of Nitrospirae, Omnitrophica and Elusimicrobiota (*6*, *10*, *11*) (Figure 1B). Metagenomic analysis has suggested Latescibacteria and Planctomyetes phyla may also contain MTB species (*12*). The phylogenetic diversity of MTB is matched by a dazzling array of phenotypic variations. The geometry of the crystals, cell morphology, oxygen preference, chain organization, quantity of magnetosomes per cell, and crystal composition can vary amongst different groups of MTB (*5*). Based on extensive surveys, there seems to be a correlation between phylogeny and crystal shape. For example, alpha-Proteobacteria are known to biomineralize cubooctahedral and elongated prismatic magnetite crystals (*5*), whereas all known delta-Proteobacteria and other deep-branching MTB (Nitrospirae, OP3 and Elusimicrobiota) synthesize irregular tooth-shaped magnetite crystals, suggesting that tooth-shaped crystals are the ancestral form of magnetosomes (Figure 1B).

Despite the discovery of numerous magnetotactic bacterial species, research into the genetic basis of magnetosome formation has been limited to only a two species of alpha-Proteobacteria (*Magnetospirillum magneticum* AMB-1 and *Magnetospirillum gryphiswaldense* MSR-1). This work has identified a large number of genes contained within a discrete magnetosome gene cluster (MGC). The MGC is typically around 100 kilobases long and, depending on the species, contains somewhere between 50 to 100 genes, 32 of which are necessary and sufficient for magnetosome formation (*31*). Molecular genetic studies have shown that MGC genes participate in distinct steps to form and localize proteins to the magnetosome membrane, initiate and control magnetite biomineralization, and direct the subcellular arrangement of magnetosomes into chains. Of these 35 genes, only a core set of 8 magnetosome genes, *mamA, B, I, K, M, E, O*, and *Q*, are shared among all MTB (*8*). In fact, many of the genes necessary for critical steps of magnetosome formation in the alpha-Proteobacteria are absent from other MTB. Other sets of conserved genes, called *mad* (**ma**gnetosome **d**eep branching) are found in all deep-branching MTB and *man* (**ma**gnetosome **n**itrospirae) genes are found in Nitrospirae MTB. The phylogenetic distribution of magnetosome genes suggests that group specific *mad* and *man* genes are responsible for the unique phenotypes of deep-branching MTB. However, only a handful of MTB outside of the alpha-Proteobacteria are in culture and practically none have established genetic systems. As a result, very little is known about the function of *mad* genes or the production of irregular, tooth-shaped magnetosomes.

The most promising candidate as a model for deep-branching MTB is *Desulfovibrio magneticus* RS-1. RS-1 is a sulfate reducing obligate anaerobe, belongs to the delta-Proteobacteria class and synthesizes a single chain of irregular tooth-shaped magnetite magnetosomes. The chain is localized to the positive curvature (Supplemental Figure S4 E) of the cell and it is displayed along the entire length of the cell with gaps in between sets of contiguous crystals (Figure 2D*ii*). RS-1 is one of a handful of cultured MTB outside of the alpha-Proteobacteria phylum with a sequenced genome and the only deep-branching organism with a toolkit for heterologous gene expression and targeted genome editing (*25*, *26*). Previous

studies of RS-1 have highlighted a number of unusual features setting it apart from the commonly studied MTB. First, RS-1 produces tooth-shaped crystals whose biomineralization mechanisms are currently unknown. Tooth-shaped crystals account for the majority of magnetism in natural environments highlighting the importance of investigating the molecular basis for their production. Second, previous work has suggested that unlike the alpha-Proteobacterial models, mature magnetite crystals of RS-1 are not surrounded by a lipid membrane (*24*). However, the RS-1 MGC contains numerous conserved MGC genes that encode transmembrane domain-containing proteins. Forward genetic studies have shown that mutations in some of these genes disrupt magnetite formation suggesting that a magnetosome membrane must be present at some stage of biomineralization (*25*). Finally, like all deep-branching MTB, RS-1 contains a large number of *mad* genes, the majority of which have no known functions.

Here, we conduct a comprehensive characterization of the RS-1 biomineralization process using proteomics and genetics to define new pathways of magnetosome formation in deep-branching MTB. Using a conditional biomineralization assay, we identify intermediates in the growth and subcellular localization of magnetosomes in RS-1. We next show that different subsets of proteins are enriched on magnetosomes during various stages of biomineralization. Finally, using genetic analysis, we uncover a suite of *mad* and *mam* genes involved in the development of the RS-1 magnetosome chain. In particular, we show that MamK and Mad28, two actin-like proteins encoded by the RS-1 MGC, have separate functions in organizing the magnetosome chain and localizing it to the positive curvature of the inner cell membrane. These findings stand in stark contrast to the established models of magnetosome formation and highlight the divergent evolutionary paths taken by phylogenetically distinct groups of MTB.

Section 3: Results

3.1 Hydrogen inhibits magnetosome synthesis

Our first goal was to develop a robust system to visualize the progression of magnetosome formation and chain organization in RS-1. In other MTB, growth under iron-limiting conditions inhibits magnetite formation. Addition of iron into the medium triggers biomineralization leading to the synchronized development of magnetosome chains. In RS-1, transition from iron-limited to iron-replete conditions triggers the accumulation of an iron-containing organelle called the ferrosome (*24*). Ferrosomes are electron dense granules composed of iron, phosphorus and oxygen with a possible role in iron storage and detoxification in a variety of organisms (*32*, *33*). Due to their large number and appearance in electron microscopy, the accumulation of ferrosomes makes it nearly impossible to monitor the early stages of magnetosome biomineralization in RS-1. Therefore, we aimed to develop another method to study the steps of magnetosomes formation that did not involve iron limitation.

Serendipitously, we discovered that when RS-1 cells are grown without shaking in a hydrogen rather than nitrogen headspace, the overall magnetic response is dramatically decreased (Figure 2A). Under these conditions, the magnetic response of the culture (measured as the coefficient of magnetism (C_{Mag})) drops as the amount of hydrogen in the headspace is increased (Figure 2A). Since the magnetic response was not completely eliminated, we speculated that cells needed to be exposed to hydrogen throughout the culture medium. Therefore, the headspace and the medium were flushed with 5% hydrogen and cells were grown spinning on a wheel. In this condition, the cultures have no magnetic response as indicated by a

C_{Mag} of 1 (Figure 2C). Transmission Electron Microscopy images confirmed that no magnetosomes are present when RS-1 is grown in the presence of hydrogen (Figure 2D).

One possible explanation for these observations is that hydrogen hinders the growth of RS-1 leading to an indirect inhibition of magnetosome formation. However, growth curve measurements show that RS-1 reaches the same final cell density in hydrogen as compared to nitrogen (Figure 2B). Additionally, cells grown in hydrogen have a faster doubling time (6 hours doubling time) as compared to cells grown in nitrogen (8 hours doubling time) (Figure 2B). Another possibility is that hydrogen inhibits iron uptake thus limiting RS-1's ability to produce magnetosome. To test this possibility, we used the post-iron-starvation accumulation of ferrosomes as a proxy for iron uptake by RS-1. Cells were grown in iron-limited medium with hydrogen and then transferred into iron-replete medium with either nitrogen or hydrogen in the headspace. In post-iron starvation experiments, ferrosomes are present in both nitrogen and hydrogen conditions (Figure 2E *iii* and *iv*), whereas magnetosomes are only present in the nitrogen condition (Figure 2E *iv*). These data show that hydrogen does not inhibit iron uptake.

Lastly, we asked if hydrogen growth lowers or inhibits the expression of magnetosome proteins. To do this, the proteomes of cultures grown in hydrogen or nitrogen were compared by liquid chromatography-mass spectrometry. There was little difference in the abundance of proteins encoded from the MGC with the unusual exception of Mad10 (Figure 2F). Mad10 was over 20 times more abundant in the nitrogen condition in comparison to the hydrogen condition. However, as seen below, Mad10 is not responsible for the inhibition of magnetosome formation in hydrogen conditions. Other proteins outside of the magnetosome gene cluster that are more abundant in the hydrogen condition mostly consist of hydrogenases, along with a response regulator, a signaling protein and the ferric uptake regulator protein, Fur (Supplemental figure S4). In the nitrogen condition de-hydrogenases were more abundant as well as a carbon storage regulator protein (Supplemental figure S4). These differences may indicate the molecular repertoire for hydrogen control of magnetosome formation, a process which we will investigate in the future.

3.2 Observations of early and late stages of biomineralization

Collectively, these data indicate that hydrogen growth conditions inhibit magnetosome formation but do not impact iron uptake by RS-1. Therefore, we hypothesized that a transition from hydrogen to nitrogen growth culture conditions should restore magnetosome formation without the appearance of ferrosome granules that obscure the early stages of biomineralization. To address this, RS-1 was grown shaking with 10% hydrogen to remove all magnetosomes and then transferred into medium with nitrogen in the headspace. In contrast to transition out of iron-limited medium, a shift from hydrogen to nitrogen produces no ferrosomes and only results in magnetosome formation (Figure 2E *i-ii*). As expected, following the transfer into nitrogen-infused medium, the magnetic response of the culture increases over time (Figure 2G). Therefore, hydrogen to nitrogen transfer is a robust tool to synchronize magnetosome formation and study early stages of biomineralization without interference from ferrosomes.

To capture early stages of biomineralization, RS-1 was grown for several passages in bottles with medium infused with hydrogen and incubated shaking. As expected, cultures did not have a magnetic response and individual cells lacked biominerals as assessed by TEM imaging (Figure 2D *i*). Thereafter, cultures were transferred into a medium infused with nitrogen gas. When a reliable magnetic response could be measured (C_{Mag} ranging from 1.05-1.15), cells were harvested by centrifugation and examined by TEM imaging. The early stages of

biomineralization in RS-1 are characterized by the presence of very few magnetosomes in each cell (Figure 3A, Figure 3C), with an average of 3 crystals per cell for over 200 cells counted (Figure 3C). Many of the cells contained mature crystals alongside smaller immature crystals (Figure 3A *ii*). This was also evident when observing the length of each crystal present in these cells (Figure 3D). Although the median for crystal length in this condition is 38 nm, the length for all of the crystals measured in the early stages of biomineralization has a bimodal distribution with two peaks that represent the average immature and mature crystal size (Figure 3D). This feature is also present when calculating the shape factor (width to length ratio) of each crystal measured in the early stages of biomineralization, where there is also a bimodal distribution with one peak around 1 which would represent the immature crystals, and anther peak closer to 2, which would represent the mature crystals (Figure 3E).

During the late stages of biomineralization (C_{Mag} of 1.3-1.5), RS-1 cells harbored complete chains of crystals (Figure 3B), with an average of 12 magnetosomes per cell observed across more than 200 counted cells (Figure 3C), all situated at the positive curvature of the cell. In addition, the average crystal length was 51 nm with an average shape factor of 1.7 (Figure D and E). The distribution for both crystal length and shape factor fit a normal distribution because there were much fewer immature crystals at this stage of biomineralization (Figure 3B and Figure 2G *ii*). Another notable feature of the late stages of magnetosome formation in RS-1 is that the chain is not continuous and is composed of smaller chains which we will refer to as sub-chains for the rest of this report.

To understand process of crystal growth in RS-1 crystal measurements taken from both early and late stages of biomineralization. The pattern that has been observed in other deep-branching MTB is also present in RS-1, where the crystals grow equidimensionally until they reach approximately 30 nm after which they elongate with an anisotropic crystal growth pattern (*34*) (Figure 3G). In addition to crystal measurements, high magnification TEM images of several crystals were captured to visualize the different stages of crystal growth (Figure 3F). Notably, there are two main morphologies of mature magnetosomes, curved and straight (Figure F*ix* and F*x*). Based on these observations we propose different stages of crystal growth: initial, symmetrical, elongation, growth, and maturation. We speculate that during the elongation process, crystals can mature into either a straight or curved form (Figure 3F-*v* and F-*vi*).

Subsequently, while investigating the distinct stages of biomineralization, we also discovered that the cellular location of magnetosomes is correlated with the maturation of the crystal. This is most evident during the early biomineralization stages where nearly all mature crystals are found at the positive cell curvature which marks the location of the magnetosome chain. However, only ~25% of the immature crystals are at the positive cell curvature (Figure 3H and 3I). These results stand in stark contrast to the process of magnetosome formation in alpha-Proteobacterial MTB (*35*). For instance, in AMB-1, magnetosome membranes are assembled into chains at the positive cell curvature even prior to the initiation of biomineralization (*36*). Our data suggest that in RS-1, crystal nucleation does not occur at the positive curvature but instead magnetosomes are synthesized in one location and then localized to their final destination as they mature.

Given the clear progression of magnetosome chain development, we hypothesized that differing sets of magnetosome proteins might be involved at each stage of biomineralization. Therefore, we harvested and lysed cells at early and late stages of biomineralization and separated magnetosomes using a magnetic column. The proteomes of cell lysates and magnetosome fractions at early and late stages were analyzed by liquid chromatography-mass

spectrometry. Since the magnetosome fractions are only enrichments and not deeply purified samples, we focused our analysis on proteins encoded by genes within the RS-1 MGC that were enriched on magnetosomes at the early or late biomineralization stages. One set of MAI (Magnetosome gene Island)-encoded proteins (Mad10, MamB, MamA, Mad4, FmpA, FmpB, and MamEO-Cter) were more abundant in the early biomineralization stage magnetosome fraction as compared to the late stage magnetosome fraction (Figure 3J). A different set of MAI-encoded proteins (Mad20, Mad23, Mad28 and MamK) were more abundant at the magnetosomes in the late stage compared to the early stage (Figure 3J). Many of the proteins that are more abundant at the early stage have annotated transmembrane domains (Supplemental Figure S1), supporting previous hypotheses that even though membranes are not found surrounding mature crystals, they are still important and necessary for the early stages of crystal synthesis. However, none of the late-stage enriched proteins have transmembrane domains, supporting a transition in the physical state and membrane-association of mature crystals. In addition, two proteins more abundant in the late stage, Mad28 and MamK, have actin-like domains (Supplemental Figure S1), leading to the hypothesis that chain alignment and organization is a central step in the late stages of biomineralization.

3.3 Early magnetosome production involves membranes and is not located at the chain

In previous work, we used chemical and UV mutagenesis to enrich for RS-1 mutants with severe defects in biomineralization. This screen yielded several alleles of *mamB* most of which do not have a magnetic response and do not produce crystals (*25*). This result corroborates the proteomic finding that MamB preferentially associates with magnetosomes in early stages of biomineralization (Figure 3J).

Some of the mutants isolated in our previous work can still produce magnetic particles providing us the opportunity to study the link between specific proteins and the early stage of biomineralization. We focused on two mutants in the *fmpA* and *fmpB* genes. In our proteomic analysis, we find that FmpA and FmpB are more abundant at the magnetosome in the early stage compared to the late stage of biomineralization (Figure 3J). These proteins both have transmembrane domains as well as serine protease and denitrogenase Fe-Mo domains (Supplemental Figure S1). To follow up with the previous study, TEM was used to obtain crystal placement and crystal size measurements for both mutants with over 200 cells counted for each. We find that the *fmpA* mutant often has circular or symmetrical crystals (Figure 4A and 4G), whereas the *fmpB* mutant has crystals resembling smaller versions of WT magnetosomes (Figure 4B), although on some occasions they were misshapen and symmetrical as well (Figure 4H). Consistent to what was briefly described previously (*25*), both mutants exhibited significantly fewer crystals per cell, averaging 1.6 and 2.7 crystals per cell for *fmpA* and *fmpB* mutants, respectively, whereas the wild type (WT) had an average of 12 magnetosomes per cell (Figure 4D). Furthermore, both mutants also produced smaller crystals compared to the WT (Figure 4E), with an average length of 35 nm for *fmpA* and 31 nm for *fmpB* crystals, in contrast to the WT's average magnetosome length of 51 nm. Furthermore, both mutants have an average shape factor of 1.3, whereas the average shape factor for WT is 1.7 (Figure 4F).

In addition to the defects in the shape and size of magnetite, these mutants displayed a conspicuous aberration in the placement of the crystals within the cell. The majority of the crystals in both *fmpA* and *fmpB* mutants were not localized to the positive curvature of the cell (Figure 4J). In addition, the crystals in the *fmpA* mutant were never organized in a chain and the crystals in the *fmpB* mutant were only organized in a chain in 5% of the cells counted (Figure

4I). This data leads to the hypothesis that FmpA and FmpB are important proteins for early stages of magnetosome synthesis. Additionally, they show that the initial stages of biomineralization likely do not occur at the positive curvature. Hence, we propose that crystal nucleation occurs at different locations throughout the cell and the crystals are shuttled to the positive curvature post-maturation. It is likely that in the absence of FmpA and FmpB crystals get "stuck" at crystal nucleation sites and are not available to be transported to the site of the magnetosome chain. This stalled translocation prevents the initiation of biomineralization for new crystals leading to the much fewer crystal numbers seen in these mutants (Figure 4D).

Mad10 is another protein that displays an increase in abundance at the magnetosomes in the early stages of biomineralization compared to the late stages. It is also notable for having the largest abundance ration of an MAI protein at the magnetosome as compared to the cell lysate under all biomineralization conditions (Supplemental Figure S7). Previous studies identified Mad10 from various MTB as a magnetite binding protein and hypothesized that it would participate in controlling magnetosome shape (*37*, *38*). To uncover the role of Mad10 in magnetosome production we deleted *mad10* in RS-1. In a Δ*mad10* mutant, the magnetic response is greatly reduced as compared to the WT (Figure 6B), a phenotype that can be trans-complemented by expression of *mad10* from a plasmid (Figure 6B and Supplemental S3). The lower C_{Mag}, however, is not due to a biomineralization defect since the shape and size properties of individual crystals are unaffected in the Δ*mad10* mutant. Instead, we find that in the absence of *mad10* all magnetosomes are aggregated and cluster together at one location in the cell (Figure 5A and 6I). The number of crystals per cell also varies dramatically (Figure 6D), likely due to the asymmetric positioning of the magnetosome clusters in the cell and their unequal distribution to daughter cells during cell division. These results show that Mad10 is not responsible for regulating the size and shape of the crystals but rather plays a crucial role in chain organization (Figure 5A).

3.4 A module for assembly of the magnetosome sub-chains

We next targeted genes encoding proteins found to be more abundant at the magnetosome in late stages of biomineralization (Figure 3J). In addition, some neighboring genes (Figure 1A) that may be part of an operon were also chosen for deletion analysis. All deletions were successfully complemented using heterologous expression of the targeted gene on a plasmid (Supplemental Figure S3 and Figure 6C). These mutants display a variety of defects in organization and placement of magnetosome chains. To facilitate a more quantitative analysis, we created several categories to describe the placement of the chain in the cell, the distribution of magnetosomes across the cell length, the organizational appearance of the chain, and the phenotype of sub-chains (Supplemental Figure S4E-H).

This analysis identified one group of genes, *mad20*, *mad23*, *mad25* and *mad26* as a module responsible for assembly of magnetosome sub-chains in RS-1. Mad20 and Mad23 were both identified in our proteomic analysis as late stage magnetosome-associated proteins (Figure 3J). Mad25 is encoded from the same putative operon and present at the magnetosome in our proteomic analysis. However, unlike Mad20 and Mad23, it is more abundant in cell lysates as compared to magnetosomes in all conditions (Supplemental Figure S7). Finally, Mad26 was chosen as it is encoded by the same putative operon as the other genes (Figure 1A). Deletions of each of these genes result in magnetosomes that are dispersed, not localized to the positive curvature of the cell, often found in a transverse orientation, and not aligned as a chain spanning

the length of the cell (Figure 5 and Supplemental Figure S4). There are also specific phenotypes for each strain that hint at more specialized roles for these proteins.

In the absence of Mad23, for instance, single magnetosomes are dispersed throughout the cell and the number of crystals in a sub-chain is the lowest amongst all other mutants and WT (Figure 5C and Figure 6E and Supplemental Figure S10). Accordingly, the Δ*mad23* mutant has the lowest C_{Mag} amongst all chain organization mutants in our study (Figure 6B). We hypothesize that Mad23 is responsible for connecting individual magnetosomes to form a sub-chain.

The Δ*mad20* mutant, in contrast, contains clear sub-chains, some of which are organized as a linear segment and others appear as rings, clusters, or curved lines (Figure 5B). Intriguingly, this mutant has fewer sub-chains than the WT (Figure 6F and Supplemental Figure S9) with each segment containing more magnetosomes (Figure 6E). Perhaps, Mad20 regulates the influx of new crystals into a sub-chain. In its absence, sub-chains acquire an excessive number of crystals that curl and distort into a ring or curved line (Supplemental figure S9).

The Δ*mad25* and Δ*mad26* mutants have somewhat comparable phenotypes (Figure 5D and 5E). These strains contain similar numbers of sub-chains and crystals as wildtype (Figure 6F and 6D). However, the majority of sub-chains in these two mutants are clustered or present as rings. This is most evident for the Δ*mad26* in which ~80% of sub-chains are clustered and another 15% are in rings (Supplemental Figure S4 D). These severe phenotypes implicate Mad25 and Mad26 in maintaining the overall linear configuration of the magnetosome chain.

Overall, these mutants highlight an organizational pattern for the RS-1 magnetosome chain that is distinct from the commonly studied alpha-Proteobacterial MTB. For instance, in AMB-1, sub-chains of magnetic particles are observed via TEM. However, magnetosome membranes are still organized as a chain in these species (*39*). Additionally, chain organization mutants do not have the sub-chain-related phenotypes and mutants with a distorted chain generally have one cluster or ring in the cell. In RS-1, some mutants can have multiple clusters, rings or curved sub-chains in the same cell. Thus, we argue that sub-chains are a fundamental organizational unit of the magnetosome chain in RS-1. Proteins like Mad20, Mad23, Mad25, and Mad26 work together to set the length of individual sub-chains and to ensure their overall stability. All of these proteins, as well as Mad10, contain one or multiple coiled-coil domains (Supplemental Figure S1 and S2) hinting at cytoskeletal features and an interaction network to organize the chain. Finally, we note that in all of these mutants, localization of magnetosomes to the positive curvature of the cell is disrupted. Thus, sub-chain organizing proteins may also interface with factors mediating the placement of magnetosomes at the positive cell curvature.

3.5 The role of chain and sub-chain placement directed by Mad28 and MamK

Subsequently, Mad28 and MamK were chosen for genetic analyses because they are both more abundant at the late stage of biomineralization at the magnetosomes (Figure 3J), and because they both have actin-like domains (Supplemental Figure S1). *mamK* is a gene found in nearly all MTB and has a well described function in both AMB-1 and MSR-1 (*40–42*). Deletion of *mamK* in AMB-1 leads to a loss of cohesion in the chain (*41*), where large gaps appear between groups of magnetosomes. These gaps also lead to lateral diffusion and mobility of magnetosomes which compromises their equal distribution during cell division (*43*). The deletion of *mamK* in MSR-1 has a more dramatic phenotype, where the chain is no longer localized to the mid-cell in the majority of cells (*44*). Nevertheless, studies on both AMB-1 and MSR-1 have demonstrated the significance of MamK in orchestrating the arrangement of

magnetosomes, and ensuring equal distribution of magnetosomes among daughter cells (*39*, *42*, *43*). Similar to these results, we find that MamK in RS-1 also plays a role in chain organization. In RS-1 Δ*mamK* mutant, magnetosome sub-chains are no longer observed (Figure 6F). Instead, magnetosomes are organized as one long continuous chain (Figure 5G) that in some cases are so long that it wraps around itself and appears as multiple chains. Additionally, there are more crystals on average in Δ*mamK* cells in comparison to WT (Figure 6D). RS-1 contains another magnetosome gene that also encodes an actin-like domain, *mad28* (*8*, *28*) (Supplemental Figure S1) that is found in all deep-branching MTB. Previous studies have hypothesized that it might play a similar role as MamK in chain organization (*28*). However, when we delete *mad28*, the mutants have a distinct phenotype from the Δ*mamK* strain. Δ*mad28* has a linear chain with sub-chains as seen in WT, but the chain is no longer localized to the positive curvature of the cell (Figure 5F). The chain has a few different arrangements including pole to pole in the middle of the cell, diagonal line, or transverse line as seen in Figure 7. Therefore, Mad28 is required for positioning the chain at the positive curvature of the cell, whereas MamK is responsible for organizing the sub-chains along the length of the cell.

To examine the differences of chain organization in Δ*mad28* and Δ*mamK* mutants further, we did a biomineralization time course experiment as described above. Monitoring different stages of biomineralization allowed us to visualize how the chains were organized as it was forming in both mutants. In Δ*mad28*, the chain assembly process resembles that of WT. Initially, a single mature crystal is observed, followed by the formation of sub-chains as the number of mature crystals increases in the cell. Subsequently, additional crystals are incorporated into the sub-chains as biomineralization proceeds (Figure 7A, B and C). The only difference between chain formation in Δ*mad28* and WT is the placement of the chain even at the earliest stages of biomineralization (Figure 7A, B and C). Figure 7B shows the chain formation of Δ*mad28* when the chain is located pole to pole but in the middle of the cell and Figure 7C demonstrates the process of chain formation in Δ*mad28* when the chain forms in a transverse or diagonal position in the cell. In contrast, the chain of Δ*mamK* forms very differently (Figure 7D). The first stages in biomineralization of Δ*mamK* looks similar to WT, but as more mature crystals start to form the process of chain organization starts to differ. Instead of sub-chains forming, new mature crystals are added to the same chain and sub-chains are never observed (Figure 7D). In addition, Δ*mamK* has significantly more magnetosomes in each cell at both stages of biomineralization (Figure 7E and F) and the C_{Mag} for this mutant is greater than WT (Figure 6B and C). This is an unusual phenotype for MamK that has not been observed in other MTB *mamK* mutants (*41*, *44*). Additionally, when complementing *mamK* on a plasmid, cells now have fewer magnetosomes in comparison to WT, with a lower C_{Mag} than WT (Figure 6C). This is possibly because the expression of *mamK* is not controlled in the same manner when it is on a plasmid as it would be natively in the chromosome. The biomineralization time course of Δ*mamK* and Δ*mad28* allowed us to have a better idea of how these proteins are affecting chain organization in RS-1. This data indicates that Mad28 is involved in aligning magnetosomes towards the positive curvature of the cell starting at the early stages of chain formation, while MamK is responsible for distributing the sub-chains of magnetosomes along the cell's length to ensure the magnetosome chain spans from one pole to pole. Additionally, MamK may play a role in regulating the amount of magnetosomes produced.

Section 4: Discussion

With the rapid expansion of genomic and metagenomic studies (*8*, *11*, *45*), it has become clear that major differences exist between the genetic components of magnetosome formation in various phylogenetic families of MTB. In this study, we developed a new workflow to monitor the process of biomineralization in *Desulfovibrio magneticus* RS-1 and use proteomic and genetic analyses to reveal a mode of organelle assembly distinct from commonly studied models of MTB. Our work underscores the importance of developing a diversity of model systems even for processes that share a seemingly common evolutionary origin.

A key breakthrough in our work was the discovery that RS-1 magnetosome formation is inhibited in the presence of hydrogen. A similar phenotype is also observed in *Magnetospirillum magneticum* AMB-1 and *Magnetospirillum gryphiswaldense* MSR-1 in which elevated oxygen concentrations lead to the cessation or significant reduction in magnetosome production (*46*, *47*). Thus far it is unclear if the inhibition of magnetosome formation in these cases is due to differential regulation of the expression or activity of some genes. For AMB-1 and MSR-1, magnetosome proteins are still present even though magnetosomes are not synthesized (Schübbe et al., 2006). Similarly, magnetosome proteins in RS-1 seem to be present under hydrogen or nitrogen growth conditions (Figure 2F). However, our proteomic analysis may have missed some magnetosome proteins and is not sensitive enough to catch small changes in protein abundance. In the future, we plan to analyze global gene expression under hydrogen and nitrogen growth conditions and use genetic analyses to identify potential genes involved in this magnetosome formation switch. We also note that the lack of magnetosomes is not due to growth inhibition as RS-1 grows even faster under hydrogen conditions (Figure 2B). Additionally, iron uptake is not affected since RS-1 can still make ferrosomes, iron-rich granules, during hydrogen growth (Figure 2E).

While mechanisms or selective advantages of hydrogen-mediated magnetosome inhibition are unknown, it provides a powerful method to track biomineralization from its earliest starting points. Previously, the synchronization of biomineralization relied on addition of iron to iron-starved cells. However, this method triggers the production of ferrosomes, which makes it impossible to identify immature magnetosomes. Using the hydrogen to nitrogen switch, we replicated aspects of previous iron addition studies which mainly monitored mature crystals. Most importantly, our results are consistent with previous findings that RS-1 cells produce magnetosomes one or a few crystals at a time (*24*, *25*). Furthermore, we show that magnetite particles grow symmetrically until they reach a length of approximately 30 nm. After this point, the crystals grow in length but not width until they reach their characteristic elongated tooth-shape (Figure 3G). We also find that the initial stages of biomineralization occur at sites that are distinct from the final location of the chain. Once a crystal attains a specific size, it is localized to the chain at the positive cell curvature. These features are distinct from alpha-Proteobacterial MTB. In AMB-1, for instance, magnetosome membranes are located at the positive cell curvature even prior to biomineralization (*36*). When biomineralization is triggered multiple adjacent magnetosomes initiate biomineralization simultaneously. These differences in the mode of biomineralization and the assembly of magnetosome chains suggest the existence of a distinct mechanistic pathway for magnetosome formation in RS-1. We identified some of these factors using differential proteomic analysis of magnetosomes from RS-1 cells at early and late biomineralization stages.

In previous studies, we have failed to detect lipid membranes surrounding mature crystals in RS-1 (*24*). However, we had also identified mutations in transmembrane domain-containing magnetosome genes that abolished or significantly impacted magnetosome formation indicating

that membranes are needed at some stage of biomineralization (*25*). Our proteomic analysis supports this model since most MAI-encoded proteins enriched on early stage magnetosomes are predicted to contain transmembrane domains (Figure 3J and Supplemental Figure S1). Two of these membrane proteins are FmpA and FmpB. The mutants for *fmpA* and *fmpB* have statistically fewer crystals and the majority of those crystals are not located at the positive curvature of the cell (Figure 4D and J). These results link specific factors to the general observations of biomineralization progression. Namely, the one-by-one biomineralization of magnetite and localization to the positive curvature are both blocked in *fmpA* and *fmpB* mutants.

Mad10 is another protein that is abundant at the early stages of biomineralization. In fact, it is the most abundant MAI-encoded protein at the magnetosome fraction in comparison to the whole cell lysate fraction (Supplemental figure S7). Previous work had hypothesized a role for Mad10 in control of magnetite size or shape. However, we do not observe a biomineralization defect in a Δ*mad10* mutant. Instead, the particles are aggregated in a single cluster within the cell. Hence, we propose that Mad10 coats magnetic particles and serves as a tether to facilitate interactions between magnetite and other proteins. Curiously we also find that Mad10 is found at a much higher abundance in nitrogen conditions as compared to hydrogen conditions (Figure 2F). We hypothesize that Mad10 is overproduced prior to biomineralization in order to mediate interactions with the crystals and prevent their aggregation as soon as they are formed. That is likely why it is more abundant at the early stages. In addition, Mad10 might be regulated by biomineralization (Figure 2F).

Mad28 and MamK are two bacterial actin-like proteins that are more abundant at the magnetosomes at the late stage in comparison to the early stages of biomineralization. MamK has been shown to be involved in centering magnetosome chains in the alpha-Proteobacterial MTB to ensure its equal segregation during cell division. In contrast, the loss of MamK in RS-1 results in an overproduction of magnetosomes and the loss of separation between sub-chains. Despite these differences, at least one general function of MamK in all organisms tested may be to ensure the most efficient distribution of magnetosomes to form a centered chain within the cell. Previous studies do provide some support for a conserved MamK function. For instance, RS-1 MamK is able to partially complement the Δ*mamK* mutant of MSR-1 (*28*). This study also found that Mad28 from several deep-branching species can partially complement the loss of MamK in MSR-1. In our work, we find that the phenotype of Δ*mamK* is distinct from that of Δ*mad28*. In the absence of Mad28, a full chain composed of multiple separated sub-chains is found in nearly all cells. However, the chain does not localize to the cell's positive curvature. These results further punctuate the power of studying magnetosome genes directly in diverse organisms.

In conclusion, this study has significantly enhanced our understanding of the mechanism behind magnetosome synthesis and organization in *Desulfovibrio magneticus* RS-1. We propose the stages for biomineralization in RS-1 are as follows. Step one involves crystal nucleation, which does not take place at the positive curvature of the cell (Figure 8*i*) and instead is distributed to a few sites at different positions. In step two, the crystals are continuing to grow at the site where crystal nucleation occurs (Figure 8*ii*). Previously, we have hypothesized that these sites are a membrane-limited magnetosome factory. In step three, crystals near maturation are transported to the positive curvature of the cell (Figure 8*iii*). During this stage, it is likely that Mad10 coats the crystal to facilitate the interaction of chain organization proteins as the crystal transitions from the synthesis site to the chain assembly site. After Mad10 coats the crystal, Mad28, with the possible assistance of other proteins, can interact with the magnetosome and

direct it to the positive curvature of the cell (Figure 8*iii*). As crystals are transported to the positive curvature of the cell, the biomineralization process transitions into chain organization. During the initial phases of chain organization, specifically in step four, we detect one or two mature crystals at the positive curvature (Figure 8*iv*). As more than one crystal converge, Mad23 connects them, initiating the formation of the sub-chains. In step five, additional sub-chains form (Figure 8*v*) and are distributed along the length of the cell by MamK. Ultimately, in step six, additional crystals are continuously incorporated into the existing sub-chains to form the completed magnetosome chain (Figure 8*vi*). The suggested mechanism for magnetosome synthesis and organization in RS-1 differs significantly from the established mechanism observed in both AMB-1 and MSR-1, underscoring the importance of studying magnetosome formation across a broader spectrum of magnetotactic bacterial species.

Section 5: Methods

5.1 Multiple-sequence alignments and tree construction

Data set was designed by first searching for all known MTB by searching IMG/M ER for species with homologs for all five of the core *mam* genes selected: *mamK*, *mamA*, *mamB*, *mamM* and *mamQ*. Next, the dataset was refined to encompass only species with available genomes and accessible TEM images, enabling the identification of magnetosome gene sets (*mam*, *mms*, *mad* and *man*) for each species, along with their respective crystal shapes and compositions. Supplemental table 1 is a list of all species included in designing the phylogenetic tree for this analysis. Once the data set is the assembled DNA sequences of 16S for each species obtained from NCBI or IMG-M (*49*) (Supplemental table 1). Sequences were aligned using MAFFT version 7.490 using the scoring matrix 1PAM/ k=2 (*50*). Next, the aligned sequences were used to generate the maximum likelihood tree using PhyMLTree version 3.3.20180621 using GTR substitution model with 1000 bootstraps (*51*). Additionally, the tree was rooted with *Omnitrophus magneticus* SKK-01.

5.2 General Culturing for RS-1

Desulfovibrio magneticus RS-1 strains were grown at 30°C anaerobically in RS-1 growth medium (RGM), as described previously (*24*, *25*). For growth with hydrogen, the medium was gassed with 10% hydrogen balanced with Nitrogen prior to autoclaving the medium. Additionally, after inoculating, the headspace was re-gassed with the same concentration of hydrogen/nitrogen gas mixture for 10 minutes. All hydrogen cultures were grown spinning on a wheel in the 30°C incubator. Only nitrogen cultures that were used as controls for hydrogen cultures were grown on a wheel in the incubator; all other nitrogen cultures were grown without shaking.

5.3 Culturing for growing RS-1 in different concentrations of hydrogen

RS-1 WT strain was grown at 30°C anaerobically in RS-1 growth medium (RGM), as described above. Initially, all culture tubes were purged with nitrogen gas. Subsequently, prior to inoculation, varying volumes of nitrogen from the headspace were displaced and substituted with an equivalent volume of 100% hydrogen gas, aiming to achieve distinct concentrations of

hydrogen in the headspace. Afterwards, RS-1 was inoculated into the culture tubes. Optical density and magnetic response via C_{Mag} was monitored throughout growth as previously described (*25*).

5.4 Culturing for proteomics

Culture for hydrogen vs. nitrogen consisted of 350 mL cultures with 2/3 volume of headspace, which were prepared by gassing either with nitrogen or 10% hydrogen and grown shaking at room temperature. At late exponential phase cultures were harvested by centrifugation at 8,000 rpm using the Beckman Model J2-21M/E centrifuge. Cell pellets were stored at -80°C until it was time to lyse and prepare samples for proteomic analysis. For culturing for different stages of biomineralization, 300 mL initial cultures were grown with hydrogen in the headspace to remove all magnetosomes. C_{Mag} was measured and TEM images were taken of initial cultures to ensure no magnetosomes were present. Then 10 1L bottles of RGM-X medium was prepared by infusing the medium with nitrogen and gassing the headspace with nitrogen. Each biological replicate consisted of 10 1L bottles, which was inoculated with the same starting culture. Three of those bottles were used for late biomineralization, which were inoculated with 10 mL of starting culture, and seven bottles were used for early biomineralization samples, which were inoculated with 20 mL of the starting culture. The cultures were grown in a 30°C incubator and ODs and C_{Mag}s were taken 2X daily. When cultures had a C_{Mag} of 1.05-1.15 seven of the bottles were harvested for early biomineralization samples by centrifugation at 8,000 RPM. Subsequently, when the final 3 bottles had a C_{Mag} between 1.30-1.5 they were harvested for late stages of biomineralization samples also by centrifugation at 8,000 RPM. Cell pellets were stored at -80°C until it was time to prepare samples for proteomics. This was repeated 2 times for the three biological replicates, so in total 30L of culture was used to prepare samples for the proteomics (for each run). Each biological replicate came from a different starting colony of RS-1, but the 10 1L bottles that represented one biological replicate had an inoculum that originated from the same starting colony.

5.5 Collecting proteins associated with magnetosomes using a magnetic column

After harvesting cultures, cell pellets were resuspended in buffer A (25 mM Tris, pH 7.0, 100 mM sucrose, 1000 mg/mL Leupeptin, 1000 mg/mL Pepstatin A, and 10 M PMSF. Then cells were lysed using a single shot (reference?). Afterward, the cell lysate were passaged through a magnetic column to separate the magnetosomes from the entire cell lysate. Initially, magnetic columns underwent a wash with buffer A, followed by the attachment of magnetics to the columns. Subsequently, the cell lysate was passed through the column. After three cycles of passing the cell lysate through the column, buffer A was used for three additional washes. Following these wash cycles, the magnets were detached from the column, and 500 µL of buffer A was pipetted into the column. The column was then plunged to use force to collect all of the magnetosomes. Some of the cell lysate from each sample was also saved as a control. Next, a Bradford assay was conducted on all samples to determine the protein concentration, and if necessary, samples were concentrated during this stage. Lastly all samples were trypsin digested to prepare samples for liquid chromatography-mass spectrometry.

5.6 Liquid chromatography-mass spectrometry

Trypsin-digested protein samples were analyzed using an Acquity M-class ultra-performance liquid chromatography (UPLC) system that was connected in line with a Synapt G2-Si mass spectrometer (Waters, Milford, MA) as described elsewhere . Data acquisition and analysis were performed using MassLynx (version 4.1, Waters) and Progenesis QI for Proteomics software (version 4.2, Waters Nonlinear Dynamics). Data were searched against the *Desulfovibrio magneticus* strain RS-1 translated protein database to identify peptides.[2]

5.7 Plasmid and cloning and deletion

All plasmids used in this study for generating deletions as well as for the complementations are listed in Supplemental table 3. In-frame deletion vectors targeting *mad10, mad20, mad23, mad25, mad26 mad28* and *mamK* were constructed by amplifying upstream and downstream homology regions by amplifying RS-1's genomic DNA, using the primers listed in Supplementary Table 3. The homology regions were then inserted into the XbaI site of pAK1127 using the Gibson cloning method. Next, the P*npt -strAB* cassette was subsequently inserted between the upstream and downstream homology regions of the deletion vector. Plasmids were transformed into E. coli WM3064 and then transferred to *D. magneticus* RS-1 using conjugation methods as described previously (*26*). Allelic replacement of *mad10, mad20, mad23, mad25, mad26 mad28* or *mamK* with *strAB* was achieved with streptomycin selection and using two counterselections, 5-Flurouracil and sucrose. All deletions were confirmed by PCR followed by full genomic illumina sequencing.

5.8 Biomineralization time course using hydrogen

RS-1 strains were grown at 30°C anaerobically, as described above. Initial cultures were all grown with medium infused with 10% hydrogen and after inoculation headspace was purged with 10% hydrogen. The hydrogen cultures were all grown on a wheel in the incubator. Additionally, all cultures were transferred for supplementary growth into hydrogen tubes to ensure the removal of all magnetosomes. After growth in hydrogen cultures, they were transferred into nitrogen-infused medium with varying volumes of initial inoculum added into the nitrogen experiment tubes (1mL, 0.5 mL, 0.2 mL, and 0.1 mL), aiming to capture all stages of biomineralization more effectively. Optical density and magnetic response via C_{Mag} was monitored throughout growth as previously described (*25*) and at different stages of biomineralization samples were saved for TEM imaging. The progression of biomineralization stages was tracked using C_{Mag}, with C_{Mag}s ranging from 1.05 to 1.10 classified as early stages, 1.15 to 1.20 as middle stages, and 1.3 to 1.6 as late stages.

5.9 Electron microscopy

Whole-cell TEM imaging was performed as described previously (*24*). All TEM was done using the Tecnai 12 at the EM-Lab at the University of California, Berkeley. Magnetosomes were measured manually using ImageJ. Cells were also counted manually.

Section 6: Acknowledgement

A.K. and V.V.R. are supported through the National Institute of General Medical Sciences (R35GM127114). The QB3/Chemistry Mass Spectrometry Facility at the University of California, Berkeley received support from the National Institutes of Health (grant 1S10OD020062-01). Additionally, V.V.R. is supported through the Genetics Training Grant, which receives funds from the National Institutes of Health (Grant #: 1T32GM132022).

Thank you to the staff at the University of California Berkeley Electron Microscope Laboratory for advice and assistance in electron microscopy.

Figures

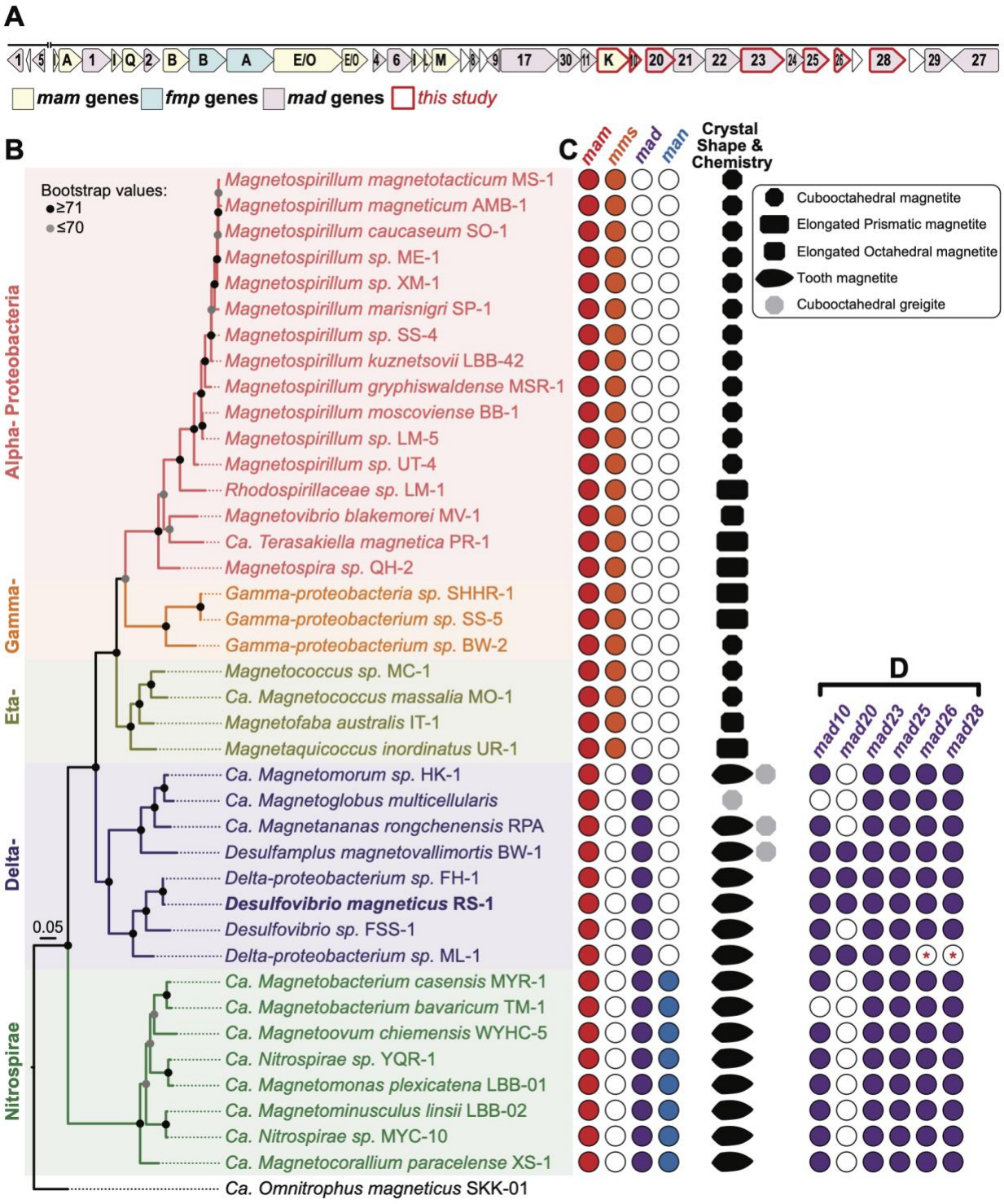

Figure 1. *Phylogenetic Tree of MTB with magnetosome genes and crystal shape data*

(A) Magnetosome gene cluster in RS-1. All *mam* genes are in yellow, all *mad* genes are in purple and *fmp* genes are in blue. Genes outlined in red (*mamK*, *mad10*, *mad20*, *mad23*, *mad25*, *mad26*

and *mad28*) are genes from this study. (B) 16S maximum likelihood tree. MAFFT was used for alignment of 16S genes. Maximum likelihood tree was built using PhyML Tree (*51*) with GTR substitution model and 1000 bootstraps. (C). For each MTB species the classification of the type of magnetosome genes (*mam*, *mms*, *mad* or *man*) are provided as well as the magnetosome chemical composition and shape. *Supplemental table 1* shows where that data was gathered from, NCBI genome ID and literature with crystal TEM images and description. (D). Shows which deep-branching MTB species that contain the *mad* genes in this study.

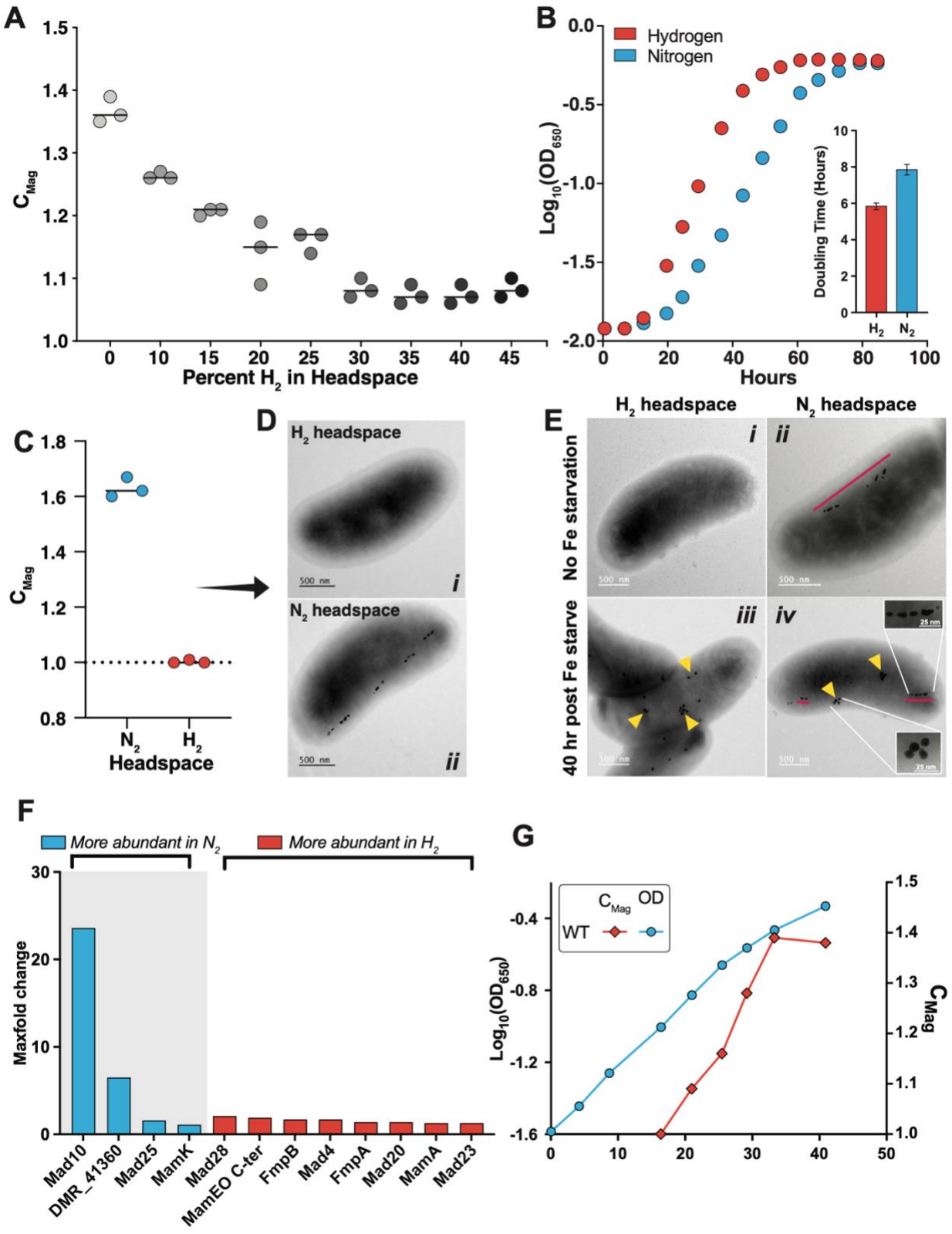
A
B
C
D
E
F
G
Percent H2 in Headspace
Hydrogen
Nitrogen
Hours
Doubling Time (Hours)
H2 headspace
N2 headspace
Headspace
No Fe starvation
40 hr post Fe starve
More abundant in N2
More abundant in H2
Maxfold change
Mad10
DMR_41360
Mad25
MamK
Mad28
MamEO C-ter
FmpB
Mad4
FmpA
Mad20
MamA
Mad23
WT

Figure 2. *Hydrogen inhibits magnetosome synthesis but not Ferrosome production*

(A). Different concentration of Hydrogen gas was added to the headspace and the magnetic response, C_{Mag} was measured over growth. See methods section for how C_{Mag} was calculated. (B). Growth curve of WT RS-1 grown with Nitrogen (blue) or Hydrogen (orange) in the headspace. Inlet graph shows the doubling time for both conditions. (C). RS-1 grown spinning on a wheel with either Nitrogen (blue) or Hydrogen (orange) and C_{Mag} values were measured showing no magnetic response for cultures grown with Hydrogen in the headspace. (D). Shows TEM images of cultures from (C). (E). Cells were grown with Hydrogen and (F). Abundance of magnetosome proteins in both nitrogen and hydrogen conditions. Blue bars represent proteins more abundant in nitrogen condition and orange bars represent proteins more abundant in hydrogen condition. (G). Growth curve (blue line) of a culture coming out of hydrogen condition and growing with Nitrogen to initiate biomineralization. C_{Mag} curve (orange line) of the same culture to show that biomineralization is initiated and increasing throughout growth.

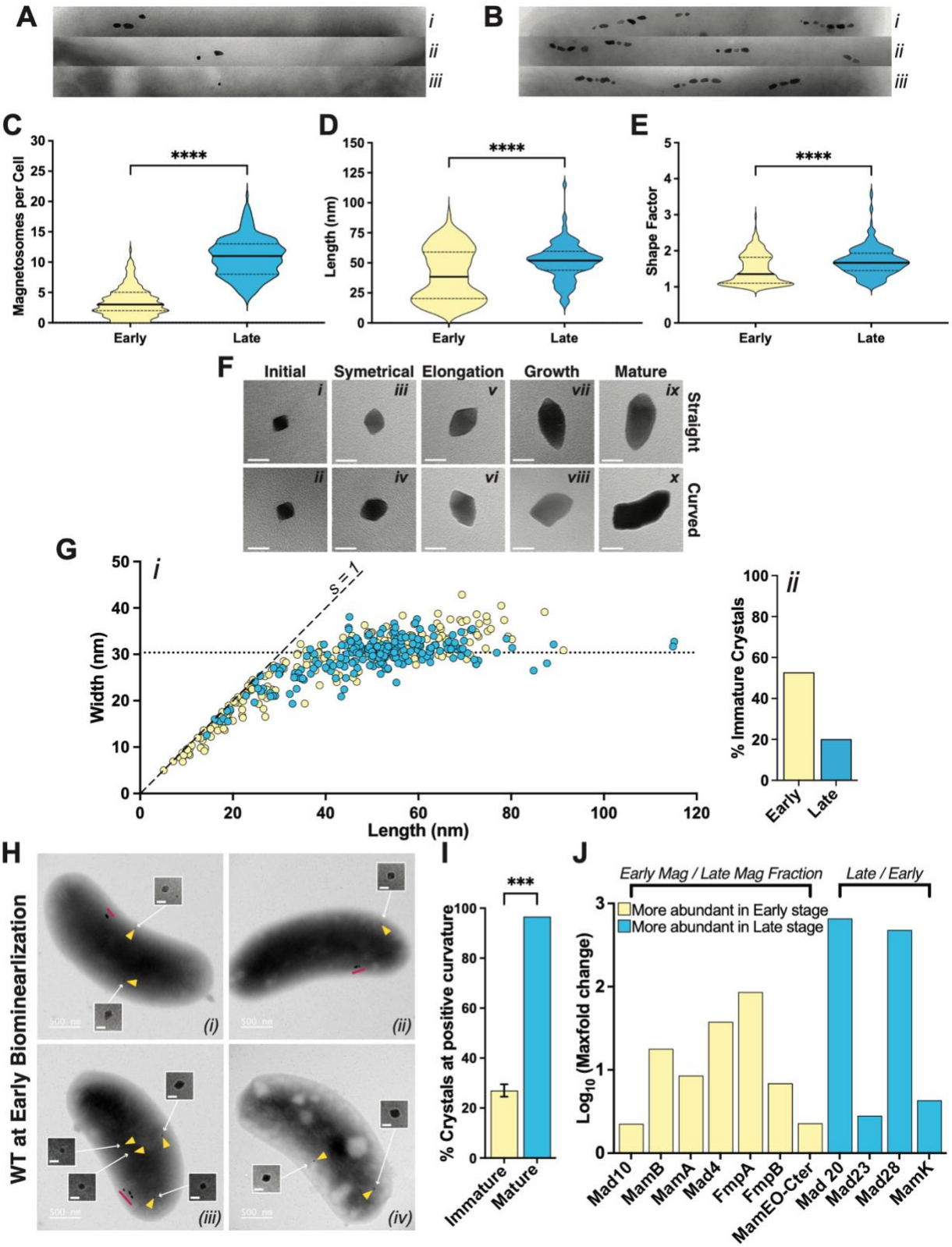
A
i
ii
iii
B
i
ii
iii
C
Magnetosomes per Cell
****
Early
Late
D
Length (nm)
****
Early
Late
E
Shape Factor
****
Early
Late
F
Initial
Symetrical
Elongation
Growth
Mature
i
iii
v
vii
ix
Straight
ii
iv
vi
viii
x
Curved
G
i
S=1
Width (nm)
Length (nm)
ii
% Immature Crystals
Early
Late
H
WT at Early Biominearlization
(i)
(ii)
(iii)
(iv)
I
***
% Crystals at positive curvature
Immature
Mature
J
Early Mag / Late Mag Fraction
Late / Early
More abundant in Early stage
More abundant in Late stage
Log10 (Maxfold change)
Mad10
MamB
MamA
Mad4
FmpA
FmpB
MamEO-Cter
Mad 20
Mad23
Mad28
MamK

Figure 3. *Proteomic analysis of magnetosome proteins at different stages of biomineralization* (A-B). TEM images of chain representing early stage and late stage of biomineralization. (C). Number of magnetosomes per cell for cells in early stages and lates stages of biomineralization. (D-E). Magnetosome measurements for crystals found in early stages vs. late stages of biomineralization, n=212 for early stages and n=214 for late stages. (F). TEM images of RS-1 magnetosomes at different stages of growth. All scale bars are 25 nm. (G). Each point is one crystal from WT (AK80) showing the measurement of the length and width for each crystal. Yellow dots represent crystals measured from cells at early stages of biomineralization. Blue dots represent crystals measured from cells at late stages of biomineralization. The dotted line represents the median width of crystals from late stages of biomineralization. Dashed line shows a slope of 1. (H). TEM images of early stage biomineralization of WT cells. Yellow triangles are pointing to immature crystals and the zoomed in images of those crystals are included for each. The white scale bars for the zoomed in crystals are all 25 nm. (I). Immature and mature magnetosomes were counted at early stage biomineralization. This graph shows the proportion of magnetosomes localized at the positive curvature of the cell for both immature and mature crystal, 140 cells counted; n=254 immature crystals, and n=394 mature crystals. (J). Magnetosome proteins more abundant at crystal fraction at different stages of biomineralization.

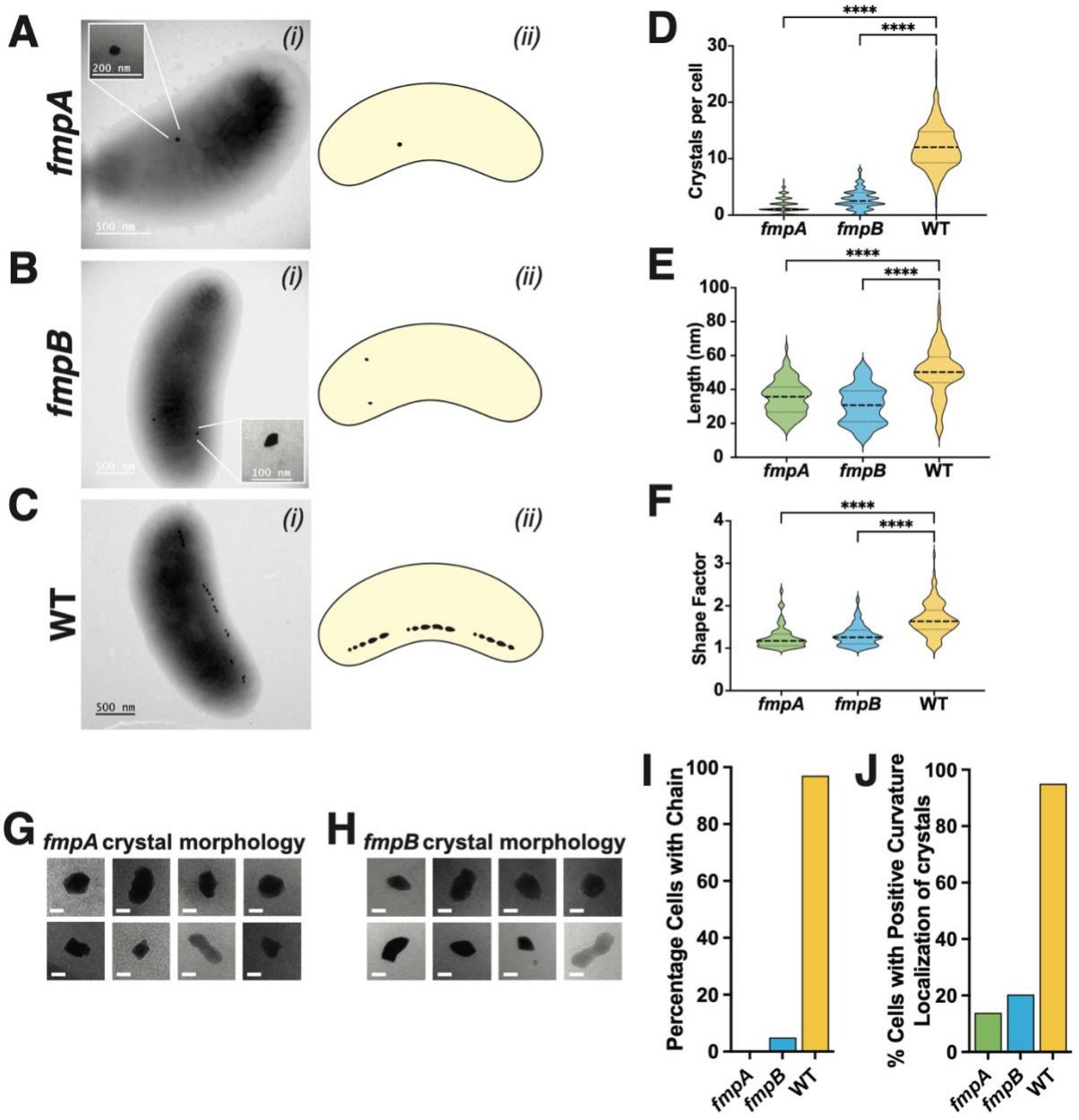

Figure 4. *Characterization of fmpA and fmpB mutants*

(A-C). (i). TEM images of each strain, and (ii) is the diagram of each strain. (D). Number of crystals per cell counted for each strain. (E-F) Crystal measurements n=200 for each strain. (E) are the measurements of crystal length for each strain and (F) are the calculated shape factor (length/width) of each crystal for each strain. (G-H). Crystal morphology for each mutant, scale bars are 25 nm. (I). Percent of cells with a chain phenotype, with more than one crystal in a line, for each strain. (J). Percent of cells with crystals located at the positive curvature in the cell. (I-J). Over 200 cells were counted.

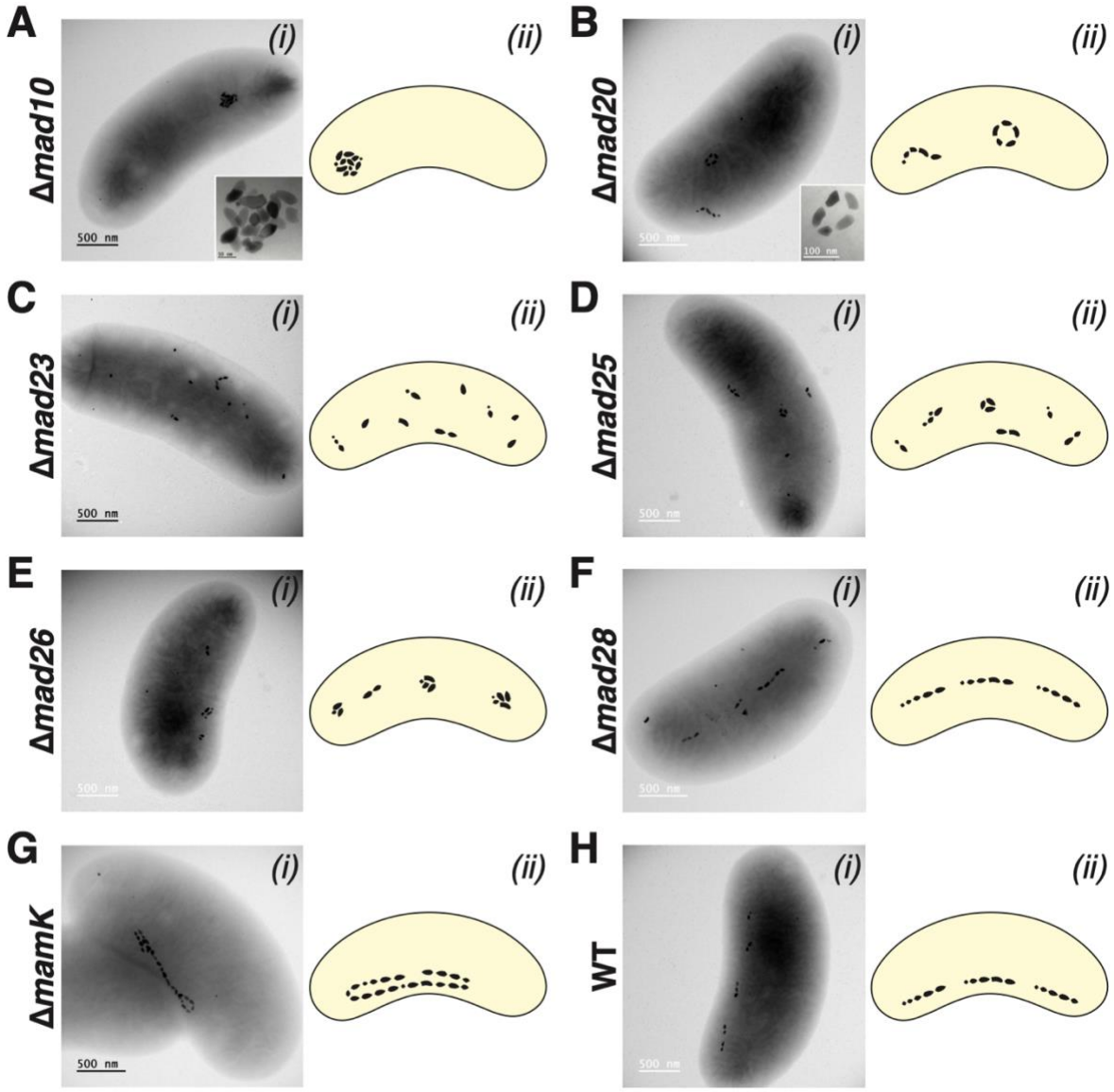

Figure 5. *Magnetosome gene deletions in RS-1*

(A-G) TEM images of different magnetosome gene deletion mutants in RS-1. (H). TEM image of wild type RS-1. (i) is the TEM representation of the strain and (ii) shows a diagram of the strain.

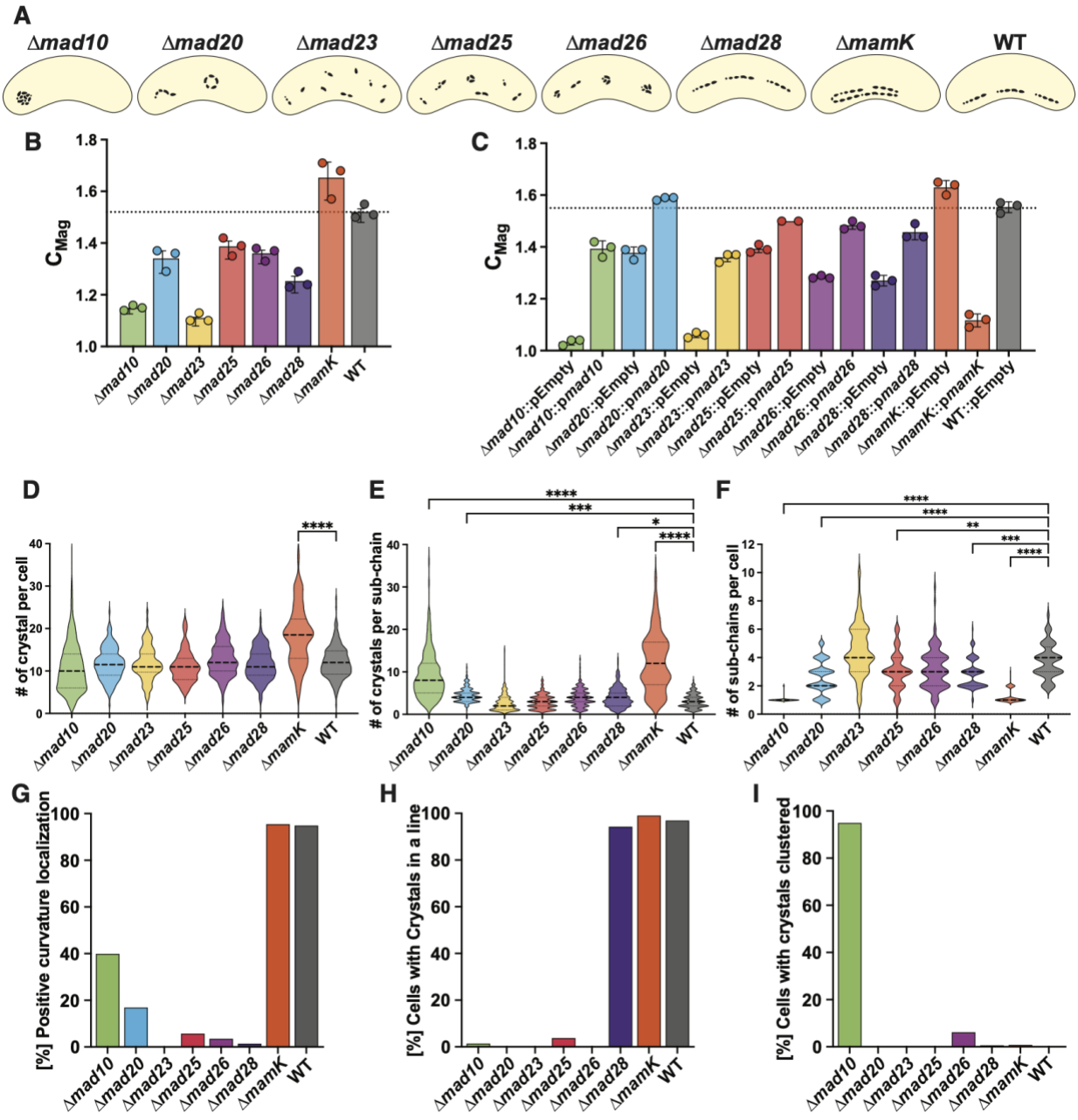

Figure 6. *Characterization of Magnetosome gene deletions in RS-1*

(A). Diagram of each strain. (B). C_{Mag} values for each strain. Cells grown in triplicates. No plasmids in the cells. (C). C_{Mag} values for each mutant with an empty plasmid and for each mutant with their complementation plasmid. WT has an empty plasmid. (D). Number of crystal per cell for each strain. (E). Number of crystals for each sub-chain for each strain. (F). Number of sub-chains per cell for each strain. (G-I). Shows the percentage of cells with a particular phenotype. 200 cells were counted for each strain. (G) shows the percent of cells with crystals localized at the positive curvature, (H) shows the percent of cells with a chain phenotype and (I) shows the percent of cells with crystals all clustered together.

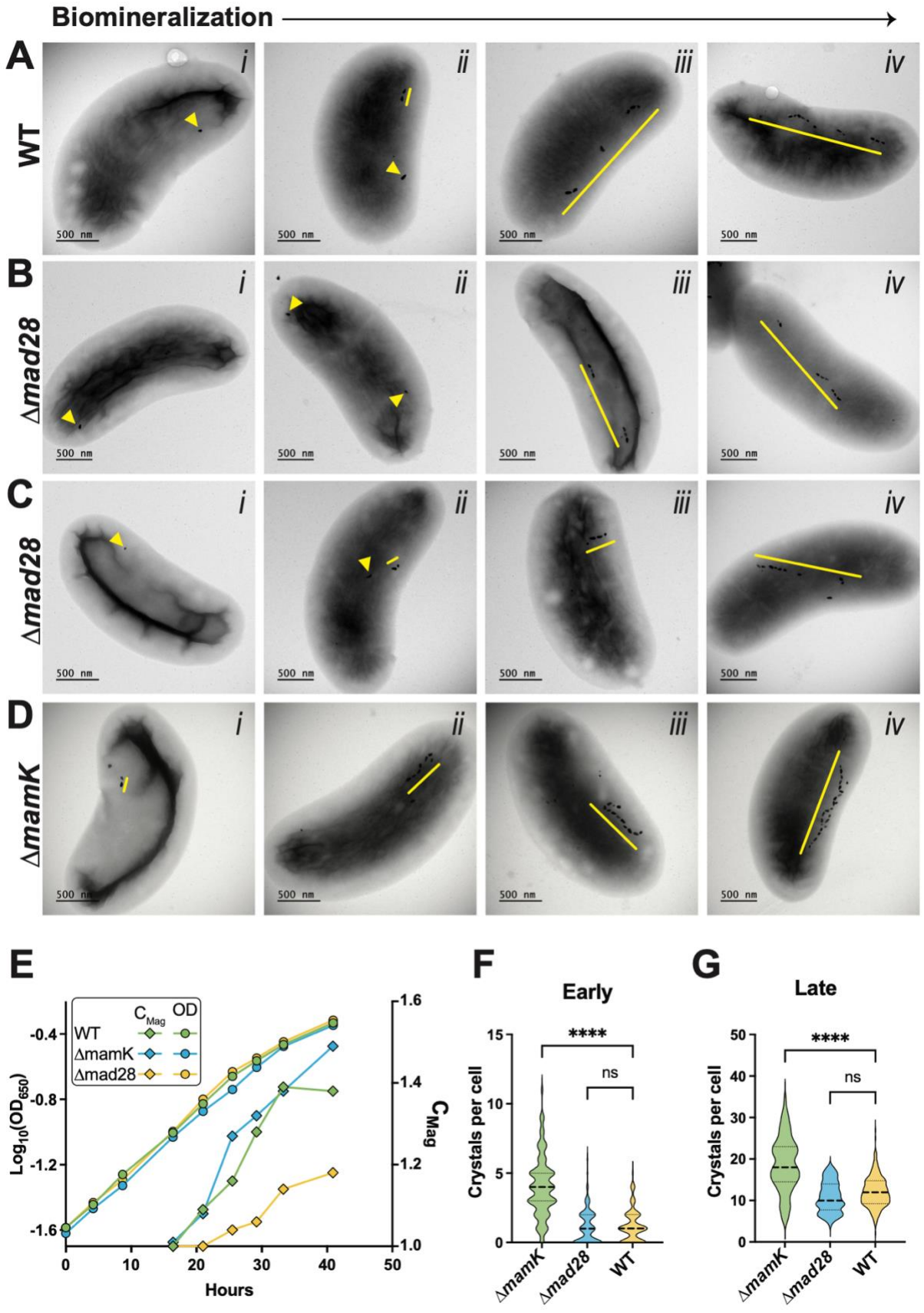
Biomineralization
A
WT
B
ΔmadΔ28
C
ΔmadΔ28
D
ΔmamK
i
ii
iii
iv
500 nm
E
C_Mag
OD
WT
ΔmamK
Δmad28
Log10(OD650)
CMag
Hours
F
Early
Crystals per cell
****
ns
ΔmamK
Δmad28
WT
G
Late
Crystals per cell
****
ns
ΔmamK
Δmad28
WT

Figure 7. *Biomineralization time course of Δmad28, ΔmamK and WT*

(A). Biomineralization time course of wildtype. (B-C). Biomineralization time course of Δ*mad28*. (B) shows the phenotype for Δ*mad28* where the chain localizes to the mid-cell, whereas (C) shows the phenotype for Δ*mad28* where the chain localizes diagonally or transversally. (D). Biomineralization time course for Δ*mamK*, show no sub-chains forming. (E). Growth curve and C_{Mag} curve for WT, Δ*mad28* and Δ*mamK*. (F). Number of crystals per cell for WT, Δ*mad28* and Δ*mamK* at early stages of biomineralization, over 100 cells counted for each strain. (G). Number of crystals per cell for WT, Δ*mad28* and Δ*mamK* at late stages of biomineralization, over 100 cells counted for each strain.

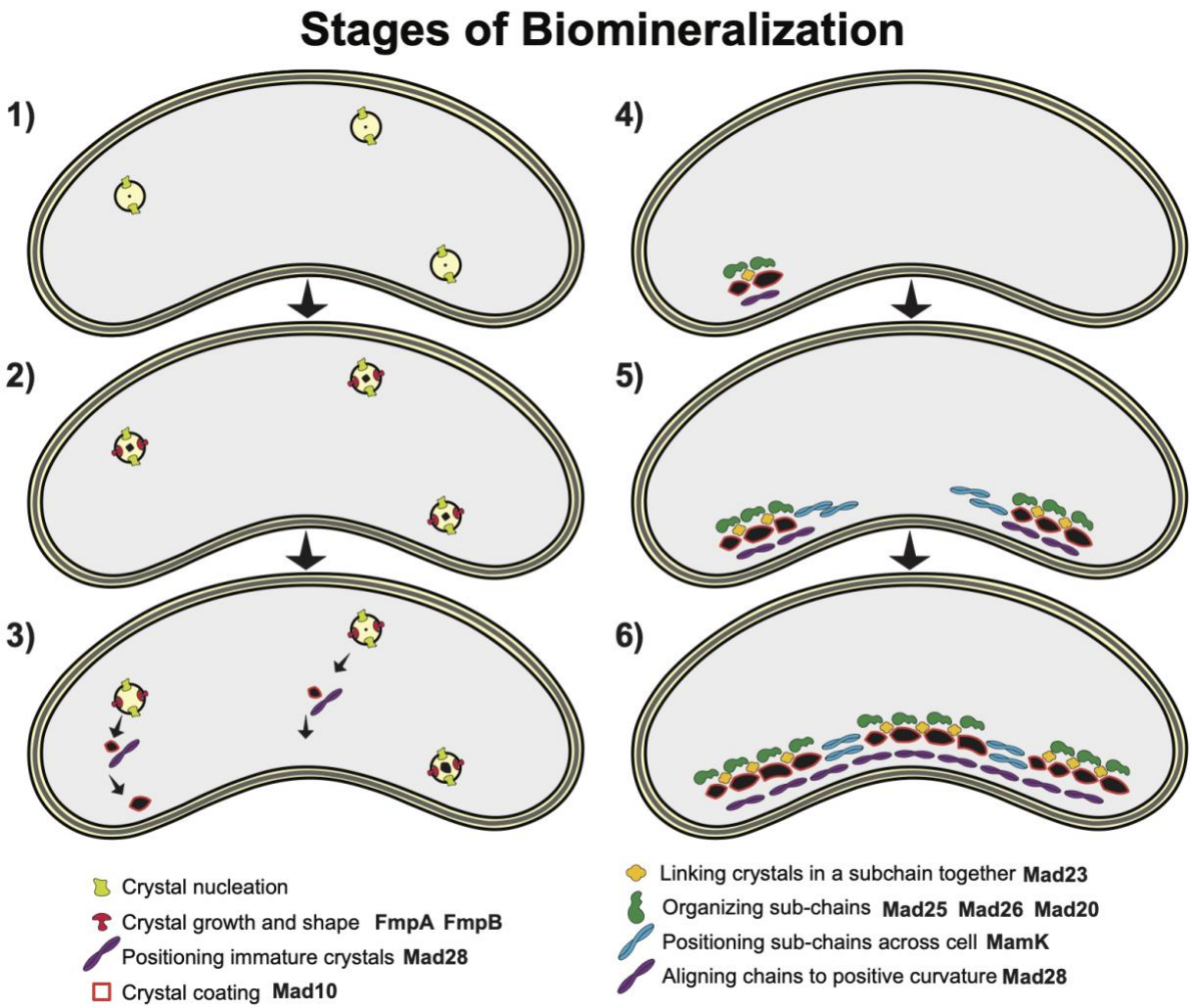

Figure 8. *Model of Magnetosome synthesis and chain organization in RS-1*

Model of different stages of biomineralization. Early stages of biomineralization includes: stage 1, where crystal nucleation occurs, stage 2, crystal growth and shape control occurs, and stage 3, whereby immature crystals at a certain stage are positioned to the positive curvature of the cell. This proposed model shows at the early stages the 'magnetosome factory' is actually distributed throughout the cell, then at a certain growth stage crystals are repositioned to the positive curvature of cell. Late stages of biomineralization involves chain organization. Stage 4 is where small sub-chains start to form, then in stage 5 more crystals are being added to the different sub-chains, and finally in step 6 the sub-chains are complete and in line with each other.

Supplemental Figures

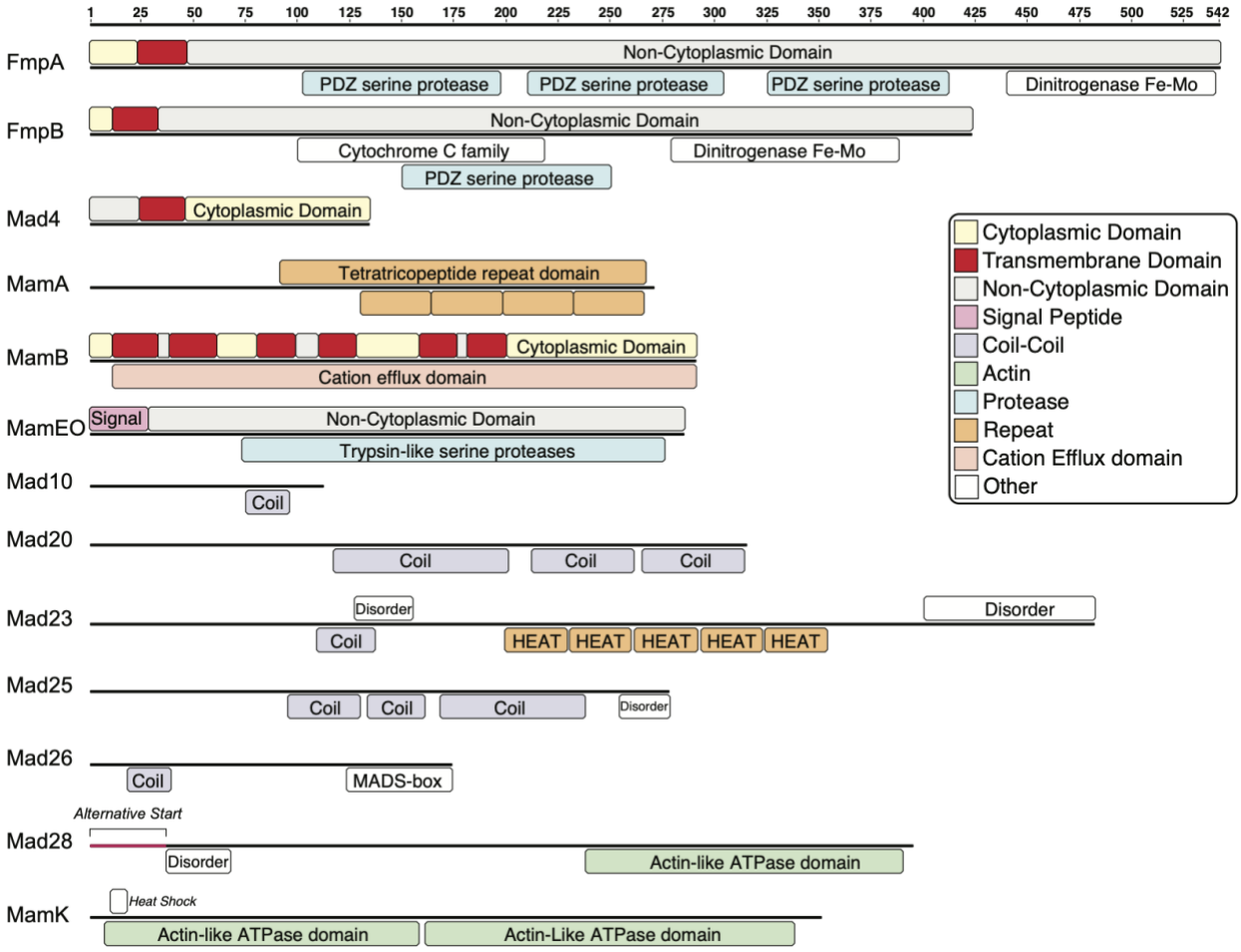

Supplemental S1. *Protein domain of proteins from proteomics and deletions.*

Protein domains were identified using InterPro (*52*) and uploaded on to Geneious (*53*) to generate domain maps. Red Asterix represent proteins that were not part of the proteomic analysis in Figure 3J. Mad25 was present in raw data from proteomics, but it was more abundant in cell lysate in comparison to at magnetosome fraction. Mad26 was not present in proteomics data. Mad28 shows an alternative start site that was not included in the original NCBI annotation and Δ*mad28* could only be complemented when including the alternative start site.

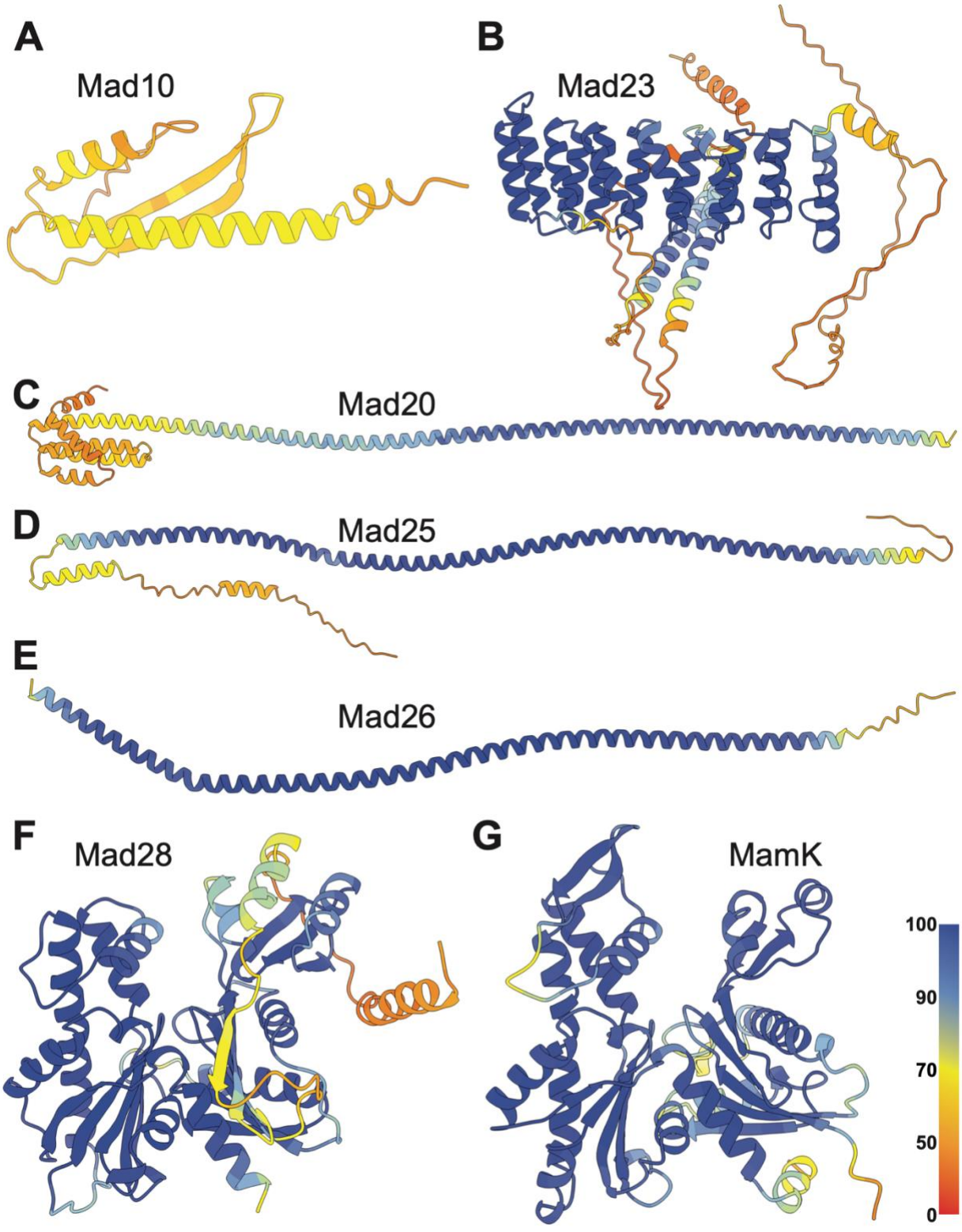
A
Mad10
B
Mad23
C
Mad20
D
Mad25
E
Mad26
F
Mad28
G
MamK
100
90
70
50
0

Supplemental S2. *Predicted crystal Structures of Mad proteins deleted in RS-1*

Predicted protein structures of Mad proteins in this study made with Alphafold2 using ColabFold (*54*) and visualized with ChimeraX (*55*). 3D structures are colored according to Alphafold2 confidence values, with blue at 100% confident and red 0% confidence.

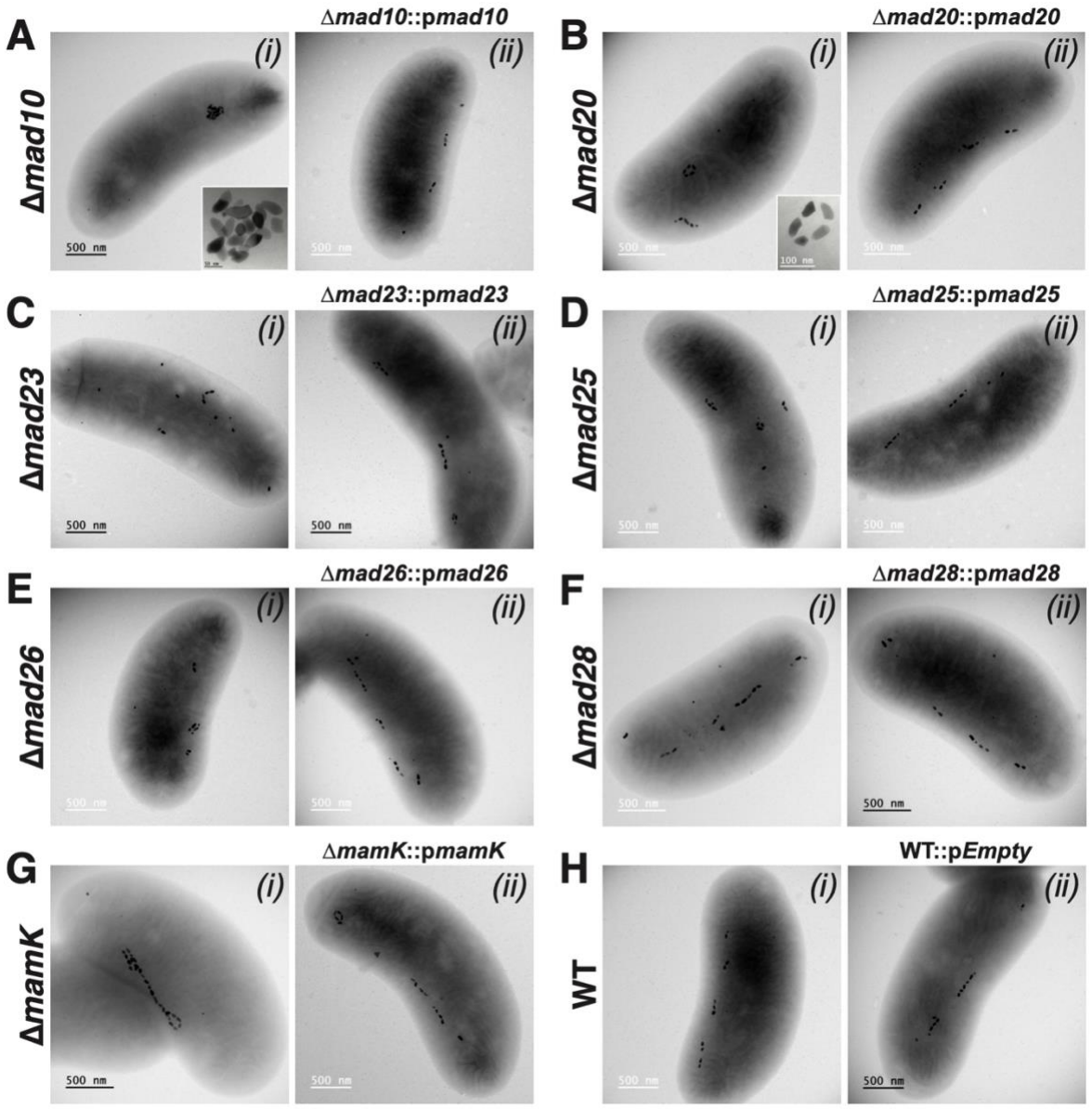

Supplemental S3. *TEM images of Complementation of deletion mutants*

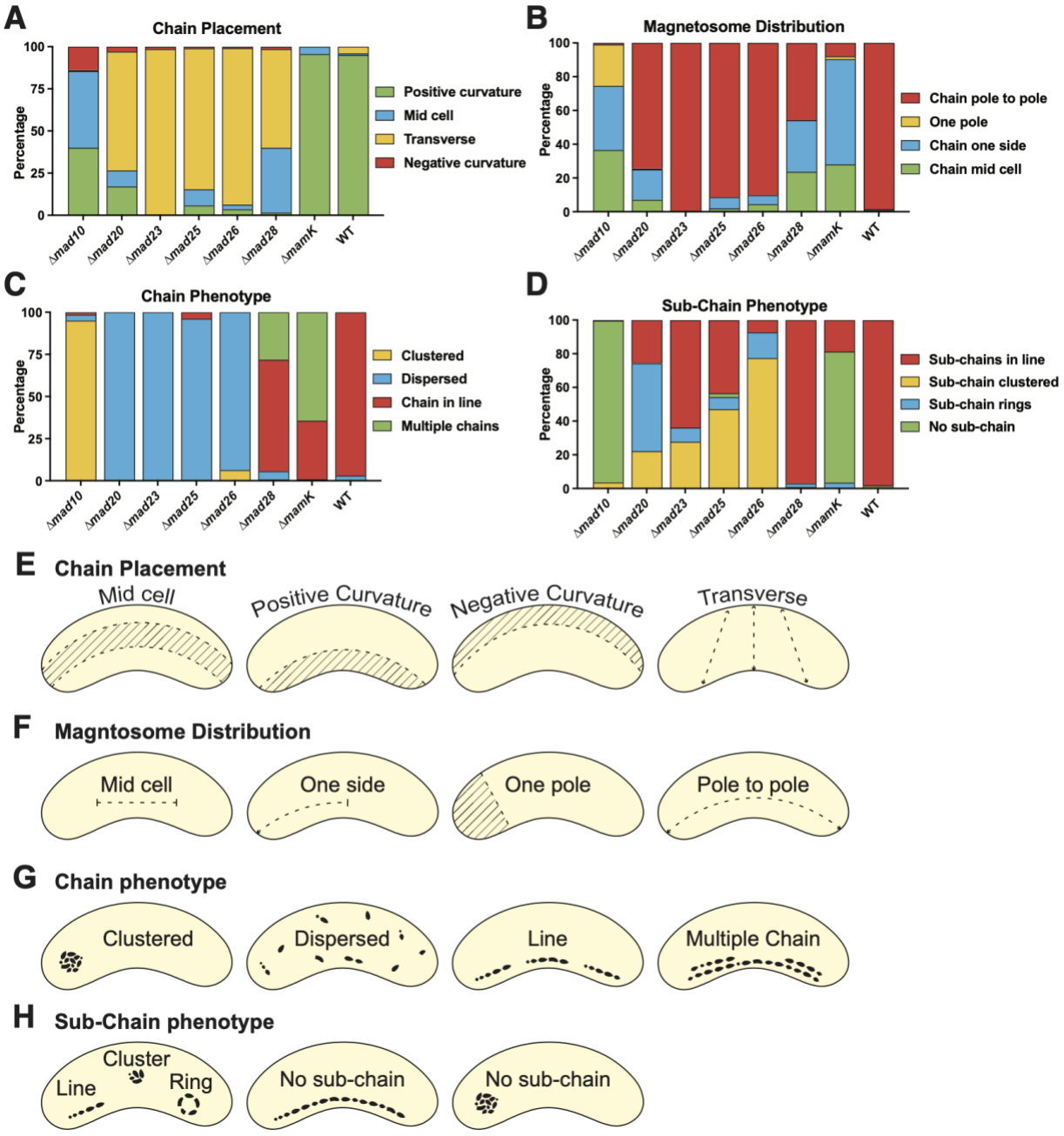

Supplemental S4. *Additional mutant phenotypes and magnetosome chain and sub-chain categories*

(A-D) Additional phenotype categories for all mutants. (E-H) Categories used to calculate mutant phenotypes in Figure 4, Figure 5 and in Supplemental Figure S5, as well as (A-D) in this figure.

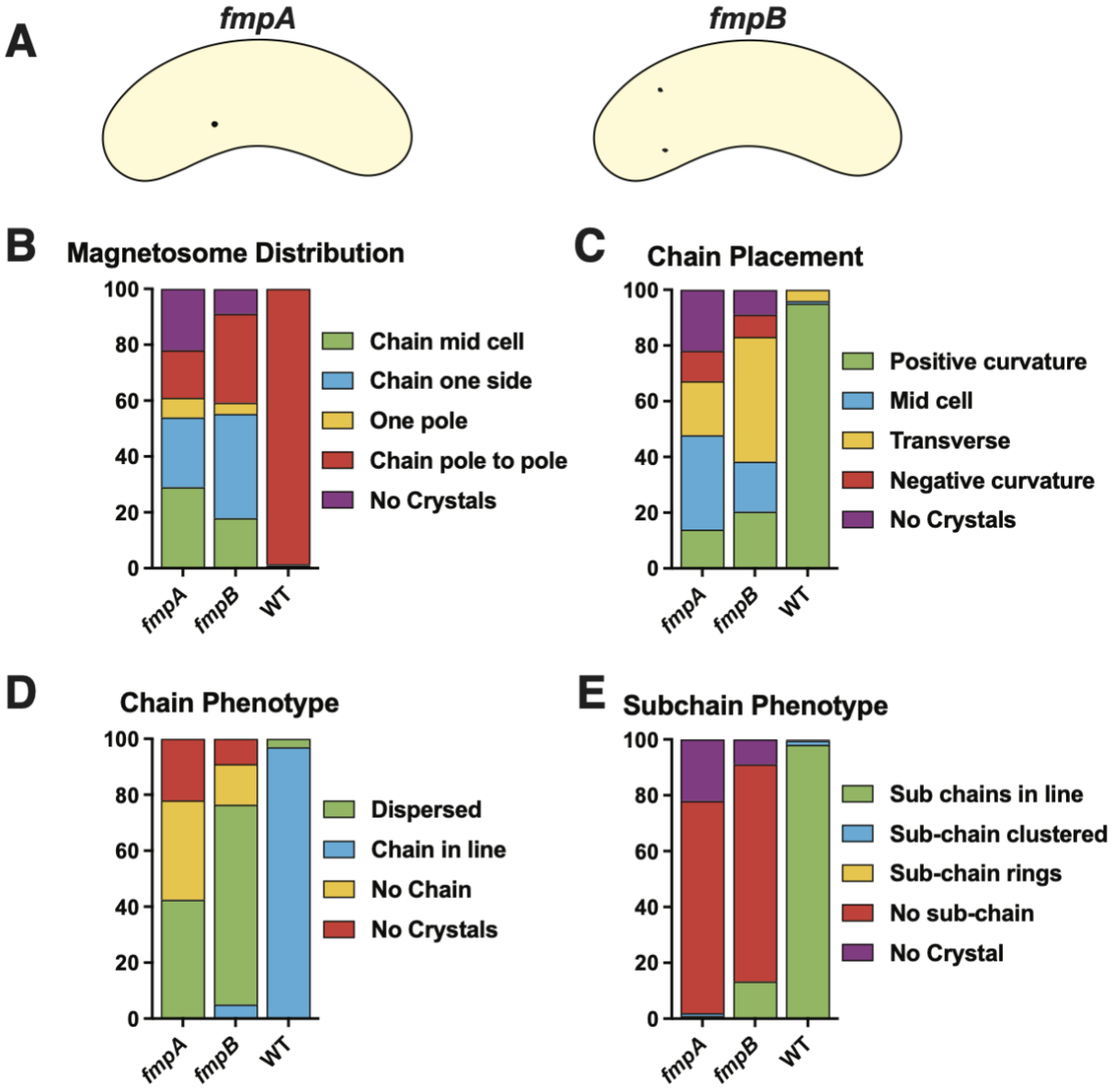

Supplemental S5. *Additional fmpA and fmpB mutant phenotypes*
Additional phenotypes for *fmpA* and *fmpB* mutants

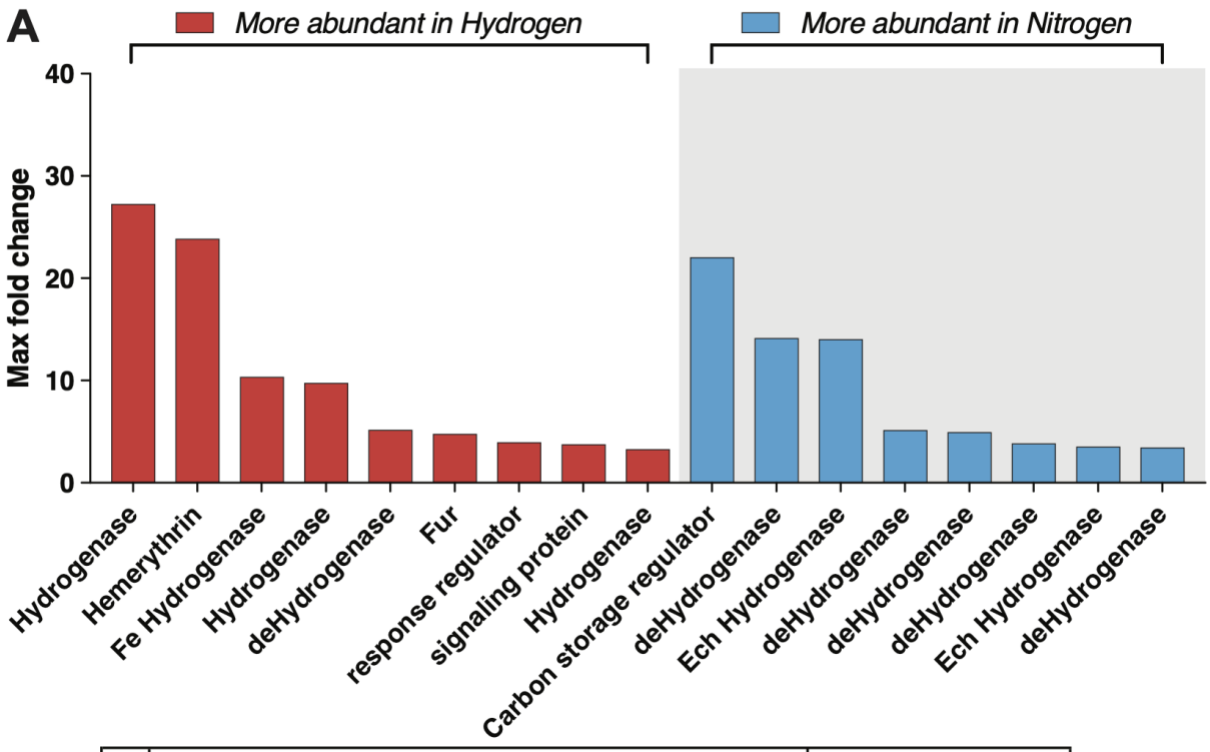

B

	Protein name	Highest abundance
1	DMR_07840: NAD-reducing Hydrogenase	Hydrogen
2	DMR_07060 hemerythrin family protein	Hydrogen
3	DMR_07830: Fe Hydrogenase	Hydrogen
4	DMR_07850: NAD-reducing Hydrogenase	Hydrogen
5	DMR_27790: NADH deHydrogenase	Hydrogen
6	Fur ferric uptake regulation	Hydrogen
7	DMR_12790: response regulator receiver	Hydrogen
8	DMR_09360: putative signaling protein	Hydrogen
9	DMR_01930 methyl-viologen-reducing Hydrogenase	Hydrogen
10	CsrA carbon storage regulator	Nitrogen
11	DMR_27790: NADH deHydrogenase	Nitrogen
12	DMR_02750: Ech Hydrogenase EchC	Nitrogen
13	DMR_01890: deHydrogenase	Nitrogen
14	XdhA xanthine deHydrogenase	Nitrogen
15	aspartate-semialdehyde deHydrogenase	Nitrogen
16	DMR_02740: Ech Hydrogenase EchB	Nitrogen
17	FwdE formylmethanofuran deHydrogenase	Nitrogen

Supplemental S6. *Proteomics of Nitrogen vs. Hydrogen non-magnetosome proteins*

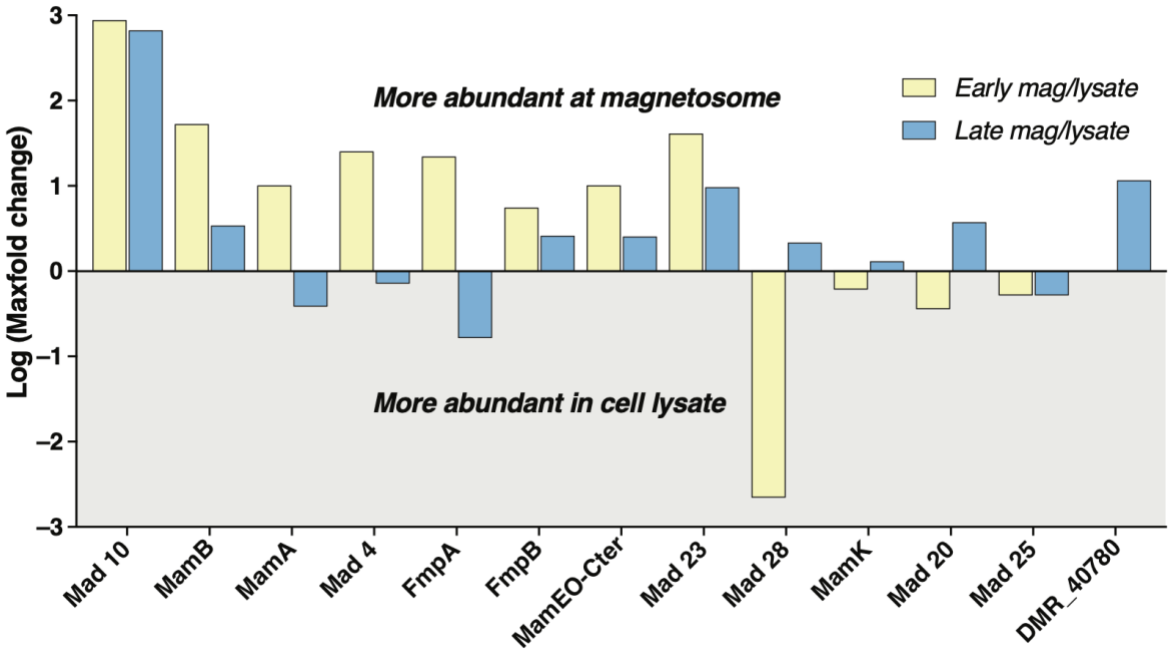

Supplemental S7. *Additional proteomics data of magnetosome proteins in lysate vs. magnetosomes*

A

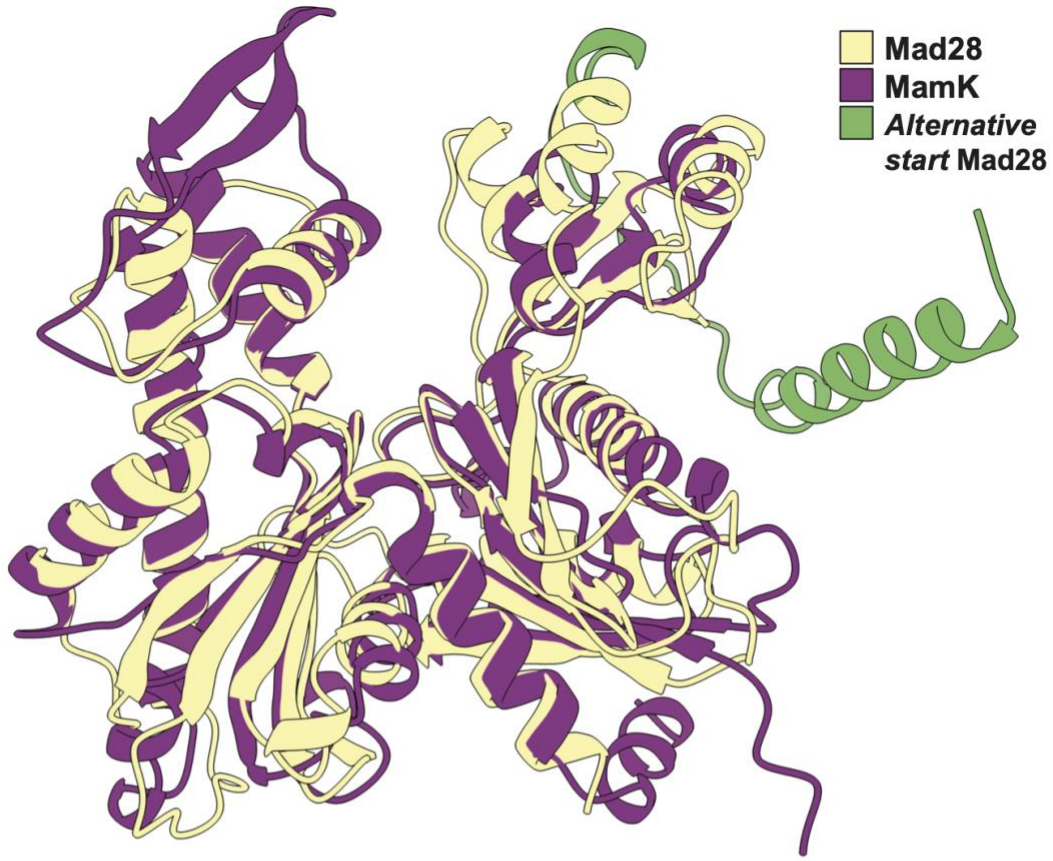

B

```
                1                  10                  20                  30                  40
Mad28  MSQEDKANIFEQKERLDAARNTLDGDVAWGGSLPEDASMERAA
MamK   MSGSNVLN----------------------------------

                    50                  60                  70                  80
Mad28  AASQKPAIGHQSEGGPDGAERPSGPVGLDIGTSH-IVSAQNRL
MamK   ----------------------------IGIDLGTSRSVIACDNGV

                90                  100                 110                 120
Mad28  RHLHMANQLNAFFTVPVSKFSRKILQSHDIIFFELGNLFYIIG
MamK   RTF-----ISSIVGYPKDAISKKLL-GKDVVFGE----------

               130                 140                 150                 160                 170
Mad28  YSADSFANMFNTSTRRPIQAGLLSPSEKEGVKVVQALVSTLIQ
MamK   ---EAAKNRLALEMRRPFEKGMLKFSN------LQDLSSAEFE

                    180                 190                 200                 210
Mad28  KPKRFGETICFGIPGEPVETPTPGAVTYHEQVLKMFLQSL--G
MamK   RYKGVARDLLHHLVGL-VRKESPQAQVVRAVIGAPALASTQNK

                220                 230                 240                 250
Mad28  YSPVSINEGMATVLSELGEDDYTGFG---------VSMGGGMI
MamK   KTLIEITKGILDDVMITSEPFAVAYGLGILNNALIVDIGAGTV

               260                 270                 280                 290                 300
Mad28  NVCLSYLSFPVVT--FSLQMAGDYIDTM-------AGISVGEP
MamK   DLCRMSGVIPTEADQITLTKAGDHIDEVLLDLIKTQHAEVDVT

                        310                 320                 330                 340
Mad28  ATKIKGIKEEELDLSRDPKGQ----------------IHTALH
MamK   LNMVKRVKEENATISE--KGERVMALLPIKGKPTSVDVTDALH

                    350                 360                 370                 380
Mad28  IYYDEVIHKLLGALQRVLTASDKLPKIAKPVPIVLSGGTAMPR
MamK   EACRSIIPDIVGGIRSLVASFDPEFQDSLKQNVVLAGGGSQIG

               390                 400                 410                 420                 430
Mad28  GCHDRFAKALERF-NLPISISGVRLAEDPLYATAKGALLMALT
MamK   G----MARLIEAYMQEHLGYGKVSRVEEPLYAGANGGLLLCKD

                        440 442
Mad28  ---------EAD
MamK   MPSDYWDELRKD
```

Supplemental S8. *Alignments of MamK and Mad28 in Desulfovibrio magneticus RS-1*

(A). 3D alignment of protein structures of Mad28 and MamK from RS-1. Protein structures were made with alphafold2 using ColabFold (*54*) and then a 3D alignment was preformed using ChimeraX (*55*). Purple is the 3D predicted structure for MamK, yellow is the predicted structure for Mad28 and green is the structure that includes the alternative start site for Mad28. Δ*mad28* would only complement with this sequence included in the plasmid. (B) 2D protein sequence alignment of MamK and Mad28 using MAFFT v7.490 plug-in on Geneious (*53*). Blue highlighted residues show similarities between sequences and red dashes represent gaps. Green letters show the sequence for the alternative start in Mad28.

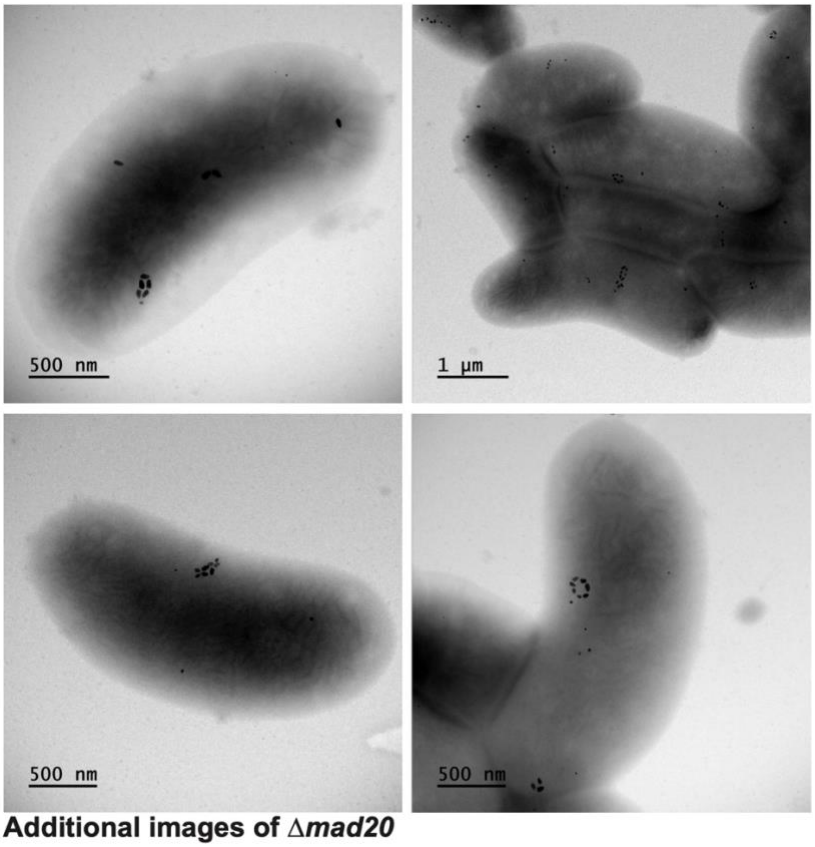

Supplemental S9. *Additional TEM images of Δmad20 in RS-1*

These images are to illustrate the fewer sub-chains in each cell and more crystals per sub-chain in each cell to complement the statistical data from Figure 6. Perhaps rings form in this mutant because sub-chains are too long, similar to Δ*mamK* phenotype.

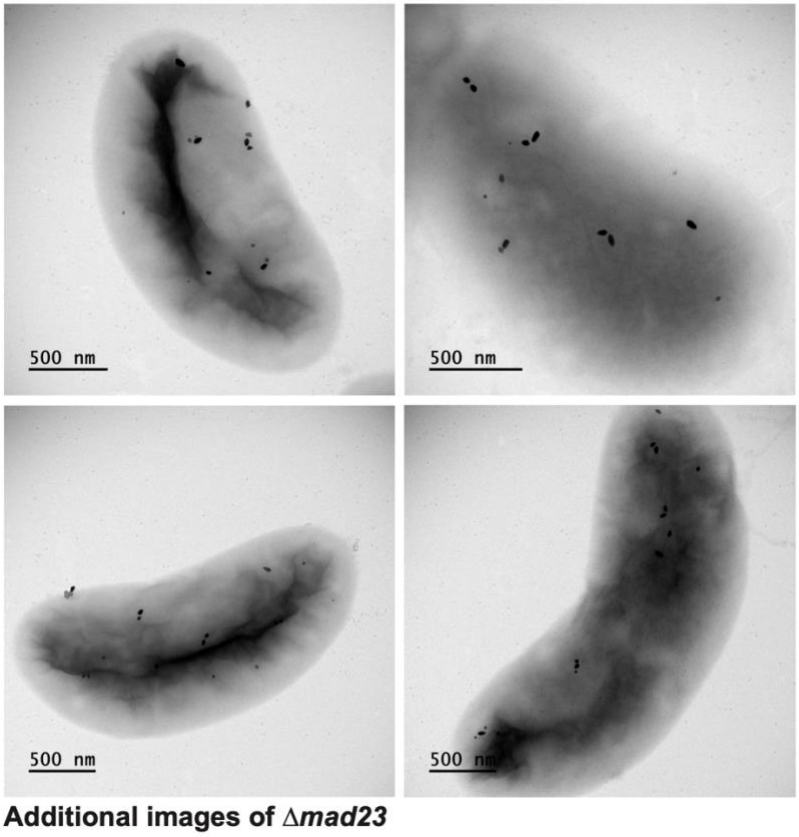

Supplemental S10. *Additional TEM images of Δmad23 in RS-1*

These images are to illustrate the more sub-chains in each cell and less crystals per sub-chain in each cell to complement the statistical data from figure 6. Sub-chains look more broken up in Δ*mad23*.

Supplemental Tables

Phyla	Organiam	16S gene ID	Genome ID	Shape reference	MGC reference
Alpha	*Magnetospirillum magneticum* AMB-1	D17514.1	NCBI:txid342108	(*56*)	(*57*)
Alpha	*Magnetospirillum magnetotacticum* MS-1	IMG: 2647169949	NCBI:txid272627	(*58*)	(*59*)
Alpha	*Magnetospirillum caucaseum* SO-1	JX502622.2	NCBI:txid1244869	(*60*)	(*8*, *60*, *61*)
Alpha	*Magnetospirillum* ME-1	IMG: 2676550241	NCBI:txid1639348	(*62*)	(*8*, *61*, *63*)
Alpha	*Magnetospirillum* XM-1	KP966105.1	NCBI:txid1663591	(*64*)	(*8*, *65*)
Alpha	*Magnetospirillum marisnigri* SP-1	KC252630.3	NCBI:txid1285242	(*60*)	(*61*, *66*)
Alpha	*Magnetospirillum kuznetsovii* LBB-42	NR_180134.1	NCBI:txid2053833	(*67*)	(*8*, *67*)
Alpha	*Magnetospirillum gryphiswaldense* MSR-1	NR_121771.1	NCBI:txid431944	(*68*, *69*)	(*70*)
Alpha	*Magnetospirillum moscoviense* BB-1	KF712468.2	NCBI:txid1437059	(*60*)	(*61*, *66*)
Alpha	*Magnetospirillum* sp. LM-5	IMG: 2894467686	NCBI:txid2681466	(*71*)	(*61*)
Alpha	*Magnetospirillum* sp. SS-4	IMG: 2894461381	NCBI:txid2681465	(*71*)	(*61*)
Alpha	*Magnetospirillum* sp. UT-4	IMG: 2894472958	NCBI:txid2681467	(*71*)	(*61*)
Alpha	*Rhodospirillaceae* LM-1	JF490044.1	NCBI:txid1008128	(*71*)	(*61*)
Alpha	*Magnetospira* QH-2	EU675666.1	NCBI:txid1288970	(*72*)	(*73*)
Alpha	*Ca. Terasakiella magnetica* PR1	IMG: 2752957094	NCBI:txid1867952	(*74*)	(*74*)
Alpha	*Magnetovibrio blakemorei* MV-1	L06455.1	NCBI:txid28181	(*75*)	(*76*)
Gamma	Strain BW-2	HQ595728.1	NCBI:txid947515	(*77*)	(*78*)
Gamma	SHHR-1	KX344069.1	NCBI:txid1899433	(*79*)	(*8*)
Gamma	Strain SS-5	HQ595729.1	NCBI:txid947516	(*77*)	(*80*)
Eta	*Ca. Magnetococcus massalia* MO-1	EF643520.2	NCBI:txid451514	(*81*)	(*82*)

Eta	*Magnetococcus* MC-1	IMG: 640720050	NCBI:txid156889	(*83*)	(*84*)
Eta	*Magnetofaba australis* IT-1	JX534168.1	NCBI:txid1434232	(*85*)	(*85*)
Eta	*Ca. Magnetaquicoccus inordinatus* UR-1	IMG: 2881921666	NCBI:txid2496818	(*86*)	(*86*)
Delta	*Ca. Magnetoglobus multicellularis*	IMG: 2559591426	NCBI:txid890399	(*87*, *88*)	(*89*)
Delta	*Ca. Magnetananas rongchenensis* RPA	KF925363.1	NCBI:txid1463558	(*90*)	(*90*)
Delta	*Ca. Magnetomorum* HK-1	IMG: 2648890082	NCBI:txid1509431	(*91*)	(*92*)
Delta	*Desulfamplus magnetovallimortis* BW-1	JN252194.1	NCBI:txid1073250	(*22*)	(*23*)
Delta	*Desulfovibrio magneticus* RS-1	NR_074958.1	NCBI:txid573370	(*16*, *17*)	(*93*)
Delta	*Desulfovibrio* FSS-1	LC311577.1	NCBI:txid2730080	(*29*)	(*29*)
Delta	*Delta Proteobacterium* FH-1	JF330268	NCBI:txid999117	(*23*)	(*23*)
Delta	*Desulfonatronum* ML-1	HQ595725.1	NCBI:txid947513	(*94*)	(*23*)
Nitro-spirae	*Ca. Magnetoovum chiemensis* WYHC-5	OL423397.1	NCBI:txid1609970	(*95*)	(*95*)
Nitro-spirae	*Ca. Magnetobacterium casensis* MYR-1	MT703955.1	NCBI:txid1455061	(*34*)	(*96*)
Nitro-spirae	*Ca. Magnetobacterium bavaricum* TM-1	X71838.1	NCBI:txid29290	(*21*)	(*97*)
Nitro-spirae	*Ca. Nitrospirae* YQR-1	ON340538.1		(*8*)	(*8*)
Nitro-spirae	*Ca. Magnetomonas plexicatena* LBB-01	MK632185.1	CP049016.1	(*98*)	(*98*)
Nitro-spirae	*Ca. Magnetominusculus linsii* LBB-02	MK632186.1		(*98*)	(*98*)
Nitro-spirae	*Ca. Nitrospirae* MYC-10	ON342894.1		(*8*)	(*8*)
Nitro-spirae	*Ca. Magnetocorallium paracelense* XS-1	OQ281288.1	NCBI:txid3021403	(*99*)	(*99*)
OP3	*Ca. Omnitrophus magneticus* SKK-01	JN412733.1	NCBI:txid174292	(*100*)	(*97*)

Supplemental Table 1. *Table of species and reference used for phylogenetic tree construction*

Strain	Description	Reference
AK80	WT	(*25*)
AK268	WT, Δ*upp*	(*26*)
AK350	Δ*mad23*, Δ*upp*	This study
AK377	Δ*mad20*, Δ*upp*	This study
AK378	Δ*mad25*, Δ*upp*	This study
AK380	Δ*mad10*, Δ*upp*	This study
AK382	Δ*mad28*, Δ*upp*	This study
AK383	Δ*mad26*, Δ*upp*	This study
AK220	Δ*mamK*	This study

Supplemental Table 2. *Table of all strains used in this study*

Plasmid	Description	Backbone	Reference
PAK906	Complementation backbone with P*npt*		(*25*)
PAK907	Complementation backbone with P*mamA*		(*25*)
pAK914	Deletion backbone with SacB only		(*25*)
pAK1127	Deletion backbone with Upp and SacB		(*26*)
pAK1452	pVR071: *mad10* deletion plasmid with Strep	pAK1127	This study
pAK1384	pVR022: *mad20* deletion plasmid with *strAB*	pAK1127	This study
pAK1268	*mad23* deletion with *strAB* for selection and *upp* counterselection (pCG116)	pAK1127	This study
pAK1386	pVR026: *mad25* deletion plasmid with *strAB*	pAK1127	This study
pAK1387	pVR028: *mad26* deletion plasmid with *strAB*	pAK1127	This study
pAK1388	pVR031: *mad28* deletion plasmid with *strAB*	pAK1127	This study
pAK966	*mamK* deletion plasmid with *strAB* in pAK914	pAK914	This study
pAK1481	pVR077: pAK906– *mad10* complementation	pAK906	This study
pAK1454	pVR073: pAK906– *mad20* complementation	pAK906	This study
pAK1507	pVR008: p906– *mad23* complementation	pAK906	This study
pAK1480	pVR076: pAK907– *mad25* complementation	pAK907	This study
pAK1488	pVR084: pAK907– *mad26* complementation	pAK907	This study
pAK1518	pVR096: pAK907– *mad28* complementation (with alternative start site)	pAK907	This study
pAK1489	pVR085: pAK906– *mamK* complementation	pAK906	This study

Supplemental Table 3. *Table of all plasmids used in this study*

All of the plasmids used for this study and the previously published backbones used to generate the plasmids used for this research.

Primer	Sequence	Description
VR123-F	AAACGCAAAAGAAAATGCCGATATCC TATTGGCCTCTAGAGGAATTCCAGGAT TCCCTCA	*mad20* deletion upstream
VR124-R	GGATCCCCCATCCACTAAATTTAAATA GGATCCTCTGTCCTTAATCTTGGCC	*mad20* deletion upstream
VR125-F	GGATCCTATTTAAATTTAGTGGATGGG GGATCCAGGATCGCCAACAATGCCTG	*mad20* deletion downstream
VR126-R	TGGCGGTCATGGTCTTTTCGGCGAGCT TCTCTAGAAGCTCCGCTTCAAGAACCA C	*mad20* deletion downstream
VR127-F	AAACGCAAAAGAAAATGCCGATATCC TATTGGCCTCTAGACAAGTGGAGTTAG GGTGATT	*mad25* deletion upstream
VR128-R	CATATGCCCATCCACTAAATTTAAATA CATATGGTCAGCTTTAAAAAGGGCCA	*mad25* deletion upstream
VR129-F	CATATGTATTTAAATTTAGTGGATGGG CATATGTGTTCGGCCATTGCCGTTAT	*mad25* deletion downstream
VR130-R	TGGTGGCGGTCATGGTCTTTTCGGCGA GCTTCTCTAGACCTCGTCTCTCTAACA CAAA	*mad25* deletion downstream
VR131-F	AAACGCAAAAGAAAATGCCGATATCC TATTGGCCTCTAGACATCAAAAGCATG GAAGGGC	*mad26* deletion upstream
VR132-R	GGATCCCCCATCCACTAAATTTAAATA GGATCCTTCGCGCTGCATTCCGTCCA	*mad26* deletion upstream
VR133-F	GGATCCTATTTAAATTTAGTGGATGGG GGATCCACTATTGCCTTGAATAAATG	*mad26* deletion downstream
VR134-R	TGGTGGCGGTCATGGTCTTTTCGGCGA GCTTCTCTAGAGCATCCAAGCGTTCTT TTTG	*mad26* deletion downstream
VR135-F	AAACGCAAAAGAAAATGCCGATATCC TATTGGCCTCTAGAAACGGTTTACAGC GGATACA	*mad28* deletion upstream
VR136-R	GGATCCCCCATCCACTAAATTTAAATA GGATCCGCATCCAAGCGTTCTTTTTG	*mad28* deletion upstream
VR137-F	GGATCCTATTTAAATTTAGTGGATGGG GGATCCGGCCCTGACCGAGGCGGATT	*mad28* deletion downstream
VR138-R	TGGCGGTCATGGTCTTTTCGGCGAGCT TCTCTAGACAAAATGGAGATTGGAGG AA	*mad28* deletion downstream
VR147-F	AGGCGGGCATGGCCAAGATTAAGGAC AGAGGATCCCTGCTAAAGGAAGCGGA ACACG	Add *strAB-mad20*-F

VR148-R	ATTCGCTATCAGGCATTGTTGGCGATCCTGGATCCCTAGTATGACGTCTGTCGCACCT	Add *strAB-mad20*-R
VR149-F	AGGGGCCATGGCCCTTTTTAAAGCTGACCATATGCTGCTAAAGGAAGCGGAACACG	Add *strAB-mad25*-F
VR150-R	GAAAAAGCATAACGGCAATGGCCGAACACATATGCTAGTATGACGTCTGTCGCACCT	Add *strAB-mad25*-R
VR151-F	GGGCAAACACTCCCGGTCGATTCCGGACAGGATCCCTGCTAAAGGAAGCGGAACACG	Add *strAB-mad26*-F
VR152-R	ATCACAGTTCATTTATTCAAGGCAATAGTGGATCCCTAGTATGACGTCTGTCGCACCT	Add *strAB-mad26*-R
VR153-F	ATATTCGAGCAAAAAGAACGCTTGGATGCGGATCCCTGCTAAAGGAAGCGGAACACG	Add *strAB-mad28*-F
VR154-R	GGTATGGCTAATCCGCCTCGGTCAGGGCCGGATCCCTAGTATGACGTCTGTCGCACCT	Add *strAB-mad28*-R
VR319-F	GTCATGGTCTTTTCGGCGAGCTTCTCTAGAATCTCCAAAAAGTTGCTGGGC	*mad10* deletion upstream
VR320-R	CCCATCCACTAAATTTAAATAGGATCCTCTTCCATGGCGTCCTCCG	*mad10* deletion upstream
VR321-F	TATTTAAATTTAGTGGATGGGGGATCCCCAGTGCGCAGCCGGCCTGA	*mad10* deletion downstream
VR322-R	GAAAATGCCGATATCCTATTGGCCTCTAGATCGCGGCCTGGGCC	*mad10* deletion downstream
VR323-F	CGACAATGCGCGGAGGACGCCATGGAAGAGCTGCTAAAGGAAGCGGAACAC	Add *strAB-mad10*-F
VR324-R	GAGATGATCTCAGGCCGGCTGCGCACTGGGCTAGTATGACGTCTGTCGCACC	Add *strAB-mad10*-R
VR277-F	AGACAGGATGAGGATCGTTTCGCGTCGACTGATCATCTCCCGGCGGG	*mad20* complementation in pAK906
VR278-R	GGGAATTCGAGCTCGGTACCCGGGGATCCTGCGCCGCTCCTGGATTC	*mad20* complementation in pAK906
CG220-R	GAGCTCGGTACCCGGGGATCCTCTAGAACTTGCTTTTCCGCCGTCATAC	*mad23* complementation in pAK906
CG221-F	CAAGAGACAGGATGAGGATCGTTTCGCGATGGAAGACGCCATGAGCTC	*mad23* complementation in pAK906
VR335-F	AAGCCAAGAAAAACGTCGCCAACGTCGACTATGGCCCTTTTTAAAGCTGACG	mad25 complementation in pAK907
VR336-R	GGGAATTCGAGCTCGGTACCCGGGGATCCTCTACCCGTCTGCGACGTC	*mad25* complementation in pAK907

VR337-F	AGACAGGATGAGGATCGTTTCGCGTCG ACTATGGAAGAAAATACCCGCTACA	*mad10* complementation in pAK906
VR338R	GGGAATTCGAGCTCGGTACCCGGGGA TCCTTCAGGCCGGCTGCG	*mad10* complementation in pAK906
VR355-F	AAGCCAAGAAAAACGTCGCCAACGTC GACTATGGACGGAATGCAGCGC	*mad26* complementation in pAK907
VR356-R	GGGAATTCGAGCTCGGTACCCGGGGA TCCTTCATTTATTCAAGGCAATAGTCA GT	*mad26* complementation in pAK907
VR357-F	AGACAGGATGAGGATCGTTTCGCGTCG ACTATGTCCGGAAGCAACGTGC	*mamK* complementation in pAK906
VR358-R	GGGAATTCGAGCTCGGTACCCGGGGA TCCTTTAATCCTTTCGCAGCTCGTC	*mamK* complementation in pAK906
VR375-F	AAGCCAAGAAAAACGTCGCCAACGTC GACTACAGCTCTGGCGCTCTTG	*mad28* complementation in pAK907 (with P*mad28* & alt-start)
VR372-R	GGGAATTCGAGCTCGGTACCCGGGGA TCCTCTAATCCGCCTCGGTCAGG	*mad28* complementation in pAK907 (with P*mad28* & alt-start)

Supplemental Table 4. *Table of all primers used in this study*

		Compared with:	Mann-Whitney U test		Welch's T-Test	
Figure	**Strain/ Condition**	**Strain/ Condition**	**pValue**	**Significance**	**pValue**	**Significance**
Figure 3C	Early	Late	<0.0001	****	<0.0001	****
Figure 3D	Early	Late	<0.0001	****	<0.0001	****
Figure 3E	Early	Late	<0.0001	****	<0.0001	****
Figure 3I	Immature crystals	Mature crystals	---	---	0.0006	***

Supplemental Table 5. *Table of all statistical tests used for figure 3 in this study*

		Compared with:	One way ANOVA test		Mann-Whitney U test	
Figure	**Strain/ Condition**	**Strain/ Condition**	**pValue**	**Significance**	**pValue**	**Significance**
Figure 4D	*fmpA*	WT	<0.0001	****	<0.0001	****
Figure 4D	*fmpB*	WT	<0.0001	****	<0.0001	****
Figure 4E	*fmpA*	WT	<0.0001	****	<0.0001	****
Figure 4E	*fmpB*	WT	<0.0001	****	<0.0001	****
Figure 4F	*fmpA*	WT	<0.0001	****	<0.0001	****
Figure 4F	*fmpB*	WT	<0.0001	****	<0.0001	****

Supplemental Table 6. *Table of all statistical tests used for figure 4 in this study*

		Compared with:	One way ANOVA test		Mann-Whitney U test	
Figure	**Strain/ Condition**	**Strain/ Condition**	**pValue**	**Significance**	**pValue**	**Significance**
Figure 6D	Δ*mad10*	WT	0.1364	ns	0.0005	***
Figure 6D	Δ*mad20*	WT	0.7606	ns	0.3754	ns
Figure 6D	Δ*mad23*	WT	0.7606	ns	0.5328	ns
Figure 6D	Δ*mad25*	WT	0.3521	ns	0.0147	*
Figure 6D	Δ*mad26*	WT	0.4881	ns	0.111	ns
Figure 6D	Δ*mad28*	WT	0.7606	ns	0.3365	ns
Figure 6D	Δ*mamK*	WT	<0.0001	****	<0.0001	****

		Compared with:	One way ANOVA test	
Figure	**Strain/Condition**	**Strain/Condition**	**pValue**	**Significance**
Figure 6E	Δ*mad10*	WT	<0.0001	****
Figure 6E	Δ*mad20*	WT	0.0001	***
Figure 6E	Δ*mad23*	WT	0.5127	ns
Figure 6E	Δ*mad25*	WT	0.9895	ns
Figure 6E	Δ*mad26*	WT	0.0953	ns
Figure 6E	Δ*mad28*	WT	0.0381	*
Figure 6E	Δ*mamK*	WT	<0.0001	****

		Compared with:	Kruskal-Wallis test	
Figure	**Strain/Condition**	**Strain/Condition**	**pValue**	**Significance**
Figure 6F	Δ*mad10*	WT	<0.0001	****
Figure 6F	Δ*mad20*	WT	<0.0001	****
Figure 6F	Δ*mad23*	WT	0.2744	ns
Figure 6F	Δ*mad25*	WT	0.0073	**
Figure 6F	Δ*mad26*	WT	0.0805	ns
Figure 6F	Δ*mad28*	WT	0.0007	***
Figure 6F	Δ*mamK*	WT	<0.0001	****

Supplemental Table 7. *Table of all statistical tests used for figure 6 in this study*

		Compared with:	One way ANOVA test		Mann-Whitney U test	
Figure	**Strain/ Condition**	**Strain/ Condition**	**pValue**	**Significance**	**pValue**	**Significance**
Figure 7F	Δ*mamK*	WT	<0.0001	****	<0.0001	****
Figure 7F	Δ*mad28*	WT	0.9378	ns	0.4697	ns
Figure 7G	Δ*mamK*	WT	<0.0001	****	<0.0001	****
Figure 7G	Δ*mad28*	WT	0.0703	ns	0.0053	**

Supplemental Table 8. *Table of all statistical tests used for figure 7 in this study*

Chapter 3

Uncovering the mechanisms for magnetosome inhibition in a hydrogen environment

Virginia V. Russell[1], Shannon O'Brien[2] and Arash Komeili[1]

[1] Plant and Microbiology, University of California Berkeley, Berkeley, California, USA.
[2]Berkeley City College, Berkeley, California, USA.

Section 1: Introduction

Magnetotactic Bacteria (MTB) constitute a diverse, ubiquitous group of bacteria adept at navigating along the Earth's geomagnetic field in search of the optimal environment, employing a specialized organelle known as the magnetosome. This organelle consists of a lipid bilayer membrane that encases a magnetic crystal, usually composed of either magnetite (Fe_3O_4) or greigite (Fe_3S_4) (*4*). It is believed that magnetotaxis, the capacity to align in magnetic fields, operates in conjunction with chemotaxis, enabling MTB to position themselves in the most favorable oxygen zone within a sediment or water column. This zone is typically at or just below the oxic/anoxic interface, depending on the species (*5*) (Figure 1). However, for strictly anaerobic MTB, it may also involve seeking zones that have, or lack, other elemental species, located at deeper levels within the water column (Figure 1). In a study conducted by Bidaud et al., it was posited that certain MTB utilize their magnetosomes to navigate towards varied redox gradients that facilitate diverse metabolic processes, such as sulfur and phosphorus metabolisms (*101*). This stands in contrast to microaerobic MTB, which have been demonstrated to employ magnetosomes for magneto-aerotaxis, navigating along geomagnetic field lines to locate the most favorable oxygen concentrations (*102–104*).

Desulfovibrio magneticus RS-1 is a dissimilatory sulfate-reducing bacterium, belonging to the delta-Proteobacteria sub-phylum, that synthesizes a single chain of irregular tooth-shaped magnetite magnetosomes. At the time of its discovery in 1993 (*16*), researchers were fascinated to find an MTB at lower levels in the water column where sulfate reduction is occurring (*16*). One cause is that the bacterial reduction of sulfate leads to the generation of hydrogen sulfide, which can then react with iron to create a precipitate of iron sulfide (*16*). Therefore, finding sulfate reducing bacteria that are capable of producing magnetite magnetosomes was intriguing. Furthermore, the isolation of magnetotactic bacteria in strictly anaerobic settings supports the hypothesis that some MTB might employ magnetosomes for magnetotaxis to locate the ideal redox environment instead of varying concentrations of oxygen. In chapter 2, we discovered that when RS-1 is grown in the presence of hydrogen it no longer synthesizes magnetosomes. We were also able to show that in hydrogen conditions magnetosome synthesis is not limited by iron availability as is seen when RS-1 is grown in the presence of sulfate (*17*). Here, in this study, we are aiming to uncover the mechanism for the regulation of magnetosome production in a hydrogen environment, which might help shed light onto the function of magnetosomes in strictly anaerobic environments. We used an evolution experiment to search for a gene or set of genes that are responsible for controlling magnetosomes production in different environmental conditions.

Section 2: Results/Discussion:

In chapter 2 we discovered when *Desulfovibrio magneticus* RS-1 is grown in the presence of hydrogen it no longer synthesizes magnetosomes. Additionally, we showed that another iron organelle, the ferrosome, can be synthesized in a hydrogen environment leading us the conclusion that iron availability is not hindering the production of magnetosomes (Chapter 2). Therefore, our subsequent question was whether the synthesis of magnetosomes is genetically regulated under varying conditions. To address this, we did an evolution experiment (Figure 2), where we grew 3 cultures of WT RS-1 (samples A, B, and C) in a medium infused with hydrogen. To select for magnetic cells, during each transfer we passed the entire 10 mL cultures through a magnetic column (Figure 2). During growth we measured the optical density and the

magnetic response. We were looking for a culture that had a significant magnetic response (C_{Mag}).

The initial several transfers using the magnetic columns did not exhibit a significant rise in C_{Mag}; however, by the fifth and sixth columns transfers, samples B and C began to show a magnetic reaction (Figure 3). Sample A never became magnetic (Figure 3). These results indicate that samples B and C are dominated by RS-1 mutants that can synthesize magnetosomes under hydrogen conditions. Therefore, we isolated genomic DNA from the cultures and sequenced them to find possible mutations. Interestingly, there was one gene that showed several mutations in both the B and C communities. This gene is annotated with a HAMP domain, a PAS domain, and a Methyl accepting chemotaxis sensing protein domain. In addition, there are two transmembrane domains. (Figure 4 and Figure 5). HAMP (histidine kinases, adenylyl cyclases, methyl-accepting chemotaxis proteins, and phosphatases) domains are a common component in numerous bacterial signal transduction proteins (*105*). This result suggests that RS-1 can detect hydrogen in its surroundings and that when cultivated in a hydrogen-rich environment, there may be a genetic response that controls magnetosome synthesis, ceasing the production of magnetosomes in that environment.

In conclusion, when *Desulfovibrio magneticus* RS-1 is cultured in an environment containing hydrogen, it inhibits the production of magnetosomes. A similar feature is noted in *Magnetospirillum magneticum* AMB-1 and *Magnetospirillum gryphiswaldense* MSR-1, both microaerobic alpha-Proteobacteria MTB. However, in these species, the phenomenon is triggered by elevated oxygen levels rather than hydrogen, leading to a cessation or significant reduction in magnetosome production under oxygen-rich conditions (*46*, *47*). It is believed that the function of magnetosomes, magnetotaxis, enables MTB to use the Earth's geomagnetic fields to align themselves in the most favorable oxygen zone within a sediment or water column. Yet, it is curious why in the presence of high levels of oxygen AMB-1 and MSR-1 ceases the production of magnetosomes because if the cells are in environments with higher concentrations of oxygen it would make it more difficult to move to a more favorable environment. In a similar way it is curious why RS-1 would stop the production of magnetosomes in hydrogen environments. Here, we showed there might be a potential genetic regulation occurring to prevent magnetosomes from forming, yet more research is necessary to prove this phenomenon. Looking deeper into the mechanism for inhibiting magnetosomes synthesis, in future studies, will likely shed light into the question regarding not only what the mechanism is, but also why this might be happening.

Section 3: Methods

3.1 General Culturing for RS-1

Desulfovibrio magneticus RS-1 strains were grown at 30°C anaerobically in RS-1 growth medium (RGM), as described previously (*24*, *25*). For growth with hydrogen, the medium was gassed with 10% hydrogen balanced with Nitrogen prior to autoclaving the medium. Additionally, after inoculating, the headspace was re-gassed with the same concentration of hydrogen nitrogen gas for 10 minutes. All hydrogen cultures were grown spinning on a wheel in the 30°C incubator. Only nitrogen cultures that were used as controls for hydrogen cultures were grown on a wheel in the incubator; all other nitrogen cultures were not grown shaking. Optical density and magnetic response via C_{Mag} were monitored throughout growth for all experiments as previously described (*25*).

3.2 Evolution experiment

Wild-type strain of *Desulfovibrio magneticus* RS-1 was cultured from a colony into Balch tubes containing 10 mL of nitrogen-infused medium to confirm magnetosome production as previously detailed. Subsequently, these cultures were transferred into Balch tubes with 10 mL of hydrogen-infused medium, using the procedure outlined earlier. Before the evolution experiment commenced, the culture underwent an additional transfer into 10 mL of hydrogen-infused medium to guarantee the absence of magnetosomes, making this culture the initial inoculum for the experiment. To verify the lack of magnetosomes, a magnetic response was measured using C_{Mag}. This initial culture was used to inoculate three Balch tubes with 10 mL of hydrogen infused medium with 0.5 mL of inoculum (Figure 2). Four days later, in the anaerobic chamber, each culture tube was passed through a magnetic column with magnets added to the sides of the column. The flow through was collected and the columns were washed with the same volume of sterile media (RGM), then the magnets were removed and 3 mL of RGM was used to elute any magnetic cells from the column (Figure 2). That elution was used to inoculate the next set of Balch tubes with 10 mL of hydrogen infused medium (Figure 2). This procedure was carried out for each transfer, occurring biweekly. For each transfer, the cultures were assessed by measuring optical density and magnetic response using C_{Mag}, aiming to detect any cultures exhibiting a magnetic response, an indicator of mutations permitting magnetosome production.

3.3 Variant calling to find mutations

During the evolution experiment, when a culture was found to have a magnetic response, 1 mL of that culture was streaked onto RGM plates, while the remaining 9 mL was harvested for DNA extraction to sequence the entire community. When the plates grew up, individual colonies were used to inoculate Balch tubes with 10 mL of hydrogen infused RGM. Subsequently, when the cultures tubes grew up optical density and magnetic response via C_{Mag} were measured and magnetic cultures were saved for DNA extractions to send for sequencing as well. All sequencing was performed by SeqCenter in Pittsburgh, PA, with 200 Mbp Illumina Whole Genome Sequencing and mutations were searched for using variant calling with Breseq (*106*).

Section 4: Acknowledgements

A.K. and V.V.R. are supported through the National Institute of General Medical Sciences (R35GM127114). S.O. was supported in part by the U.S. Department of Energy, Office of Science, Office of Workforce Development for Teachers and Scientists (WDTS) under the Community College Internship (CCI) program.

Figures

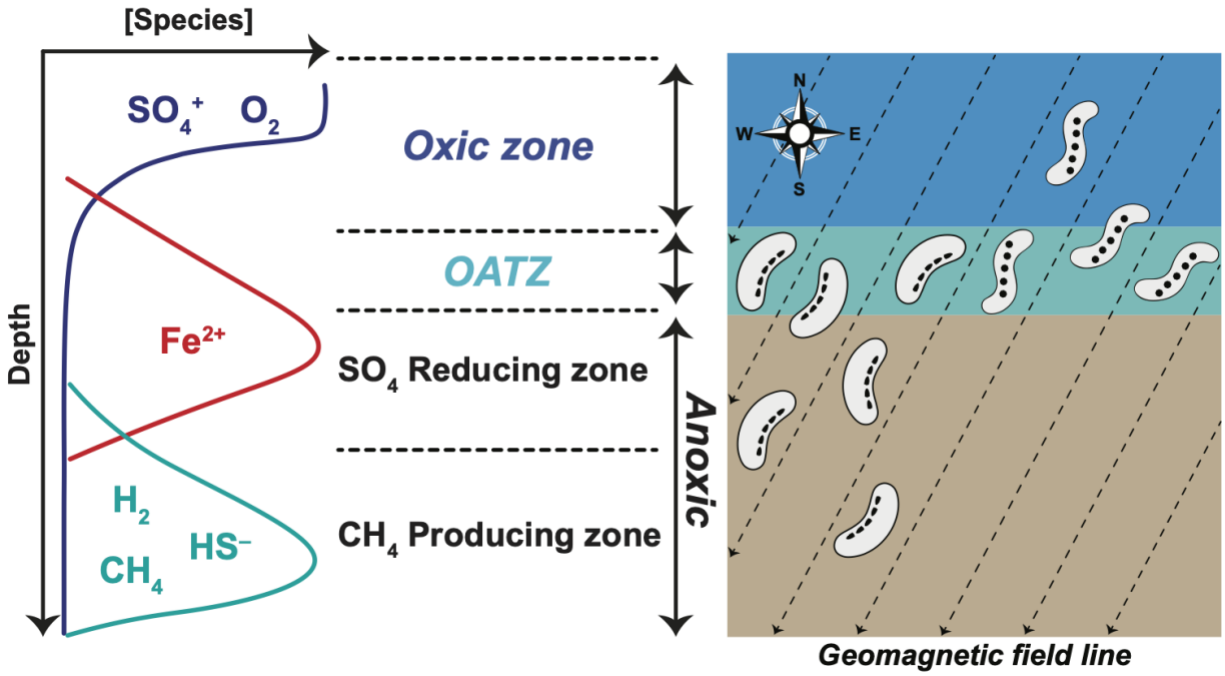

Figure 1. *Water column model*

(Left) depicts examples of main geochemical gradients in a water column. (Right) shows location of MTB in a water column.

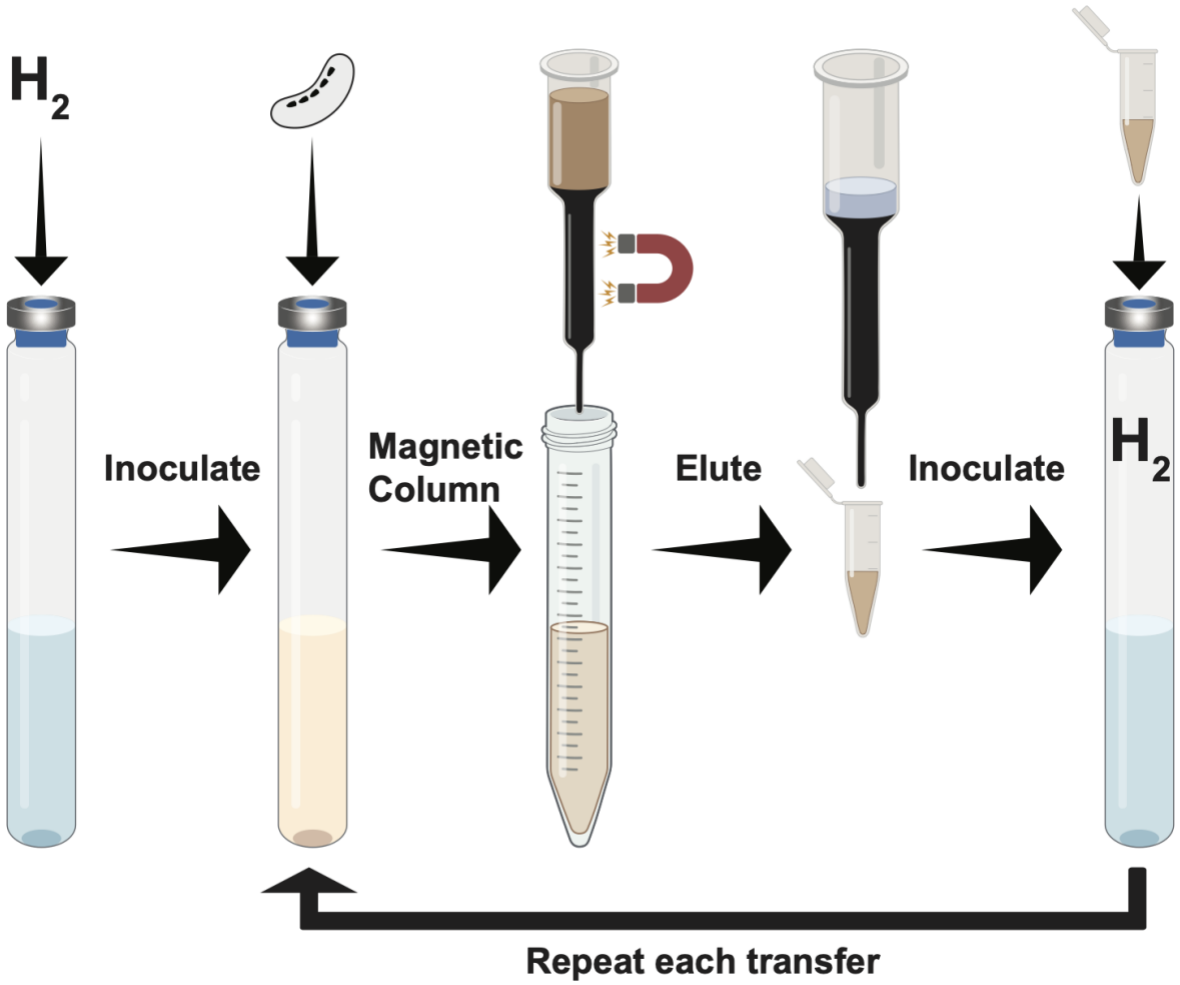

Figure 2. *Diagram of Evolution experiment in hydrogen environment*

Experimental design for the evolution experiment. More details about this method is described in the methods section.

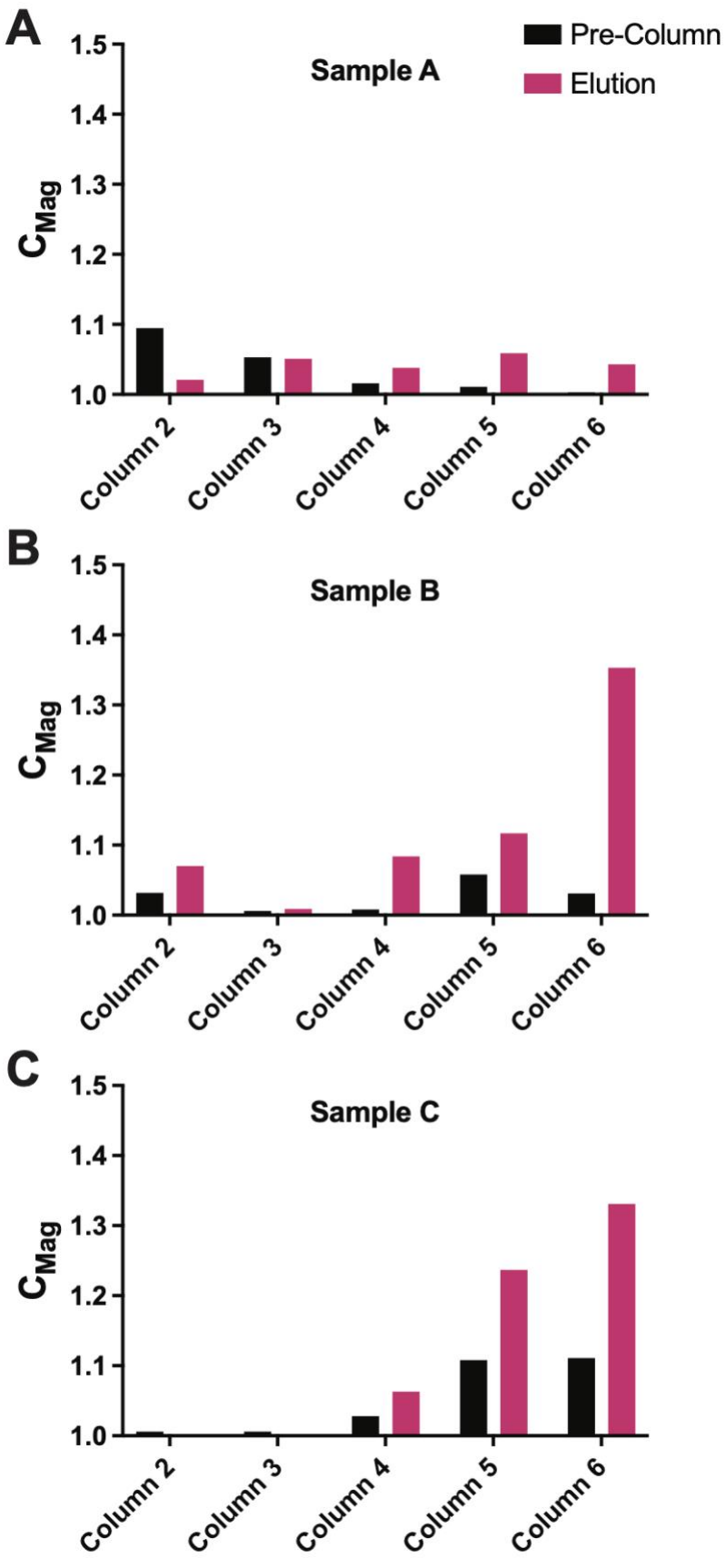
A
Pre-Column
Elution
Sample A
C_{Mag}
1.5
1.4
1.3
1.2
1.1
1.0
Column 2
Column 3
Column 4
Column 5
Column 6
B
Sample B
C
Sample C

Figure 3. *Magnetic response before and after magnetic columns for each transfer*

Each culture transfer during the evolution experiment the magnetic response was measured and calculated using C_{Mag} as described previously (*25*). The C_{Mag} was measured before and after the culture was passed through the column. 1.0 represents no magnetic response, whereas 1.3 represents a good magnetic response. WT RS-1 grown in nitrogen conditions can have a magnetic response ranging from 1.4 to 1.8.

A

Sample B

Predicted mutations						
evidence	seq id	position	mutation	annotation	gene	description
RA	contig_13	12,458	2 bp→GT	intergenic (+245/+586)	*trnfM* → / ← *NAEEGL_04360*	tRNA-fMet(cat)/hypothetical protein
RA	contig_13	13,024	C→T	intergenic (+811/+21)	*trnfM* → / ← *NAEEGL_04360*	tRNA-fMet(cat)/hypothetical protein
RA	contig_13	13,038	T→G	intergenic (+825/+7)	*trnfM* → / ← *NAEEGL_04360*	tRNA-fMet(cat)/hypothetical protein
RA	contig_13	13,051	G→A	A66A (GCC→GCT)	*NAEEGL_04360* ←	hypothetical protein
RA	contig_13	13,054	G→A	S65T (TCC→ACT)	*NAEEGL_04360* ←	hypothetical protein
RA	contig_13	13,056	A→T	S65T (TCC→ACT)	*NAEEGL_04360* ←	hypothetical protein
RA	contig_133	38	C→G	intergenic (–/-61)	– / → *NAEEGL_19480*	–/Superoxide dismutase
RA	contig_136	74	G→T	intergenic (–/+213)	– / ← *NAEEGL_19685*	–/4Fe-4S ferredoxin-type domain-containing protein
RA	contig_23	4,181	A→G	K70K (AAA→AAG)	*NAEEGL_06995* →	HAMP domain-containing protein
RA	contig_23	4,208	A→C	E79D (GAA→GAC)	*NAEEGL_06995* →	HAMP domain-containing protein
RA	contig_23	4,220	G→A	R83R (CGG→CGA)	*NAEEGL_06995* →	HAMP domain-containing protein
RA	contig_23	4,286	C→T	N105N (AAC→AAT)	*NAEEGL_06995* →	HAMP domain-containing protein
RA	contig_23	4,440	G→A	A157T (GCT→ACT)	*NAEEGL_06995* →	HAMP domain-containing protein
RA	contig_23	4,451	G→A	L160L (TTG→TTA)	*NAEEGL_06995* →	HAMP domain-containing protein
RA	contig_23	4,475	C→T	T168T (ACC→ACT)	*NAEEGL_06995* →	HAMP domain-containing protein
RA	contig_23	4,517	Δ1 bp	coding (546/2469 nt)	*NAEEGL_06995* →	HAMP domain-containing protein
RA	contig_23	5,249	C→A	G426G (GGC→GGA)	*NAEEGL_06995* →	HAMP domain-containing protein
RA	contig_23	5,282	Δ1 bp	coding (1311/2469 nt)	*NAEEGL_06995* →	HAMP domain-containing protein
RA	contig_23	5,288	+T	coding (1317/2469 nt)	*NAEEGL_06995* →	HAMP domain-containing protein
RA	contig_23	5,318	T→C	I449I (ATT→ATC)	*NAEEGL_06995* →	HAMP domain-containing protein
MC	contig_286	1	Δ398 bp	intergenic (–/–)	– / –	–/–
MC	contig_296	1	Δ287 bp	intergenic (–/–)	– / –	–/–
MC	contig_297	1	Δ287 bp	intergenic (–/–)	– / –	–/–
RA	contig_3	61	2 bp→CC	intergenic (–/+328)	– / ← *purM*	–/Phosphoribosylformylglycinamidine cyclo-ligase
MC	contig_307	1	Δ219 bp	intergenic (–/–)	– / –	–/–
RA	contig_312	72	T→C	intergenic (–/–)	– / –	–/–
MC	contig_314	1	Δ164 bp	intergenic (–/–)	– / –	–/–

B

Sample C

Predicted mutations						
evidence	seq id	position	mutation	annotation	gene	description
RA	contig_13	12,458	2 bp→GT	intergenic (+245/+586)	*trnfM* → / ← *NAEEGL_04360*	tRNA-fMet(cat)/hypothetical protein
RA	contig_13	13,024	C→T	intergenic (+811/+21)	*trnfM* → / ← *NAEEGL_04360*	tRNA-fMet(cat)/hypothetical protein
RA	contig_13	13,038	T→G	intergenic (+825/+7)	*trnfM* → / ← *NAEEGL_04360*	tRNA-fMet(cat)/hypothetical protein
RA	contig_13	13,051	G→A	A66A (GCC→GCT)	*NAEEGL_04360* ←	hypothetical protein
RA	contig_13	13,054	G→A	S65T (TCC→ACT)	*NAEEGL_04360* ←	hypothetical protein
RA	contig_13	13,056	A→T	S65T (TCC→ACT)	*NAEEGL_04360* ←	hypothetical protein
RA	contig_23	4,112	T→A	R47R (CGT→CGA)	*NAEEGL_06995* →	HAMP domain-containing protein
RA	contig_23	4,142	T→G	G57G (GGT→GGG)	*NAEEGL_06995* →	HAMP domain-containing protein
RA	contig_23	4,181	A→G	K70K (AAA→AAG)	*NAEEGL_06995* →	HAMP domain-containing protein
RA	contig_23	4,208	A→C	E79D (GAA→GAC)	*NAEEGL_06995* →	HAMP domain-containing protein
RA	contig_23	4,220	G→A	R83R (CGG→CGA)	*NAEEGL_06995* →	HAMP domain-containing protein
RA	contig_23	4,286	C→T	N105N (AAC→AAT)	*NAEEGL_06995* →	HAMP domain-containing protein
RA	contig_23	4,440	G→A	A157T (GCT→ACT)	*NAEEGL_06995* →	HAMP domain-containing protein
RA	contig_23	4,451	G→A	L160L (TTG→TTA)	*NAEEGL_06995* →	HAMP domain-containing protein
RA	contig_23	4,475	C→T	T168T (ACC→ACT)	*NAEEGL_06995* →	HAMP domain-containing protein
RA	contig_23	4,517	Δ1 bp	coding (546/2469 nt)	*NAEEGL_06995* →	HAMP domain-containing protein
RA	contig_23	5,249	C→A	G426G (GGC→GGA)	*NAEEGL_06995* →	HAMP domain-containing protein
RA	contig_23	5,282	Δ1 bp	coding (1311/2469 nt)	*NAEEGL_06995* →	HAMP domain-containing protein
RA	contig_23	5,288	+T	coding (1317/2469 nt)	*NAEEGL_06995* →	HAMP domain-containing protein
RA	contig_23	5,318	T→C	I449I (ATT→ATC)	*NAEEGL_06995* →	HAMP domain-containing protein
MC	contig_286	1	Δ398 bp	intergenic (–/–)	– / –	–/–
MC	contig_296	1	Δ287 bp	intergenic (–/–)	– / –	–/–
MC	contig_297	1	Δ287 bp	intergenic (–/–)	– / –	–/–
RA	contig_3	61	2 bp→CC	intergenic (–/+328)	– / ← *purM*	–/Phosphoribosylformylglycinamidine cyclo-ligase
MC	contig_307	1	Δ219 bp	intergenic (–/–)	– / –	–/–
MC	contig_314	1	Δ164 bp	intergenic (–/–)	– / –	–/–
MC	contig_316	1	Δ116 bp	intergenic (–/–)	– / –	–/–

Figure 4. *Mutations for community B and C*

Using a variant calling program, BreSeq (*106*), sequencing reads for both communities, Sample B and Sample C, were compared to the WT annotated genome. (A) shows the predicted mutations with the highest confidence for sample B and (B) shows the predicted mutations for sample C.

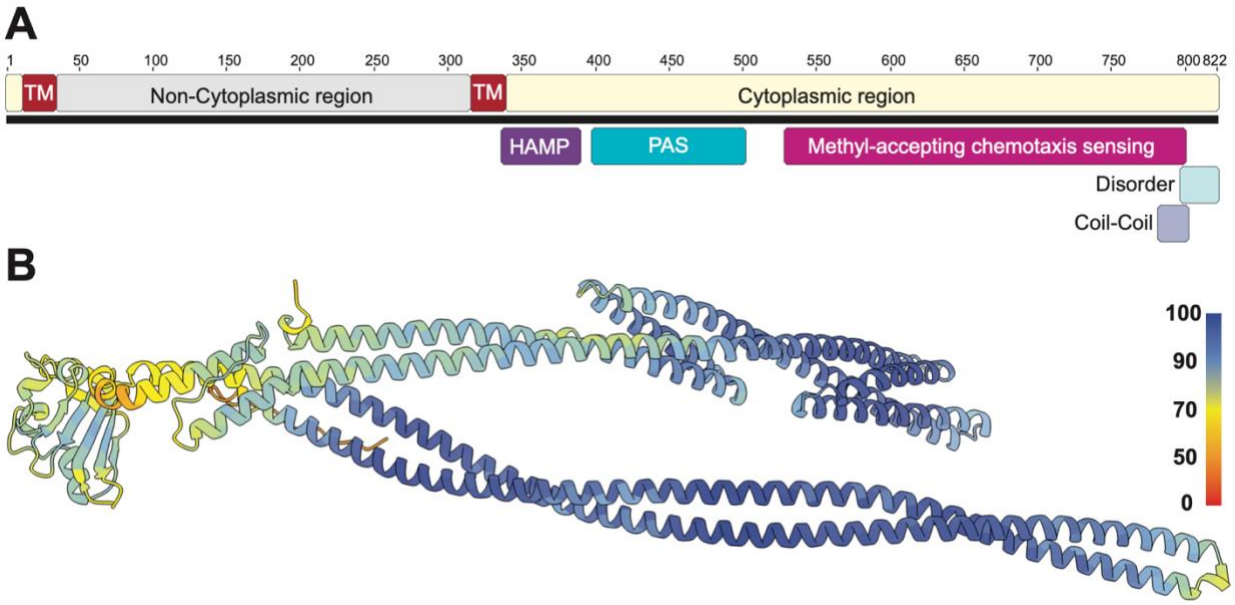

Figure 5. *Domain map and 3D protein structure of HAMP containing gene*

(A) Domain map of the gene with predicted mutations from evolution experiment. This gene contains a HAMP domain, a PAS domain, and a Methyl accepting chemotaxis sensing protein domain. In addition, there are two transmembrane domains. The domains were predicted using InterPro (*52*). (B). 3D protein structure of gene mutated in evolution experiment. Protein structure was generated using Alphafold2 with Colabs (*54*) and visualized using ChimeraX (*55*). The protein structure is colored according to the confidence level with blue being 100% confident and red representing 0% confident.

Chapter 4

Concluding remarks

Virginia V. Russell[1]

[1] *Plant and Microbiology, University of California Berkeley, Berkeley, California, USA.*

Conclusion

In conclusion, this study has greatly enhanced our knowledge of the mechanisms involved in magnetosome synthesis and organization in *Desulfovibrio magneticus* RS-1, a representative of the deep-branching magnetotactic bacteria (MTB). Prior to this work, our understanding of magnetosome formation and alignment was primarily derived from studies on two key model organisms: *Magnetospirillum magneticum* AMB-1 and *Magnetospirillum gryphiswaldense* MSR-1. Both of these MTB are part of the alpha-Proteobacteria sub-phylum and generate cubooctahedral magnetite crystals. However, as the phylogenetic tree of MTB expands, it becomes crucial to include representation from other MTB groups. In chapter 1 we discussed the diversity of magnetotactic bacteria and the need for models outside of the sub-phyla of alpha-Proteobacteria.

In Chapter 2, based on proteomic and genetic analyses, we have developed the following model for the stages of magnetosome formation in RS-1. The first step involves crystal nucleation, which occurs not at the cell's positive curvature but at several distinct sites. In the second step, crystal growth continues at the nucleation sites. Once the crystals reach a certain size in step three, the immature crystals are moved to the positive curvature of the cell. At this stage, it is likely that Mad10 envelops the crystal, aiding the binding of chain organization proteins. After Mad10 has coated the crystal, Mad28 then engages with the magnetosome, guiding it towards the positive curvature. As the crystals migrate to this curvature, the biomineralization shifts towards chain organization. During the initial stage of this organization in step four, we observe one or two mature crystals at the positive curvature. When multiple crystals come together, Mad23 links them, sparking the creation of sub-chains. In step five, further sub-chains begin to form. MamK plays a crucial role in separating these sub-chains and arranging them along the cell’s length. Finally, in step six, more crystals are progressively integrated into the existing sub-chains to complete the magnetosome chain.

Additionally, Chapter 2 reveals that when *Desulfovibrio magneticus* RS-1 is cultivated in the presence of hydrogen, it ceases to produce magnetosomes. A similar behavior is noted in AMB-1 and MSR-1, although in these cases, the suppression occurs under conditions of high oxygen rather than hydrogen (*46*, *47*). In both instances, magnetosome proteins remain present even though magnetosomes are not formed (*48*). Similar to MSR-1 and AMB-1, a set of magnetosome proteins in RS-1 are constitutively translated. Subsequently, in Chapter 3 we implemented an alternative method to explore the inhibition of magnetosome synthesis in the presence of hydrogen, using a genetic screening approach. This investigation identified a potential gene featuring a HAMP-domain, which could play a role in controlling magnetosome production under hydrogen-rich conditions. Thus, it appears that magnetosome production is regulated at the transcriptional or translational level, yet the proteomics analysis suggests that not all magnetosome proteins cease translation, indicating that the regulation might be more specific and targeted. Furthermore, the absence of magnetosomes is not due to a lack of iron availability since RS-1 can still produce ferrosomes, iron-rich granules, under these conditions (Chapter 2). Therefore, beyond iron availability and translation of magnetosome protein, there must be an additional regulatory mechanism affecting magnetosome synthesis. Additionally, a benefit of discovering magnetosome production is inhibited in hydrogen, is the possibility of using this feature as a tool for investigating different phases of biomineralization. Prior to this revelation, the synchronization of biomineralization relied on inducing iron starvation. However, this approach led to the production of ferrosomes, making it impossible to distinguish immature magnetosomes from ferrosomes. Therefore, it made observing early stages of biomineralization

nearly impossible. Utilizing hydrogen, we are able to capture the early stages of biomineralization in much more detail.

In closing, this research has greatly expanded our knowledge of the mechanism behind magnetosome synthesis and organization in *Desulfovibrio magneticus* RS-1. The proposed model for magnetosome synthesis and organization in RS-1, outlined in Chapter 2, is remarkably different from the established mechanisms in both AMB-1 and MSR-1. This highlights the significance of investigating magnetosome formation across a wider range of Magnetotactic bacterial species, especially in the deeper branching MTB. As the phylogenetic tree of MTB continues to grow, it has become more and more evident that we require additional model systems beyond those in the alpha-Proteobacteria sub-phyla.

References

1. S. Mann, “Mineralization in biological systems” in *Inorganic Elements in Biochemistry*, P. H. Connett, H. Folłmann, M. Lammers, S. Mann, J. D. Odom, K. E. Wetterhahn, Eds. (Springer, Berlin, Heidelberg, 1983), pp. 125–174.

2. H. A. Lowenstam, Minerals Formed by Organisms. *Science* **211**, 1126–1131 (1981).

3. J. Cosmidis, K. Benzerara, Why do microbes make minerals? *Comptes Rendus. Géoscience* **354**, 1–39 (2022).

4. A. Komeili, Molecular Mechanisms of Compartmentalization and Biomineralization in Magnetotactic Bacteria. *FEMS Microbiol Review* **36**, 232–255 (2012).

5. C. T. Lefevre, D. A. Bazylinski, Ecology, Diversity, and Evolution of Magnetotactic Bacteria. *Microbiology and Molecular Biology Reviews* **77**, 497–526 (2013).

6. M. Amor, F. P. Mathon, C. L. Monteil, V. Busigny, C. T. Lefevre, Iron-biomineralizing organelle in magnetotactic bacteria: function, synthesis and preservation in ancient rock samples. *Environmental Microbiology* **22**, 3611–3632 (2020).

7. S. Spring, K.-H. Schleifer, Diversity of Magnetotactic Bacteria. *Systematic and Applied Microbiology* **18**, 147–153 (1995).

8. P. Liu, Y. Zheng, R. Zhang, J. Bai, K. Zhu, K. Benzerara, N. Menguy, X. Zhao, A. P. Roberts, Y. Pan, J. Li, Key gene networks that control magnetosome biomineralization in magnetotactic bacteria. *National Science Review* **10**, nwac238 (2023).

9. R. Blakemore, Magnetotactic Bacteria. *Science* **190**, 377–379 (1975).

10. W. Lin, G. A. Paterson, Q. Zhu, Y. Wang, E. Kopylova, Y. Li, R. Knight, D. A. Bazylinski, R. Zhu, J. L. Kirschvink, Y. Pan, Origin of microbial biomineralization and magnetotaxis during the Archean. *Proceedings of the National Academy of Sciences* **114**, 2171–2176 (2017).

11. M. Uzun, V. Koziaeva, M. Dziuba, L. Alekseeva, M. Krutkina, M. Sukhacheva, R. Baslerov, D. Grouzdev, Recovery and genome reconstruction of novel magnetotactic Elusimicrobiota from bog soil. *The ISME Journal* **17**, 204–214 (2023).

12. W. Lin, W. Zhang, X. Zhao, A. P. Roberts, G. A. Paterson, D. A. Bazylinski, Y. Pan, Genomic expansion of magnetotactic bacteria reveals an early common origin of magnetotaxis with lineage-specific evolution. *ISME Journal* **12**, 1508–1519 (2018).

13. C. L. Monteil, N. Menguy, S. Prévéral, A. Warren, D. Pignol, C. T. Lefèvre, Accumulation and Dissolution of Magnetite Crystals in a Magnetically Responsive Ciliate. *Appl Environ Microbiol* **84**, e02865-17 (2018).

14. C. L. Monteil, D. Vallenet, N. Menguy, K. Benzerara, V. Barbe, S. Fouteau, C. Cruaud, M. Floriani, E. Viollier, G. Adryanczyk, N. Leonhardt, D. Faivre, D. Pignol, P. López-García, R. J. Weld, C. T. Lefevre, Ectosymbiotic bacteria at the origin of magnetoreception in a marine protist. *Nat Microbiol* **4**, 1088–1095 (2019).

15. P. Leão, L. Le Nagard, H. Yuan, J. Cypriano, I. Da Silva-Neto, D. A. Bazylinski, D. Acosta-Avalos, H. L. De Barros, A. P. Hitchcock, U. Lins, F. Abreu, Magnetosome magnetite biomineralization in a flagellated protist: evidence for an early evolutionary origin for magnetoreception in eukaryotes. *Environmental Microbiology* **22**, 1495–1506 (2020).

16. T. Sakaguchi, J. G. Burgess, T. Matsunaga, Magnetite formation by a sulphate-reducing bacterium. *Nature* **365**, 47–49 (1993).

17. T. Sakaguchi, A. Arakaki, T. Matsunaga, Desulfovibrio magneticus sp. nov., a novel sulfate-reducing bacterium that produces intracellular single-domain-sized magnetite particles. *International Journal of Systematic and Evolutionary Microbiology* **52**, 215–221 (2002).

18. R. Kawaguchi, Phylogenetic analysis of a novel sulfate-reducing magnetic bacterium, RS-1, demonstrates its membership of the δ-Proteobacteria. *FEMS Microbiology Letters* **126**, 277–282 (1995).

19. S. Mann, N. H. C. Sparks, R. B. Frankel, D. A. Bazylinski, H. W. Jannasch, Biomineralization of ferrimagnetic greigite (Fe3S4) and iron pyrite (FeS2) in a magnetotactic bacterium. *Nature* **343**, 258–261 (1990).

20. E. F. DeLong, R. B. Frankel, D. A. Bazylinski, Multiple Evolutionary Origins of Magnetotaxis in Bacteria. *Science* **259**, 803–806 (1993).

21. S. Spring, R. Amann, W. Ludwig, K.-H. Schleifer, H. Van Gemerden, N. Petersen, Dominating Role of an Unusual Magnetotactic Bacterium in the Microaerobic Zone of a Freshwater Sediment. *Appl Environ Microbiol* **59**, 2397–2403 (1993).

22. C. T. Lefèvre, N. Menguy, F. Abreu, U. Lins, M. Pósfai, T. Prozorov, D. Pignol, R. B. Frankel, D. A. Bazylinski, A Cultured Greigite-Producing Magnetotactic Bacterium in a Novel Group of Sulfate-Reducing Bacteria. *Science* **334**, 1720–1723 (2011).

23. C. T. Lefèvre, D. Trubitsyn, F. Abreu, S. Kolinko, C. Jogler, L. G. P. de Almeida, A. T. R. de Vasconcelos, M. Kube, R. Reinhardt, U. Lins, D. Pignol, D. Schüler, D. A. Bazylinski, N. Ginet, Comparative genomic analysis of magnetotactic bacteria from the Deltaproteobacteria provides new insights into magnetite and greigite magnetosome genes required for magnetotaxis. *Environmental Microbiology* **15**, 2712–2735 (2013).

24. M. E. Byrne, D. A. Ball, J.-L. Guerquin-Kern, I. Rouiller, T.-D. Wu, K. H. Downing, H. Vali, A. Komeili, *Desulfovibrio magneticus* RS-1 contains an iron- and phosphorus-rich organelle distinct from its bullet-shaped magnetosomes. *Proc. Natl. Acad. Sci. U.S.A.* **107**, 12263–12268 (2010).

25. L. Rahn-Lee, M. E. Byrne, M. Zhang, D. Le Sage, D. R. Glenn, T. Milbourne, R. L. Walsworth, H. Vali, A. Komeili, A Genetic Strategy for Probing the Functional Diversity of Magnetosome Formation. *PLoS Genet* **11**, e1004811 (2015).

26. C. R. Grant, L. Rahn-lee, K. N. Legault, Genome Editing Method for the Anaerobic Magnetotactic. *Applied and Environmental Microbiology* **84**, 1–12 (2018).

27. R. P. Awal, C. T. Lefevre, D. Schüler, Functional expression of foreign magnetosome genes in the alphaproteobacterium *Magnetospirillum gryphiswaldense*. *mBio*, e03282-22 (2023).

28. R. P. Awal, F. D. Müller, D. Pfeiffer, C. L. Monteil, G. Perrière, C. T. Lefèvre, D. Schüler, Experimental analysis of diverse actin-like proteins from various magnetotactic bacteria by functional expression in *Magnetospirillum gryphiswaldense*. *mBio* **14**, e01649-23 (2023).

29. H. Shimoshige, H. Kobayashi, S. Shimamura, T. Mizuki, A. Inoue, T. Maekawa, Isolation and cultivation of a novel sulfate-reducing magnetotactic bacterium belonging to the genus Desulfovibrio. *PLoS ONE* **16**, e0248313 (2021).

30. H. Ehrlich, E. Bailey, M. Wysokowski, T. Jesionowski, Forced Biomineralization: A Review. *Biomimetics* **6**, 46 (2021).

31. I. Kolinko, A. Lohße, S. Borg, O. Raschdorf, C. Jogler, Q. Tu, M. Pósfai, É. Tompa, J. M. Plitzko, A. Brachmann, G. Wanner, R. Müller, Y. Zhang, D. Schüler, Biosynthesis of magnetic nanostructures in a foreign organism by transfer of bacterial magnetosome gene clusters. *Nature Nanotech* **9**, 193–197 (2014).

32. C. R. Grant, M. Amor, H. A. Trujillo, S. Krishnapura, A. T. Iavarone, A. Komeili, Distinct gene clusters drive formation of ferrosome organelles in bacteria. *Nature* **606**, 160–164 (2022).

33. H. Pi, R. Sun, J. R. McBride, A. R. S. Kruse, K. N. Gibson-Corley, E. S. Krystofiak, M. R. Nicholson, J. M. Spraggins, Q. Zhou, E. P. Skaar, Clostridioides difficile ferrosome organelles combat nutritional immunity. *Nature* **623**, 1009–1016 (2023).

34. J. Li, N. Menguy, C. Gatel, V. Boureau, E. Snoeck, G. Patriarche, E. Leroy, Y. Pan, Crystal growth of bullet-shaped magnetite in magnetotactic bacteria of the *Nitrospirae* phylum. *J. R. Soc. Interface.* **12**, 20141288 (2015).

35. S. Ben-Shimon, D. Stein, R. Zarivach, Current view of iron biomineralization in magnetotactic bacteria. *Journal of Structural Biology: X* **5**, 100052 (2021).

36. E. Cornejo, P. Subramanian, Z. Li, G. J. Jensen, A. Komeili, Dynamic Remodeling of the Magnetosome Membrane Is Triggered by the Initiation of Biomineralization. *mBio* **7**, e01898-15 (2016).

37. A. Pohl, F. Berger, R. M. A. Sullan, C. Valverde-Tercedor, K. Freindl, N. Spiridis, C. T. Lefèvre, N. Menguy, S. Klumpp, K. G. Blank, D. Faivre, Decoding Biomineralization:

Interaction of a Mad10-Derived Peptide with Magnetite Thin Films. *Nano Lett.* **19**, 8207–8215 (2019).

38. A. Pohl, S. A. E. Young, T. C. Schmitz, D. Farhadi, R. Zarivach, D. Faivre, K. G. Blank, Magnetite-binding proteins from the magnetotactic bacterium *Desulfamplus magnetovallimortis* BW-1. *Nanoscale* **13**, 20396–20400 (2021).

39. J. Wan, C. L. Monteil, A. Taoka, G. Ernie, K. Park, M. Amor, E. Taylor-Cornejo, C. T. Lefevre, A. Komeili, McaA and McaB control the dynamic positioning of a bacterial magnetic organelle. *Nat Commun* **13**, 5652 (2022).

40. N. Abreu, S. Mannoubi, E. Ozyamak, D. Pignol, N. Ginet, A. Komeili, Interplay between Two Bacterial Actin Homologs, MamK and MamK-Like, Is Required for the Alignment of Magnetosome Organelles in Magnetospirillum magneticum AMB-1. *J Bacteriol* **196**, 3111–3121 (2014).

41. A. Komeili, Z. Li, D. K. Newman, G. J. Jensen, Magnetosomes Are Cell Membrane Invaginations Organized by the Actin-Like Protein MamK. *Science* **311**, 242–245 (2006).

42. M. Toro-Nahuelpan, F. D. Müller, S. Klumpp, J. M. Plitzko, M. Bramkamp, D. Schüler, Segregation of prokaryotic magnetosomes organelles is driven by treadmilling of a dynamic actin-like MamK filament. *BMC Biol* **14**, 88 (2016).

43. A. Taoka, A. Kiyokawa, C. Uesugi, Y. Kikuchi, Z. Oestreicher, K. Morii, Y. Eguchi, Y. Fukumori, Tethered Magnets Are the Key to Magnetotaxis: Direct Observations of *Magnetospirillum magneticum* AMB-1 Show that MamK Distributes Magnetosome Organelles Equally to Daughter Cells. *mBio* **8**, e00679-17 (2017).

44. E. Katzmann, A. Scheffel, M. Gruska, J. M. Plitzko, D. Schüler, Loss of the actin-like protein MamK has pleiotropic effects on magnetosome formation and chain assembly in *Magnetospirillum gryphiswaldense*. *Molecular Microbiology* **77**, 208–224 (2010).

45. M. Uzun, L. Alekseeva, M. Krutkina, V. Koziaeva, D. Grouzdev, Unravelling the diversity of magnetotactic bacteria through analysis of open genomic databases. *Sci Data* **7**, 252 (2020).

46. T. Matsunaga, T. Sakaguchi, F. Tadakoro, Magnetite formation by a magnetic bacterium capable of growing aerobically. *Appl Microbiol Biotechnol* **35** (1991).

47. D. Schüler, E. Baeuerlein, Dynamics of Iron Uptake and Fe $_3$ O $_4$ Biomineralization during Aerobic and Microaerobic Growth of *Magnetospirillum gryphiswaldense*. *J Bacteriol* **180**, 159–162 (1998).

48. S. Schübbe, C. Würdemann, J. Peplies, U. Heyen, C. Wawer, F. O. Glöckner, D. Schüler, Transcriptional Organization and Regulation of Magnetosome Operons in *Magnetospirillum gryphiswaldense*. *Appl Environ Microbiol* **72**, 5757–5765 (2006).

49. I.-M. A. Chen, K. Chu, K. Palaniappan, A. Ratner, J. Huang, M. Huntemann, P. Hajek, S. J. Ritter, C. Webb, D. Wu, N. J. Varghese, T. B. K. Reddy, S. Mukherjee, G. Ovchinnikova, M. Nolan, R. Seshadri, S. Roux, A. Visel, T. Woyke, E. A. Eloe-Fadrosh, N. C. Kyrpides, N. N. Ivanova, The IMG/M data management and analysis system v.7: content updates and new features. *Nucleic Acids Research* **51**, D723–D732 (2023).

50. K. Katoh, D. M. Standley, MAFFT multiple sequence alignment software version 7: improvements in performance and usability. *Mol Biol Evol* **30**, 772–780 (2013).

51. S. Guindon, J.-F. Dufayard, V. Lefort, M. Anisimova, W. Hordijk, O. Gascuel, New algorithms and methods to estimate maximum-likelihood phylogenies: assessing the performance of PhyML 3.0. *Syst Biol* **59**, 307–321 (2010).

52. T. Paysan-Lafosse, M. Blum, S. Chuguransky, T. Grego, B. L. Pinto, G. A. Salazar, M. L. Bileschi, P. Bork, A. Bridge, L. Colwell, J. Gough, D. H. Haft, I. Letunić, A. Marchler-Bauer, H. Mi, D. A. Natale, C. A. Orengo, A. P. Pandurangan, C. Rivoire, C. J. A. Sigrist, I. Sillitoe, N. Thanki, P. D. Thomas, S. C. E. Tosatto, C. H. Wu, A. Bateman, InterPro in 2022. *Nucleic Acids Research* **51**, D418–D427 (2023).

53. M. Kearse, R. Moir, A. Wilson, S. Stones-Havas, M. Cheung, S. Sturrock, S. Buxton, A. Cooper, S. Markowitz, C. Duran, T. Thierer, B. Ashton, P. Meintjes, A. Drummond, Geneious Basic: An integrated and extendable desktop software platform for the organization and analysis of sequence data. *Bioinformatics* **28**, 1647–1649 (2012).

54. M. Mirdita, K. Schütze, Y. Moriwaki, L. Heo, S. Ovchinnikov, M. Steinegger, ColabFold: making protein folding accessible to all. *Nat Methods* **19**, 679–682 (2022).

55. E. C. Meng, T. D. Goddard, E. F. Pettersen, G. S. Couch, Z. J. Pearson, J. H. Morris, T. E. Ferrin, UCSF ChimeraX: Tools for structure building and analysis. *Protein Sci* **32**, e4792 (2023).

56. J. Li, Y. Pan, Environmental Factors Affect Magnetite Magnetosome Synthesis in Magnetospirillum magneticum AMB-1: Implications for Biologically Controlled Mineralization. *Geomicrobiology Journal* **29**, 362–373 (2012).

57. T. Matsunaga, Y. Okamura, Y. Fukuda, A. T. Wahyudi, Y. Murase, H. Takeyama, Complete genome sequence of the facultative anaerobic magnetotactic bacterium Magnetospirillum sp. strain AMB-1. *DNA Res* **12**, 157–166 (2005).

58. D. Maratea, R. P. Blakemore, Aquaspirillum magnetotacticum sp. nov., a Magnetic Spirillum. *International Journal of Systematic and Evolutionary Microbiology* **31**, 452–455 (1981).

59. M. D. Smalley, G. K. Marinov, L. E. Bertani, G. DeSalvo, Genome Sequence of Magnetospirillum magnetotacticum Strain MS-1. *Genome Announc* **3**, e00233-15 (2015).

60. M. Dziuba, V. Koziaeva, D. Grouzdev, E. Burganskaya, R. Baslerov, T. Kolganova, A. Chernyadyev, G. Osipov, E. Andrianova, V. Gorlenko, B. Kuznetsov, Magnetospirillum

caucaseum sp. nov., Magnetospirillum marisnigri sp. nov. and Magnetospirillum moscoviense sp. nov., freshwater magnetotactic bacteria isolated from three distinct geographical locations in European Russia. *International Journal of Systematic and Evolutionary Microbiology* **66**, 2069–2077 (2016).

61. C. L. Monteil, D. S. Grouzdev, G. Perrière, B. Alonso, Z. Rouy, S. Cruveiller, N. Ginet, D. Pignol, C. T. Lefevre, Repeated horizontal gene transfers triggered parallel evolution of magnetotaxis in two evolutionary divergent lineages of magnetotactic bacteria. *The ISME Journal* **14**, 1783–1794 (2020).

62. L. Ke, Y. Chen, P. Liu, S. Liu, D. Wu, Y. Yuan, Y. Wu, M. Gao, Characteristics and optimised fermentation of a novel magnetotactic bacterium, Magnetospirillum sp. ME-1. *FEMS Microbiology Letters* **365**, fny052 (2018).

63. L. Ke, P. Liu, S. Liu, M. Gao, Complete Genome Sequence of Magnetospirillum sp. ME-1, a Novel Magnetotactic Bacterium Isolated from East Lake, Wuhan, China. *Genome Announc* **5**, e00485-17 (2017).

64. Y. Wang, W. Lin, J. Li, T. Zhang, Y. Li, J. Tian, L. Gu, Y. V. Heyden, Y. Pan, Characterizing and optimizing magnetosome production of Magnetospirillum sp. XM-1 isolated from Xi'an City Moat, China. *FEMS Microbiology Letters* **362**, fnv167 (2015).

65. Y. Wang, T. Zhang, W. Lin, B. Zhang, Y. Cai, C. Yang, J. Li, H. Xu, Y. Pan, Complete Genome Sequence of Magnetospirillum sp. Strain XM-1, Isolated from the Xi'an City Moat, China. *Genome Announc* **4**, e01171-16 (2016).

66. V. V. Koziaeva, M. V. Dziuba, T. M. Ivanov, B. B. Kuznetsov, K. G. Skryabin, D. S. Grouzdev, Draft Genome Sequences of Two Magnetotactic Bacteria, Magnetospirillum moscoviense BB-1 and Magnetospirillum marisnigri SP-1. *Genome Announc* **4**, e00814-16 (2016).

67. V. V. Koziaeva, S. A. Rusakova, N. V. Slobodova, M. Uzun, T. V. Kolganova, K. G. Skryabin, D. S. Grouzdev, Magnetospirillum kuznetsovii sp. nov., a novel magnetotactic bacterium isolated from a lake in the Moscow region. *International Journal of Systematic and Evolutionary Microbiology* **69**, 1953–1959 (2019).

68. M. L. Fdez-Gubieda, A. Muela, J. Alonso, A. García-Prieto, L. Olivi, R. Fernández-Pacheco, J. M. Barandiarán, Magnetite Biomineralization in Magnetospirillum gryphiswaldense: Time-Resolved Magnetic and Structural Studies. *ACS Nano* **7**, 3297–3305 (2013).

69. K. H. Schleifer, D. Schüler, S. Spring, M. Weizenegger, R. Amann, W. Ludwig, M. Köhler, The Genus *Magnetospirillum* gen. nov. Description of *Magnetospirillum gryphiswaldense* sp. nov. and Transfer of *Aquaspirillum magnetotacticum* to *Magnetospirillum magnetotacticum* comb. nov. *Systematic and Applied Microbiology* **14**, 379–385 (1991).

70. X. Wang, Q. Wang, W. Zhang, Y. Wang, L. Li, T. Wen, T. Zhang, Y. Zhang, J. Xu, J. Hu, S. Li, L. Liu, J. Liu, W. Jiang, J. Tian, Y. Li, D. Schüler, L. Wang, J. Li, Complete Genome

Sequence of Magnetospirillum gryphiswaldense MSR-1. *Genome Announc* **2**, e00171-14 (2014).

71. C. T. Lefèvre, M. L. Schmidt, N. Viloria, D. Trubitsyn, D. Schüler, D. A. Bazylinski, Insight into the Evolution of Magnetotaxis in Magnetospirillum spp., Based on *mam* Gene Phylogeny. *Appl Environ Microbiol* **78**, 7238–7248 (2012).

72. K. Zhu, H. Pan, J. Li, K. Yu-Zhang, S.-D. Zhang, W.-Y. Zhang, K. Zhou, H. Yue, Y. Pan, T. Xiao, L.-F. Wu, Isolation and characterization of a marine magnetotactic spirillum axenic culture QH-2 from an intertidal zone of the China Sea. *Research in Microbiology* **161**, 276–283 (2010).

73. B. Ji, S.-D. Zhang, P. Arnoux, Z. Rouy, F. Alberto, N. Philippe, D. Murat, W.-J. Zhang, J.-B. Rioux, N. Ginet, M. Sabaty, S. Mangenot, N. Pradel, J. Tian, J. Yang, L. Zhang, W. Zhang, H. Pan, B. Henrissat, P. M. Coutinho, Y. Li, T. Xiao, C. Médigue, V. Barbe, D. Pignol, E. Talla, L.-F. Wu, Comparative genomic analysis provides insights into the evolution and niche adaptation of marine Magnetospira sp. QH-2 strain. *Environmental Microbiology* **16**, 525–544 (2014).

74. C. L. Monteil, G. Perrière, N. Menguy, N. Ginet, B. Alonso, N. Waisbord, S. Cruveiller, D. Pignol, C. T. Lefèvre, Genomic study of a novel magnetotactic Alphaproteobacteria uncovers the multiple ancestry of magnetotaxis. *Environmental Microbiology* **20**, 4415–4430 (2018).

75. D. A. Bazylinski, T. J. Williams, C. T. Lefèvre, D. Trubitsyn, J. Fang, T. J. Beveridge, B. M. Moskowitz, B. Ward, S. Schübbe, B. L. Dubbels, B. Simpson, Magnetovibrio blakemorei gen. nov., sp. nov., a magnetotactic bacterium (Alphaproteobacteria: Rhodospirillaceae) isolated from a salt marsh. *International Journal of Systematic and Evolutionary Microbiology* **63**, 1824–1833 (2013).

76. D. Trubitsyn, F. Abreu, F. B. Ward, T. Taylor, M. Hattori, S. Kondo, U. Trivedi, S. Staniland, U. Lins, D. A. Bazylinski, Draft Genome Sequence of Magnetovibrio blakemorei Strain MV-1, a Marine Vibrioid Magnetotactic Bacterium. *Genome Announc* **4**, e01330-16 (2016).

77. C. T. Lefèvre, N. Viloria, M. L. Schmidt, M. Pósfai, R. B. Frankel, D. A. Bazylinski, Novel magnetite-producing magnetotactic bacteria belonging to the Gammaproteobacteria. *ISME J* **6**, 440–450 (2012).

78. C. Geurink, C. T. Lefevre, C. L. Monteil, V. Morillo-Lopez, F. Abreu, D. A. Bazylinski, D. Trubitsyn, Complete Genome Sequence of Strain BW-2, a Magnetotactic Gammaproteobacterium in the Family Ectothiorhodospiraceae, Isolated from a Brackish Spring in Death Valley, California. *Microbiol Resour Announc* **9**, e01144-19 (2020).

79. J. Li, H. Zhang, N. Menguy, K. Benzerara, F. Wang, X. Lin, Z. Chen, Y. Pan, Single-Cell Resolution of Uncultured Magnetotactic Bacteria via Fluorescence-Coupled Electron Microscopy. *Appl Environ Microbiol* **83**, e00409-17 (2017).

80. D. Trubitsyn, C. L. Monteil, C. Geurink, V. Morillo-Lopez, L. Gonzaga Paula de Almeida, A. T. Ribeiro de Vasconcelos, F. Abreu, D. A. Bazylinski, C. T. Lefevre, Complete Genome Sequence of Strain SS-5, a Magnetotactic Gammaproteobacterium Isolated from the Salton Sea, a Shallow, Saline, Endorheic Rift Lake Located on the San Andreas Fault in California. *Microbiol Resour Announc* **10**, e00928-20 (2021).

81. C. T. Lefèvre, A. Bernadac, K. Yu-Zhang, N. Pradel, L.-F. Wu, Isolation and characterization of a magnetotactic bacterial culture from the Mediterranean Sea. *Environmental Microbiology* **11**, 1646–1657 (2009).

82. B. Ji, S.-D. Zhang, W.-J. Zhang, Z. Rouy, F. Alberto, C.-L. Santini, S. Mangenot, S. Gagnot, N. Philippe, N. Pradel, L. Zhang, S. Tempel, Y. Li, C. Médigue, B. Henrissat, P. M. Coutinho, V. Barbe, E. Talla, L.-F. Wu, The chimeric nature of the genomes of marine magnetotactic coccoid-ovoid bacteria defines a novel group of Proteobacteria. *Environmental Microbiology* **19**, 1103–1119 (2017).

83. F. C. Meldrum, S. Mann, B. R. Heywood, R. B. Frankel, D. A. Bazylinski, Electron microscopy study of magnetosomes in a cultured coccoid magnetotactic bacterium. *Proceedings of the Royal Society of London. Series B: Biological Sciences* **251**, 231–236 (1993).

84. S. Schübbe, T. J. Williams, G. Xie, H. E. Kiss, T. S. Brettin, D. Martinez, C. A. Ross, D. Schüler, B. L. Cox, K. H. Nealson, D. A. Bazylinski, Complete Genome Sequence of the Chemolithoautotrophic Marine Magnetotactic Coccus Strain MC-1. *Appl Environ Microbiol* **75**, 4835–4852 (2009).

85. V. Morillo, F. Abreu, A. C. Araujo, L. G. Almeida, A. E. Prast, M. Farina, A. T. R. Vasconcelos, D. A. Bazylinski, U. Lins, Isolation, cultivation and genomic analysis of magnetosome biomineralization genes of a new genus of South-seeking magnetotactic cocci within the Alphaproteobacteria. *Frontiers in Microbiology* **5** (2014).

86. V. Koziaeva, M. Dziuba, P. Leão, M. Uzun, M. Krutkina, D. Grouzdev, Genome-Based Metabolic Reconstruction of a Novel Uncultivated Freshwater Magnetotactic coccus "Ca. Magnetaquicoccus inordinatus" UR-1, and Proposal of a Candidate Family "Ca. Magnetaquicoccaceae." *Frontiers in Microbiology* **10** (2019).

87. F. Abreu, K. T. Silva, P. Leão, I. A. Guedes, C. N. Keim, M. Farina, U. Lins, Cell Adhesion, Multicellular Morphology, and Magnetosome Distribution in the Multicellular Magnetotactic Prokaryote Candidatus Magnetoglobus multicellularis. *Microscopy and Microanalysis* **19**, 535–543 (2013).

88. F. Abreu, J. L. Martins, T. S. Silveira, C. N. Keim, H. G. P. L. de Barros, F. J. G. Filho, U. Lins, 'Candidatus Magnetoglobus multicellularis', a multicellular, magnetotactic prokaryote from a hypersaline environment. *International Journal of Systematic and Evolutionary Microbiology* **57**, 1318–1322 (2007).

89. F. Abreu, V. Morillo, F. F. Nascimento, C. Werneck, M. E. Cantão, L. P. Ciapina, L. G. P. de Almeida, C. T. Lefèvre, D. A. Bazylinski, A. T. R. de Vasconcelos, U. Lins,

Deciphering unusual uncultured magnetotactic multicellular prokaryotes through genomics. *The ISME Journal* **8**, 1055–1068 (2014).

90. P. Leão, Y.-R. Chen, F. Abreu, M. Wang, W.-J. Zhang, K. Zhou, T. Xiao, L.-F. Wu, U. Lins, Ultrastructure of ellipsoidal magnetotactic multicellular prokaryotes depicts their complex assemblage and cellular polarity in the context of magnetotaxis. *Environmental Microbiology* **19**, 2151–2163 (2017).

91. R. Zhang, Y.-R. Chen, H.-J. Du, W.-Y. Zhang, H.-M. Pan, T. Xiao, L.-F. Wu, Characterization and phylogenetic identification of a species of spherical multicellular magnetotactic prokaryotes that produces both magnetite and greigite crystals. *Research in Microbiology* **165**, 481–489 (2014).

92. S. Kolinko, M. Richter, F.-O. Glöckner, A. Brachmann, D. Schüler, Single-cell genomics reveals potential for magnetite and greigite biomineralization in an uncultivated multicellular magnetotactic prokaryote. *Environmental Microbiology Reports* **6**, 524–531 (2014).

93. H. Nakazawa, A. Arakaki, S. Narita-Yamada, I. Yashiro, K. Jinno, N. Aoki, A. Tsuruyama, Y. Okamura, S. Tanikawa, N. Fujita, H. Takeyama, T. Matsunaga, Whole genome sequence of *Desulfovibrio magneticus* strain RS-1 revealed common gene clusters in magnetotactic bacteria. *Genome Res.* **19**, 1801–1808 (2009).

94. C. T. Lefèvre, R. B. Frankel, M. Pósfai, T. Prozorov, D. A. Bazylinski, Isolation of obligately alkaliphilic magnetotactic bacteria from extremely alkaline environments. *Environmental Microbiology* **13**, 2342–2350 (2011).

95. J. Li, P. Liu, N. Menguy, X. Zhang, J. Wang, K. Benzerara, L. Feng, L. Sun, Y. Zheng, F. Meng, L. Gu, E. Leroy, J. Hao, X. Chu, Y. Pan, Intracellular silicification by early-branching magnetotactic bacteria. *Sci. Adv.* **8**, eabn6045 (2022).

96. W. Lin, A. Deng, Z. Wang, Y. Li, T. Wen, L.-F. Wu, M. Wu, Y. Pan, Genomic insights into the uncultured genus ‘Candidatus Magnetobacterium’ in the phylum Nitrospirae. *ISME J* **8**, 2463–2477 (2014).

97. S. Kolinko, M. Richter, F.-O. Glöckner, A. Brachmann, D. Schüler, Single-cell genomics of uncultivated deep-branching magnetotactic bacteria reveals a conserved set of magnetosome genes. *Environmental Microbiology* **18**, 21–37 (2016).

98. M. Uzun, V. Koziaeva, M. Dziuba, P. Leão, M. Krutkina, D. Grouzdev, Detection of interphylum transfers of the magnetosome gene cluster in magnetotactic bacteria. *Front. Microbiol.* **13**, 945734 (2022).

99. Y. Zhao, W. Zhang, H. Pan, J. Chen, K. Cui, L.-F. Wu, W. Lin, T. Xiao, W. Zhang, J. Liu, Insight into the metabolic potential and ecological function of a novel Magnetotactic Nitrospirota in coral reef habitat. *Front. Microbiol.* **14**, 1182330 (2023).

100. S. Kolinko, C. Jogler, E. Katzmann, G. Wanner, J. Peplies, D. Schüler, Single-cell analysis reveals a novel uncultivated magnetotactic bacterium within the candidate division OP3. *Environmental Microbiology* **14**, 1709–1721 (2012).

101. C. C. Bidaud, C. L. Monteil, N. Menguy, V. Busigny, D. Jézéquel, É. Viollier, C. Travert, F. Skouri-Panet, K. Benzerara, C. T. Lefevre, É. Duprat, Biogeochemical Niche of Magnetotactic Cocci Capable of Sequestering Large Polyphosphate Inclusions in the Anoxic Layer of the Lake Pavin Water Column. *Front. Microbiol.* **12**, 789134 (2022).

102. M. Bennet, A. McCarthy, D. Fix, M. R. Edwards, F. Repp, P. Vach, J. W. C. Dunlop, M. Sitti, G. S. Buller, S. Klumpp, D. Faivre, Influence of Magnetic Fields on Magneto-Aerotaxis. *PLoS ONE* **9**, e101150 (2014).

103. R. B. Frankel, D. A. Bazylinski, M. S. Johnson, B. L. Taylor, Magneto-aerotaxis in marine coccoid bacteria. *Biophys J* **73**, 994–1000 (1997).

104. C. T. Lefèvre, M. Bennet, L. Landau, P. Vach, D. Pignol, D. A. Bazylinski, R. B. Frankel, S. Klumpp, D. Faivre, Diversity of Magneto-Aerotactic Behaviors and Oxygen Sensing Mechanisms in Cultured Magnetotactic Bacteria. *Biophysical Journal* **107**, 527–538 (2014).

105. K. T. Elliott, I. B. Zhulin, J. A. Stuckey, V. J. DiRita, Conserved Residues in the HAMP Domain Define a New Family of Proposed Bipartite Energy Taxis Receptors. *J Bacteriol* **191**, 375–387 (2009).

106. D. E. Deatherage, J. E. Barrick, "Identification of Mutations in Laboratory-Evolved Microbes from Next-Generation Sequencing Data Using breseq" in *Engineering and Analyzing Multicellular Systems: Methods and Protocols*, L. Sun, W. Shou, Eds. (Springer, New York, NY, 2014; https://doi.org/10.1007/978-1-4939-0554-6_12), pp. 165–188.